ESD-TR-69-138

Technical Report

458

J. A. Ball

Observations
of OH Radio Emission Sources

23 May 1969

Lincoln Laboratory

MASSACHUSETTS INSTITUTE OF TECHNOLOGY

Lexington, Massachusetts

AD0704572

MASSACHUSETTS INSTITUTE OF TECHNOLOGY

LINCOLN LABORATORY

OBSERVATIONS OF OH RADIO EMISSION SOURCES

JOHN A. BALL

Group 31

LEXINGTON   MASSACHUSETTS

OBSERVATIONS OF OH RADIO EMISSION SOURCES[*]

ABSTRACT

The 18-cm OH radio emission sources were studied to determine their character and their relation to other objects in our galaxy. The Haystack and Millstone antennas were used with a 100-channel digital autocorrelator to obtain Stokes parameter spectra of many of the brighter sources. Time variations in the OH emission from some of these sources were detected and studied and maps of the regions around OH emission sources were obtained in the continuum near 2 and 4 cm. The Haystack-Millstone spectral-line interferometer was used to check the positions of a pair of OH emission sources and to search for angular variation in the OH absorption across Cas A. Evidence for phenomenological associations between OH emission and H II regions, supernovae remnants, and infrared objects is discussed in the report and a kinematic model of the OH emission sources presented.

CONTENTS

OBSERVATIONS OF OH RADIO EMISSION SOURCES

I. INTRODUCTION

A. OH Molecule

The OH molecule is an electrically neutral combination of an oxygen and a hydrogen atom. The internal energy of such a molecule may be divided into three types: rotational (i.e., energy of rotation of the constituent atoms about their barycenter), vibrational (i.e., energy of periodic variation of the distance between the two atoms), and electronic (i.e., energy of the electrons bound to the molecule). In molecules such as OH, transitions between rotational states give rise to microwave and far infrared lines, transitions between vibrational states give rise to near infrared and visible lines, and transitions between electronic states give rise to visible and ultraviolet lines.

The ground state of OH is $^2\Pi_{3/2}$, $J = 3/2$ (the $^2\Pi_{1/2}$ level is higher in energy). In this notation, the superscript is $2S + 1$ where S is the unpaired electron spin (there are nine electrons, one unpaired, giving $S = 1/2$), and the Π indicates that Λ, the projection of the electronic orbital angular momentum onto the internuclear axis, is one. The subscript following the Π is the vector sum of S and Λ, i.e., the total electronic angular momentum component on the internuclear axis, and J is the total angular momentum (except for nuclear spin), i.e., the sum of the electronic and rotational angular momenta.

The transition from the ground state to the first rotationally excited state ($^2\Pi_{3/2}$, $J = 5/2$) and the "fine structure" transitions between $^2\Pi_{3/2}$ states and $^2\Pi_{1/2}$ states are in the infrared. However, the ground state of OH is Λ doubled with a separation of about 1666 MHz in the radio microwave region. This Λ doubling occurs because of an interaction between the electronic orbital angular momentum and the molecular rotation, and may be thought of as a partial uncoupling of the electronic angular momentum from the internuclear axis with a tendency to couple it instead to the rotation axis. The ground state of OH is intermediate between Hund's coupling case (a) for which the spin and orbital electronic angular momenta are coupled to the internuclear axis, and Hund's case (b) for which the orbital electronic angular momentum is still coupled to the internuclear axis, but the spin is coupled instead to the resultant of the orbital electronic and rotational angular momenta. Λ doubling represents a tendency toward Hund's case (d) for which the orbital angular momentum is coupled to the rotation axis. The Λ doublet states may properly be labeled with their parity (+ or −) but not by Λ, because each state is a combination of $\Lambda = +1$ and −1.

These Λ doublet states are further split with a separation of about 53 MHz by an interaction with the magnetic moment of the nuclear spin. These substates may be labeled F, the total

angular momentum including nuclear spin. The resulting energy level diagram for the ground state of OH is shown schematically in Fig. 1. The four transitions of interest are at 1612231, 1665401, 1667358, and 1720527 kHz. The relative line strengths (1:5:9:1) are also indicated in Fig. 1. The transitions in the figure are electric dipole and the transition probability (the Einstein A) is 7.7×10^{-11}/sec for the 1667 transition.
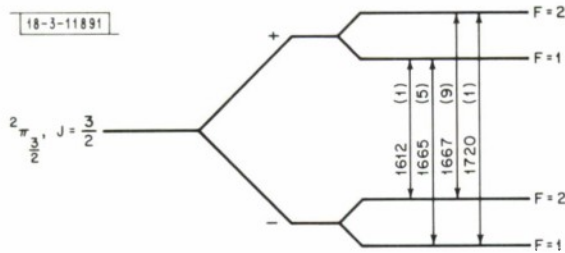

Fig. 1. Energy level diagram of OH.

Further details about the OH molecule may be found in Townes and Schawlow (1955) and Herzberg (1950).

B. History of OH Radio Astronomy

The original proposal that the radio frequency transitions of OH should be looked for from extraterrestrial sources is apparently due to Shklovsky (1953). Townes (1957) also made such a suggestion and in 1956 Barrett and Lilley (1957) tried and failed to detect OH. At that time, the frequencies of the lines were known only with low accuracy. But as increasingly accurate laboratory measurements became available [Dousmanis, et al. (1955), Ehrenstein, et al. (1959), Radford (1961) and (1964)], two attempts were made in 1963 [Penzias (1964), Weinreb, et al. (1963)] Weinreb, Barrett, Meeks and Henry, using Lincoln Laboratory's 84-foot Millstone antenna, detected the 1665- and 1667-MHz absorption against Cas A late in 1963 [Weinreb, et al. (1963)] This was confirmed by Dieter and Ewen (1964) and Bolton, et al. (1964), and Weaver and Williams (1964) found OH absorption against Sag A. Barrett, et al. (1964) studied Cas A further and found that the OH absorption near zero velocity is a double feature without a counterpart in H I absorption. Robinson, et al. (1964) studied the Sag A OH absorption in more detail and found additional strong OH absorption with almost no corresponding feature in the H I absorption. They gave evidence for believing that some of the OH is not distributed uniformly over the source. Gardner, et al. (1964) detected OH absorption at 1612- and 1720-MHz against Sag A. Goldstein, et al. (1964) discovered additional OH absorption against Sag A, again without any strong counterpart in the H I absorption.

At this point the observations seemed to fit fairly well into the pattern of accepted ideas about the galaxy. The ratios of the absorptions in the various OH lines agreed fairly well with the values predicted by the transition probabilities with the possibility of a high optical depth and a mottled distribution of OH [Gunderman (1965)]. The width of the absorption lines ranges from ten to several hundred kHz.

In 1965 Gunderman (1965) and Weaver, Williams, Dieter and Lum [(1965) and (1966)] discovered remarkably narrow and intense emission features while looking for absorption against certain Galactic H II regions. These results were confirmed [Zuckerman, et al. (1965), McGee, et al. (1965)] and it was found that some of the features are strongly linearly [Weinreb, et al.

(1965)] and circularly [Davies, et al. (1966), Barrett and Rogers (1966)] polarized. The polarization properties of some of the stronger emission sources were measured in detail [Palmer and Zuckerman (1967), Williams, et al. (1966), Meeks, et al. (1966)] and it was found that strong circular polarization is very common, linear polarization is less common, and completely unpolarized features are rare. Very little correlation of features between 1665 and 1667 MHz was found and there is perhaps evidence of anti-correlation. No simple pattern of Zeeman split features will fit the data. Although the kinetic temperatures implied by the widths of the emission features are typically 10° to 100°K, the brightness temperatures were already known to be over 1000°K and this was only a lower limit because the angular sizes of the sources were unresolved.

To add to the list of anomalies, Dieter, Weaver, and Williams (1966) reported large time variations within a span of weeks in some of the OH emission features coming from NGC 6334 and Orion, and these results have been at least partially confirmed [Palmer and Zuckerman (1967), Ball and Meeks (1968)], although this is clearly an area which needs much more observational work.

Because the angular sizes and hence the brightness temperatures could not be found from single antenna measurements, a series of interferometer measurements were undertaken [Cudaback, et al. (1966), Rogers, et al. (1966), Rogers, et al. (1967), Davies, et al. (1967), Radhakrishnan and Whiteoak (1967), Moran, et al. (1967 a and b)]. Most of the OH emission sources do not exactly coincide with strong continuum sources. These interferometer measurements have succeeded in separating some of the sources into spatial components, but some of the individual features have not yet been resolved in angle.

The latest results [Moran, et al. (1968)], show that the W3 OH emission is coming from a region a few thousand au's in diameter. Since this size is characteristic of solar-system dimensions rather than interstellar distances, we are led to think that we are observing OH emission from a circumstellar envelope around a single star, or perhaps a protostar. Furthermore, within this region the individual OH emission features originate in much smaller spots typically only a few au in size. The apparent brightness temperature of one of the features in W3 is now known to be at least 10^{12}°K [Moran, et al. (1968)].

Meanwhile other OH lines were sought. $O^{18}H$ was seen in absorption [Barrett and Rogers (1964), Robinson (1967)] but not in emission [Wilson and Barrett (1968)]. The $^2\Pi_{1/2}$, J = 1/2 transition [Zuckerman, et al. (1968)], the $^2\Pi_{3/2}$, J = 5/2 transition [Yen, et al. (1969)], and the $^2\Pi_{1/2}$, J = 5/2 transition (Schwarz, P., private communication) were found in OH emission. The recent discovery of water vapor in emission from some of the same sources seen in OH emission [Cheung, et al. (1969), Knowles, et al. (1969)] promises to help us understand the nature of these sources. The $^2\Pi - {}^2\Sigma$ bands of OH occur around 3000 Å and although this wavelength is rather strongly absorbed by the earth's atmosphere, these bands have been looked for in stellar spectra [Goss and Spinrad (1966)], but without success.

From the myriad of problems concerning the OH emission sources, the following questions were selected for this study, primarily because the technology for making significant measurements was available or in prospect. (1) What additional observational constraints can be placed on the models of the OH emission sources and the kinematic and spatial relationships within and among the sources? To approach this question, the details of the Stokes parameters of the OH emission features from some of these sources were studied and time variations in these parameters were monitored. (2) What associations and interactions exist between the OH emission

TABLE I

ANTENNA AND FEED PROPERTIES

Antenna	Frequency (GHz)	Feed	Polarization	Antenna Temperature (°K) and Source		Aperture Efficiency η_A (percent)	ξ * (fu/°K)	Beamwidth (mdeg)	Beam † Efficiency η_B (percent)	(Mapping ‡ Efficiency)$^{-1}$ (fu/°K/deg²)	Remarks
1. Haystack	15.5	Rotatable horn	Linear	1.7 ± 0.3	W75-DR21	22 ± 4	5.9 ± 1.2	36 ± 3	33 ± 5	6850 ± 700	Pre-rerigging [see also Allen (1966)]
2. Haystack	15.5	Rotatable horn	Linear	2.1 ± 0.3	W75-DR21	27 ± 4	4.8 ± 0.7	36 ± 3	36 ± 3	6150 ± 700	Post-rerigging [see also Allen (1966)]
3. Haystack	8	Rotatable Clavin	Linear	1.9 ± 0.2	W75-DR21	25 ± 4	5.25 ± 0.7	72 ± 5	28 ± 3	2120 ± 300	
4. Haystack	7.795	Radar horn	Left circular	2.9 ± 0.4	W75-DR21	38 ± 5	3.45 ± 0.5	72 ± 4	46 ± 5	1230 ± 150	The error bars include both the pre- and post-rerigging values
5. Haystack	1.66	Rotatable Clavin	Linear	210 ± 15	Cas A	27 ± 3	4.9 ± 0.4	381 ± 10			
6. Haystack	1.66	Andrew	Right circular	165 ± 10	Cas A	21 ± 3	6.2 ± 0.4	376 ± 10			
7. Haystack	1.66	Andrew	Left circular	164 ± 10	Cas A	21 ± 2	6.3 ± 0.4	374 ± 10			
8. Haystack	1.66	Andrew	Linear horizontal	175 ± 15	Cas A	22 ± 2	5.9 ± 0.5	370 ± 10			
9. Haystack	1.66	Andrew	Linear vertical	152 ± 15	Cas A	19 ± 2	5.8 ± 0.6	374 ± 10			
10. Haystack	1.72	Andrew	Right circular	130 ± 10	Cas A	17 ± 2	7.7 ± 0.6	373 ± 15			
11. Haystack	1.72	Andrew	Left circular	122 ± 10	Cas A	16 ± 2	8.2 ± 0.7	372 ± 20			Asymmetrical beam
12. Millstone	1.66	Horn	Right circular	145 ± 10	Cas A	38 ± 3	7.1 ± 0.5	491 ± 10			
13. Millstone	1.66	Horn	Left circular	146 ± 10	Cas A	38 ± 3	7.0 ± 0.5	494 ± 10			
14. Millstone	1.66	Horn	Linear horizontal	157 ± 10	Cas A	41 ± 3	6.5 ± 0.5	495 ± 10			
15. Millstone	1.66	Horn	Linear vertical	155 ± 10	Cas A	41 ± 3	6.6 ± 0.5	494 ± 10			
16. Millstone	1.72	Horn	Right circular	129 ± 10	Cas A	34 ± 3	7.8 ± 0.6	485 ± 15			
17. Millstone	1.72	Horn	Left circular	131 ± 10	Cas A	35 ± 3	7.6 ± 0.6	473 ± 15			
18. Millstone	1.72	Horn	Linear horizontal	146 ± 10	Cas A	39 ± 3	6.9 ± 0.5	480 ± 15			
19. Millstone	1.72	Horn	Linear vertical	135 ± 10	Cas A	36 ± 3	7.4 ± 0.6	480 ± 15			
20. Millstone	1.61	Horn	Right circular	157 ± 15	Cas A	40 ± 3	6.7 ± 0.7	505 ± 15			
21. Millstone	1.61	Horn	Left circular	142 ± 15	Cas A	36 ± 3	7.4 ± 0.9	505 ± 15			

* ξ is equal to k/A_e (not $2k/A_e$).

† Beam efficiency was calculated both from the sum of the temperature numbers in the map and from a Gaussian model with the beamwidth given (see Sec. IV-A-2). The two methods give the same values to within the stated error limits.

‡ The (mapping efficiency)$^{-1}$ is equal to $2k/(\lambda^2 \eta_B)$ and was calculated from the sum of the temperature numbers in the map of the source (see Sec. IV-A-2).

4

sources and nearby objects (H II regions, SNR's, etc.)? To approach this problem, the regions around some of the OH emission sources were mapped in the radio continuum near 2 and 4 cm.

The material presented here can only be considered a progress report; some progress has been made on these problems, but some new problems have been uncovered. Sections II through IV present the data acquisition and data reduction techniques used in this study. Some of these techniques are new and not previously discussed in print; however, the reader who is primarily interested in the astronomical results may wish to skip to Sec. V.

II. EQUIPMENT – INSTRUMENTAL EVALUATION AND MEASUREMENTS

A. Haystack Antenna

All of the continuum measurements and many of the spectral line measurements described in this report were made with the 120-foot-diameter antenna of the Haystack Research Facility of Lincoln Laboratory. This is a paraboloidal antenna enclosed in a radome and located in Tyngsboro, Massachusetts. It is azimuth-elevation mounted and both the surface accuracy and the pointing accuracy permit operation down to about 8-millimeter wavelengths. This antenna has been described in some detail by Weiss (1965) and additional information can be found in Lincoln Laboratory Report "Radio Physics and Astronomy" 1965:1, Allen (1967), and Stuart (1968). The antenna is pointed in real time by computer programs written for the Univac 490 (U490). These programs are described in a series of Lincoln Laboratory Technical Notes [see Heart, et al. (1965) and other references therein].

Allen (1967) measured the gain and beamwidth of the Haystack antenna as a function of elevation at 8 and 15 GHz and analyzed the behavior of these parameters as a function of the temperature of the antenna structure. These measurements, however, were made before the recent rerigging [Stuart (1968)]. In the present study a number of Discrete Source Scan (DSS) runs (see Sec. III-A) were made to determine the gain, beamwidth and pointing accuracy of this antenna at various observing frequencies and with different feeds. The results of this antenna calibration are summarized in Table I.

The aperture efficiency at 1.6 and 1.7 GHz is based on continuum measurements of Cas A. The Cas A flux was calculated from a formula suggested by Allen (1967), namely

$$S = 6500(\nu/0.4)^{-0.785} \text{ fu}$$

for ν in GHz for the epoch 1964.4, and a secular decrease of 1.1 percent per year. This gives, for example, 2055 fu for 1.66 GHz for 1967.4. One fu is 10^{-26} watts/M^2/Hz. The aperture efficiency at 8 and 15 GHz is based on continuum measurements of W75-DR21, which was taken to be a point source and for which a flux of 20 fu at both these frequencies was assumed [see Ryle and Downs (1967) and Mezger, et al. (1967)].

ξ is the ratio of the source flux in a given sense of polarization to the observed antenna temperature, and is equal to k/A_e where k is Boltzmann's constant and A_e is the collecting area of the antenna. However, since the flux published for a continuum source is usually the total flux (S_o), i.e., the sum of the fluxes in two orthogonal polarizations, a value for the conversion factor from antenna temperature to flux equal to 2ξ is often used [e.g., by Allen (1966)] to convert a measured antenna temperature in one sense of polarization into a total flux for a source presumed to be unpolarized.

Allen (1967) found some dependence of the Haystack antenna gain on elevation angle and on differential temperature across the antenna structure. The gain variation with elevation was relatively small (perhaps 10 percent in going from the zenith to an elevation angle of 20°) and also the antenna system has been changed considerably since Allen's measurements were made. The temperature differential across the antenna surface has been substantially reduced [Stuart (1968)]. For these reasons, these effects have been neglected.

The pointing of the Haystack antenna was calibrated in November 1965 and again in November 1967 (after rerigging) by doing a large number of DSS runs (see Sec. III-A) on a number of small-diameter continuum radio sources whose positions are accurately known. Each DSS produces an azimuth and an elevation offset which equal the differences between the command positions and the position at which the program actually finds the source.

In order to understand these errors and predict them for subsequent observations, they were fit in a least-square sense with equations that take into account azimuth and elevation axis tilts and skews as well as the dominant sag or flexure term in elevation. These equations are

$$\Delta A = [\phi \cos(A - K_A) + \epsilon] \tan E + D \sin E + C_A$$

and

$$\Delta E = -\phi \sin(A - K_A) + \beta \cos E + C_A$$

where

A = azimuth

E = elevation

ϕ = tilt of the antenna-azimuth axis with respect to the zenith

$90° - K_A$ = azimuth of the antenna-azimuth axis (on the celestial sphere)

ϵ = offset of the antenna elevation axis from the plane perpendicular to the antenna azimuth axis

D = offset of the electrical boresight axis from the plane perpendicular to the antenna elevation axis

$D + C_A$ = offset of the zero position of the azimuth encoders from true North

β = sag or flexure coefficient

$\beta + C_E$ = offset of the zero position of the elevation encoders from true horizontal (at $A = K_A$).

These equations are derived and the program discussed in Meeks, et al. (1968). The results of the two pointing correction measurements are shown in Table II. The 1967 program was performed at 15 GHz while the 1965 program was carried out at 8 GHz and so had a larger beamwidth and used some radio sources whose angular structure is not negligible compared with the beamwidth. For these reasons the 1967 program should be more accurate in addition to showing changes in the antenna system since 1965. The parameters determined by this process were used to prepare a table which was incorporated into the computer pointing program for subsequent observations.

B. Millstone Antenna

Some of the spectral line measurements described in this report were made with the 84-foot-diameter antenna of the Lincoln Laboratory's Millstone Facility in Westford, Massachusetts, a

TABLE II			
HAYSTACK POINTING CALIBRATION			
Parameter	Nov. 1965 Value	Nov. 1967 Value	Units
ϕ } from azimuth errors	4.51	5.30	mdeg
K_A	25	41	deg
ϵ	−4.77	−3.98	mdeg
D	9.02	8.55	mdeg
C_A	−11.13	−25.58	mdeg
ϕ } from elevation errors	3.01	4.50	mdeg
K_A	27	27	deg
β	−51.70	−53.38	mdeg
C_E	61.62	57.08	mdeg
$\langle (\delta A \cos E)^2 \rangle^{1/2}$	3.1	2.9	mdeg
$\langle (\delta E)^2 \rangle^{1/2}$	3.6	3.6	mdeg

half mile from Haystack. The Millstone antenna is also azimuth-elevation mounted and is usable down to about 6-centimeter wavelengths. The results of the gain and beamwidth calibration of this antenna, using the horn feed at the prime focus, are listed in Table I.

A pointing calibration program similar to that done on Haystack was carried out on the Millstone antenna in November 1967. The digital encoders which monitor the pointing position of the Millstone antenna are quantized in 40 arcsecond (11 millidegree) steps. Therefore, as a rule of thumb, we cannot expect the pointing errors to be reduced much below this level. From 19 DSS runs the elevation errors were found to have an average value of 41 millidegrees with a scatter around this value from +17 to −15 millidegrees. There is no obvious pattern to these errors when plotted against either azimuth or elevation, so a 40 millidegree constant elevation bias was used in the pointing program for subsequent observations. The azimuth errors scaled by cosine of elevation showed an average value of 7 millidegrees and a scatter similar to the elevation errors. These azimuth errors were neglected in subsequent observations.

C.   Front Ends

This report contains measurements made at three frequencies — 8 and 15 GHz continuum and 1.6 GHz spectral line — using at least two different front ends at each frequency. Measurements were made both before and after rerigging [Stuart (1968)]. Table III contains a list of the front ends used and some of their important characteristics.

The figure of merit is the calculated rms noise for 1-second integration. In calculating the figure of merit, the bandwidth for the front ends used for continuum measurements was taken from the table; however, for the front ends used for spectral line work (1.6 GHz), the bandwidth was taken to be 1 kHz to correspond to the usual resolution used. To convert each figure of

TABLE III

FRONT ENDS

Name or Type	Antenna and Box	Center Frequency (GHz)	Nominal Bandwidth (MHz)	System Temperature (°K)	Figure of Merit*		Remarks
					Antenna Temperature (°K)	Flux Units	
"Old" TDA	Haystack receiver box	15.5	1000	2200	0.14	0.7	
"New" TDA	Haystack receiver box	15.5	1000	800	0.05	0.25	
TDA	Haystack receiver box	8	1000	1300	0.08	0.46	
Moser	Haystack radar box	7.795	10	60	0.038	0.13	
"Old" paramp	Haystack receiver box	1.6	10	370	23	160	Based on the Andrew feed
A.I.L. paramp	Haystack receiver box	1.6	10	230	15	100	Based on the Andrew feed
A.I.L. paramp	Millstone	1.6	10	202	13	91	

* The figure of merit is $2T_s/\sqrt{\beta}$, i.e., the theoretical rms noise for 1 second of integration.

merit to brightness temperatures and flux units, the numbers from Table 1 for the corresponding feed and antenna were used. For those front ends used with more than one feed, the numbers from Table 1 were averaged.

The numbers in Table III are only estimates; in particular the bandwidth and system temperature of the maser and the paramps depend on the tuning, and the system temperature rises at low elevations.

D. The Spectral Line Receiver

Figure 2 is a simplified block diagram of the spectral line receiver in a typical configuration. The dashed lines enclose optional items which were used for some, but not all, of the observations described herein.

The coaxial switch following the antenna selects right or left circular polarization, or, with the system reconfigured, horizontal or vertical linear polarization, when used with the Andrew feed on Haystack or the horn feed on Millstone. With the Clavin feed on Haystack, this coaxial switch is not used and the feed can be rotated by hand to any linear polarization position angle.

The calibration noise tube inserts 45°K additional noise into the antenna side of the ferrite switch. This 45°K was measured (by J. C. Carter) using a room temperature and a liquid-nitrogen-cooled load substituted for the antenna. The parametric amplifier itself provides image rejection; however, a preceding bandpass filter was sometimes used to prevent the Millstone radar transmitter (at about 1295 MHz) from interfering.

The local oscillator was phase locked to a signal derived from the station frequency standard using a general purpose frequency synthesizer. Frequency switching is possible with the Haystack system, but was not used for any of the observations reported here. Frequency errors from this source are less than 1 Hz. Sometimes a 28-MHz crystal oscillator was used as well, but its frequency was known to about 50 Hz. The 30-MHz to video frequency converter contains additional crystal oscillators whose frequencies could be monitored. After some initial difficulties with this unit, we now believe that the total frequency error from hardware causes is less than about 20 Hz. Some of the early measurements were made before this was achieved, and so may be somewhat worse. Section IV-B contains a discussion of frequency errors that may arise in the program that calculates the observer's velocity.

The video frequency converter selects a frequency window (typically 40 kHz) centered at 30 MHz and converts it to video, e.g., to 0 to 40 kHz. This signal is clipped, sampled, and fed to the autocorrelator at a clock rate two and a half times the window width, e.g., 100 kHz for a 40-kHz window. The correlator accumulates the autocorrelation functions for 100 ms and then dumps them into the U490 computer. Additional details about this system can be found in Weinreb (1963), and Rogers (1967a).

When the receiver is Dicke switching, the synchronous and gated detectors provide information to the U490 computer to calculate and monitor the effective system temperature which is needed to scale the final spectra. When the receiver is not Dicke switching a total power detector provides this information.

III. DATA ACQUISITION – TECHNIQUES AND PROCEDURES

A. Continuum

The Discrete Source Scan (DSS) program was written for the U490 computer by Mrs. P. P. Crowther to specifications by Dr. M. L. Meeks. It has been described elsewhere [Allen and
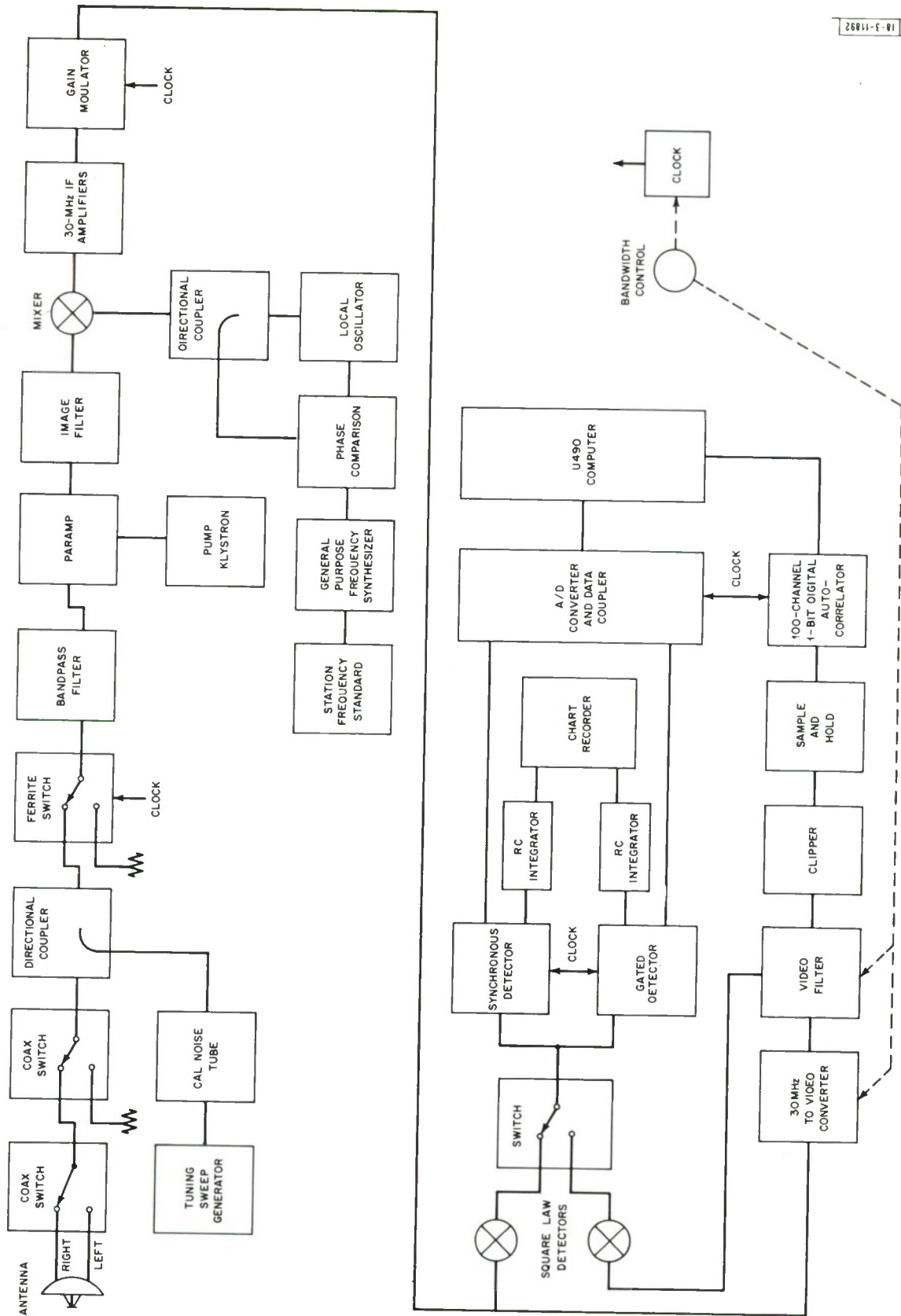
Fig. 2. Simplified block diagram of spectral line receiver in a typical configuration.

Barrett (1967) and Meeks, et al. (1968)] so will only be outlined here. The DSS program involves an interaction between real-time pointing of the antenna and real-time continuum data reduction which take place in the same computer. The DSS program first commands the antenna to make a declination scan through the pointing position of the source. The declination position of the peak temperature and the half-power width in declination are determined by fitting a pair of straight lines to the sides of the response curve. The program then commands the antenna to make a right ascension scan through this peak declination. The right ascension scan is processed in the same way as the declination scan. Then, using the peak position just found, the program commands an "on-off" in right ascension such that the same track in azimuth-elevation coordinates is followed for the "off" as for the "on." The results of the DSS, which are typed out immediately after the scan is finished, consist of the offsets from the command position to the position where the program actually found the peak temperature, and the value of this peak temperature from the "on-off." These offsets are given in both the azimuth-elevation and right ascension-declination coordinate systems. The program also types the response widths in right ascension and declination.

All the continuum maps in this report were made using the drift-curve technique with the Haystack antenna. The antenna remains stationary while the earth's rotation carries the source through the antenna beam. This technique has several outstanding advantages and perhaps only one minor disadvantage which are summarized below.

(1) The pointing errors are minimized. It is easier to make the antenna remain stationary at a specified position than to track at a specified speed.

(2) The contribution to the antenna temperature due to side lobes and back lobes of the antenna pattern striking the ground, and also the contribution due to the earth's atmosphere, are almost exactly constant during a drift curve and so they can be subtracted out. Allen (1967) reported that a component of the background temperature contribution varied rapidly with azimuth or elevation and he attributed this effect to the radome. Such a contribution has no effect on a drift curve.

(3) The baseline temperature, which corresponds to the "off" temperature in an "on-off" technique, is determined from the average of many data points. Therefore, it has a lower noise component than the "off" of an "on-off" that contains the same integration time as the "on." In Sec. III-B, an almost exactly analogous technique for spectral line observing is analyzed and shown to be superior.

The only real disadvantage of the drift curve technique has to do with the effective integration time which is equal to the time required for the earth's rotation to carry a point through half of the antenna's half-power beamwidth. The observer may get any effective integration time for a map which is an integral multiple of this time for a single drift curve, but he cannot spend less time in making a map. This restriction was no disadvantage for the maps in this report.

One other point deserves mention. In making a drift curve map one tacitly assumes that the baseline region of the sky outside the region to be mapped has negligible emission. With possibly one exception mentioned in Sec. V-H, this condition was made to hold for the maps in this report by taking sufficiently long drift curves. However, this point may be a serious problem with drift curve maps made at lower frequencies or with more sensitive systems.

B. Spectral Line

The spectral line data for this report were taken with the 100-channel one-bit digital autocorrelator described in Sec. II-D. Several modes of operation were possible including Dicke

switching and frequency switching (with Haystack). During the course of the observations, the nonswitched mode of operation also became possible. The autocorrelator accumulates autocorrelation functions for only 100 ms before dumping them into the computer. Originally, this interval corresponded to half a cycle of Dicke or frequency switching. However, it was found that the system noise temperature as a function of frequency across the window width and referred to the antenna (which is the relevant parameter with a clipped system), did not change appreciably over a period of many minutes or hours. It is therefore possible to accumulate "off" data for many minutes with the antenna pointing off but near the source, and then move the antenna onto the source for "on" data. This procedure, referred to as the nonswitched mode of operation, should probably be called "antenna switching." It has the following advantages:

(1) The frequency dependent VSWR of the antenna as compared with the VSWR of the dummy load, which may produce a sloping or curved baseline with Dicke or frequency switching, has almost no effect on the data taken in the nonswitched mode. It has no effect at all if the continuum temperature seen by the antenna during the "off" is the same as during the "on."

(2) The ferrite (Dicke) switch may be completely removed from the circuit to reduce the system temperature. (This, of course, is also true of frequency switching.)

(3) The "offs" and "ons" need not contain the same integration time and one "off" may be used with several "ons" under certain circumstances. The rule for using a single "off" with several "ons" is that the resulting spectra should not be averaged or added unless first shifted by one or more equivalent filter widths. Between two spectra using the same "off," the receiver noise is partly correlated in the same equivalent filters, but uncorrelated in adjacent filters. Since more than one frequency window was wanted in almost all the spectra taken for this report, this technique was quite valuable in reducing the integration time necessary for a given signal-to-noise ratio.

Given that one "off" will be used with several "ons," the question arises as to how one should divide up a given block of observing time among the "ons" and the "off" to produce minimum noise on the resulting spectra. This problem is analyzed below.

Let N be the number of "ons" wanted (to be used with a single "off"), t be the time for each "on," α be the ratio of "off" time to t, and T be the total observing time which is $(\alpha + n) t$. Then the noise for each "on" is $\propto t^{-1/2}$ and for the "off" is $\propto (\alpha t)^{-1/2}$. The total noise for the "on-off" is $\propto [(\alpha + 1)/\alpha t]^{1/2}$ which is $\propto (\alpha + N + 1 + N/\alpha)^{1/2}$. We differentiate this with respect to α, set the result to zero, and get $\alpha = N^{1/2}$. This means that we minimize the noise on each of the resulting spectra by spending $N^{1/2}$ times as much time on the "off" as on each "on." For example, we may divide a 5-hour observing session into a one-hour "off" and sixteen 15-minute "ons." For this example, the noise on the resulting spectra will be reduced by a factor of 0.584 compared with Dicke or frequency switching for the same total observing session.

A similar analysis may be applied to the drift curve technique in continuum observations. The baseline interval corresponds to the "off" and each $\lambda/(2D)$ section of the record corresponds to an "on."

C. Interferometer

The Haystack-Millstone interferometer has been described in some detail by Rogers (1967) and Rogers (1968) and so will only be outlined here. The antennas and front ends for this interferometer are described in Sec. 11. A reference frequency, from which the local oscillator frequency was synthesized, was sent on a coaxial cable from Haystack to Millstone and the Millstone

IF signals were sent back to Haystack on the same cable. The electrical length of this cable was held constant by a motor-driven mechanical line stretcher (trombone section). This technique virtually eliminates instrumental phase drift.

The most desirable way of obtaining the fringe amplitude and phase for a spectral line interferometer involves cross-correlating the received signals. No cross-correlator was available, so Rogers developed an add-subtract-autocorrelation technique which yields the same information with a slightly poorer signal-to-noise ratio. The Haystack and Millstone IF signals are first added for 100 ms and the autocorrelator processes the resulting bit string and dumps the results into the U490 computer. The IF signals are then subtracted for 100 ms, etc. A program in the U490 computer (a modification by Mrs. P. P. Crowther of AUTOCOR) writes these autocorrelation numbers onto magnetic tape, along with timing and other information, for subsequent processing by a post-real-time program in the CDC 3300 computer. This post-real-time program (MILSTAK or MILSTAKS, written by J. M. Moran, Jr. and A. E. E. Rogers) produces the fringe amplitude and phase as a function of frequency across the spectral window for each integration period which was typically 10 to 30 minutes.

The original observations with this interferometer by Rogers, et al. (1966) were of unresolved OH emission sources. Positions and upper limits for the angular sizes of such sources were obtained. Observations of continuum sources (as calibrators) were also made. Rogers shows that for observations of continuum sources for which the total delay is sufficient to produce many interferometer fringes across the spectral window, the correct continuum fringe amplitude and phase may be obtained from a weighted vector average over the spectral window. If, however, there is insufficient total delay relative to the spectral window, then a clipped interferometer cannot give the correct answer. This is easy to see when there is no delay. For this case, only the power level input to the clipper changes with phase switching and with time. Since the clipper is insensitive to the power level at its input, no information about this power level is available to the computer unless it is recorded separately.

This problem can be looked at as one of recovering the true autocorrelation numbers from the clipped ones. There are two parts to this clipping correction: (1) taking the trigonometric sine of the clipped autocorrelation functions and (2) "unnormalizing" by multiplying by the equivalent interferometer system temperature. When there are not many interferometer fringes across the frequency window, this normalization factor varies on a second-by-second basis (i.e., it has time fringes), rather than remaining nearly constant through a run.

These variations of the equivalent system temperature will be referred to as continuum fringes, and the process of recording the continuum fringes and using the correct variable normalization factor as continuum fringe compensation. It is necessary to do this in order to observe a continuum source with a narrow spectral window, even if the continuum information itself is not wanted. The only other alternative would be to introduce additional delay into the long leg of the interferometer, to produce many fringes across the spectral window.

To implement the continuum fringe compensation scheme on the Haystack-Millstone interferometer, two gated detectors were used to record the quantities:

$$D_1 = \overline{(e_H + e_M)^2} \tag{1}$$

and

$$D_2 = \overline{(e_H - e_M)^2} \tag{2}$$

where e_H and e_M are the IF voltages from the Haystack and Millstone receivers, respectively. The bar indicates a time average long compared with a cycle of the IF but short compared with a cycle of the interferometer fringes; three seconds were used in practice. The quantities D_1 and D_2 are proportional to the factor which should be used to scale those clipped autocorrelation functions that are taken during the "add" and the "subtract" portions of the switch cycle, respectively. The quantity $D_1 + D_2$ is proportional to the constant component and $D_1 - D_2$ is proportional to the variable component of the equivalent system temperature. In practice the variable component was fit with a sinusoid in order to extrapolate ahead in time, since the continuum data were delayed on the tape. This process also reduces the noise contribution.

The "sine" portion of the clipping correction is somewhat more of a problem, because to actually calculate the trigonometric sine in the computer for each of the autocorrelation numbers would require an excessive amount of computer time (one thousand sines would be needed for each second of data). However, the normalized autocorrelation numbers are always small and it is a good approximation to take the argument for the sine (i.e., just multiply by $\pi/2$). In the absence of continuum fringes, only the difference between the two autocorrelation numbers is needed [see Rogers (1967b), p. 14]; in the presence of continuum fringes both the sum and difference are needed.

It was found in obtaining the data in this way that a residual slope (i.e., a variation of fringe phase with frequency across the spectral window) was sometimes seen (see Sec. V-J) and this instrumental effect may possibly be due to the omission of the sine clipping correction.

IV. DATA REDUCTION – TECHNIQUES AND PROCEDURES

A. Continuum

1. Continuum Maps

The real-time program [Stylos (1965)] in the U490 provides a preliminary reduction of the incoming raw data by converting the voltages to temperatures which are printed and recorded on magnetic tape. A map reduction program written for the CDC 3300 computer by N. M. Brenner to specifications by Dr. M. L. Meeks reads these tape records and processes the data to eventually obtain a map. The details of this program are given by Brenner [N. M. Brenner (1969), in preparation] and are outlined here.

The program is divided into three parts, lettered A, B, and C. Program part A reads the data tapes made by the U490 and locates the drift curves on them. The tape record contains the time, right ascension, declination, azimuth, and elevation as well as the temperatures, so the program checks that the azimuth, elevation and declination are constant, and the right ascension is drifting at the earth's rotation rate (within prescribed tolerances). These criteria define a drift curve. When the complete drift curve is located, program part A subtracts off a baseline temperature and filters the data by convolving the function $\sin(Ax)/(Ax)$, whose Fourier transform is unity at all frequencies up to the cut-off frequency of the antenna and zero for all higher frequencies [see Bracewell and Roberts (1954) and Bracewell (1965)]. This convolution filters out receiver noise components that cannot represent signals because they are at a frequency that cannot be accepted by the antenna. And this convolution also provides an exact method of interpolation to get temperatures at intermediate positions between the original data points. We neglect the effect of the true integrator and sampler which filter the data ahead of the computer. This is a good approximation, provided that the integration time is small compared with a half

cycle of the antenna cut-off frequency. For a drift curve with Haystack the cut-off frequency is 0.13 Hz at 15 GHz and 0.07 Hz at 8 GHz. In practice, 1 second of integration for 15 GHz observations and 2 seconds of integration for 8 GHz observations were used.

Program part A plots the original data points and the smoothed curve fit through them on the cathode ray tube display (CDC-280) and the operator may accept or reject a scan, or modify it before accepting it. Accepted scans are recorded on magnetic tape for further processing by program part B.

Program part B reads these processed scans output from A and aligns and averages scans taken at the same declination. Again, they are plotted on the cathode ray tube display and the operator may accept or reject scans. In program part B a correction for atmospheric attenuation and precession corrections back to 1950 may be applied as the operator directs. The correction for atmospheric attenuation was based on ground-level values for temperature, pressure, and humidity, and was calculated from formulas suggested by Allen (1967). The correction for precession is computed for the center of each scan. For very long scans in certain parts of the sky there may be some appreciable error in the precession correction for points on the ends of the scans. This error is a small part of an arcminute on the maps in this report. The averaged scans are recorded on magnetic tape for further processing by program part C.

Program part C reads the averaged scans output from B and further processes them to obtain a two-dimensional map. The tape from B contains only one averaged scan for each step in declination and these are placed in a two-dimensional matrix of numbers which is filtered by being convolved by $J_1(Ax)/(Ax)$. This function is the two-dimensional analogue of the filter function used in part A. Again the effect is to filter out only receiver noise and to provide interpolated temperatures.

The filtered temperatures represent the best estimate of the antenna temperature over the mapped region that is possible with the given data. Restoration [see Bracewell (1958)] could be performed at this time by choosing a different filter function instead of $J_1(Ax)/(Ax)$; however, this was not done for any of the maps presented in this report. If the data are spaced in declination in steps larger than $\lambda/(2D)$, where λ is the wavelength of observation and D is the diameter of the antenna, then one must increase A to correspond to a smaller antenna and larger beamwidth. If the data are spaced in declination in nonuniform steps, then there is no way to process the data with this program. The critical step interval $\lambda/(2D)$ for Haystack is 0.016 at 15 GHz, and 0.029 at 8 GHz.

It is also possible to increase A in the filter formula to smooth a map to a larger beamwidth. The equivalent antenna pattern for this modified map will not be the same as the antenna pattern of the same antenna used at a longer wavelength; to produce such an equivalent antenna pattern would require a more complicated filter function. However, such a modified map is useful in showing weak extended features which otherwise might be hidden in noise. A rough comparison with longer wavelength maps is also possible.

The filtered temperatures may be presented in many forms: as a matrix of numbers; as a shaded map; as a ruled surface map; or as a contour diagram, which is the form used for all the maps in this report. These maps are presented on the cathode ray tube display and simultaneously on another cathode ray tube to be photographed.

2. Continuum Fluxes and Other Source Parameters

There are at least two possible ways to obtain the flux of an individual source from such a map. One may fit the observed distribution with a source model function such as a two-dimensional

Gaussian and take the volume under the model to represent the integrated antenna temperature. For a two-dimensional Gaussian model the integrated antenna temperature is just

$$\int_{source} T_A(\Omega)\, d\Omega = (1.133)\, T_{peak}\, \Theta_\delta \Theta_\alpha \tag{3}$$

where T_{peak} is the peak temperature of the Gaussian and Θ_δ and Θ_α are its two widths to half-power in declination and right ascension.

Or, one may add up the actual temperature numbers in the two-dimensional matrix that corresponds to the map of the source. This summation may be performed by program part C. Bracewell and Roberts (1954) have shown that the integral under the surface defined by the antenna temperature map is given exactly by the sum of the numbers in such a matrix; no more complicated integration formula is needed.

The sources observed for this study fall into two classes: (1) Those with an angular structure that is small or comparable to the antenna beam. For these sources the Gaussian model is most appropriate and this method yields lower error estimates for the flux. (2) Those sources with an angular structure that is large compared with the antenna beam. None of these sources is adequately approximated by a two-dimensional Gaussian model or any other simple model, so the summation method was used to calculate the flux. The two methods were compared on the source W75-DR21 (see Table I). For a complex source, the integrated antenna temperature as determined from a Gaussian model is almost always smaller than the corresponding value determined by the summation method.

When the integral of T_a is known, one may use the well-known formula

$$S_\nu = \frac{2k}{\lambda^2} \frac{1}{\eta_\beta} \int_{source} T_A(\Omega)\, d\Omega \tag{4}$$

to get the flux density (S_ν) of a source if the beam efficiency (η_β) is known, or one may use this formula to get the beam efficiency as measured on a source whose flux is known. In this formula k is Boltzmann's constant, λ is the wavelength of observation and $d\Omega$ is an element of solid angle on the source. The constant $2k/(\lambda^2 \eta_\beta)$ is the (mapping efficiency)$^{-1}$ listed in Table I. In this formula, the $1/\eta_\beta$ factor converts the integrated antenna temperature to what would be observed using a lossless antenna that accepted radiation only in its main beam, the $2k/\lambda^2$ factor converts a brightness temperature to a specific intensity according to the Rayleigh-Jeans approximation to the Planck radiation law, and the integral of the specific intensity over the solid angle of the source gives the flux density. The beam efficiency η_β is defined by

$$\eta_\beta = \int_{main\ beam} G(\Theta, \phi)\, \frac{d\Omega}{4\pi} \tag{5}$$

where G is the antenna power gain. The region over which this integral is to be taken — the "main beam" — is somewhat arbitrary. For most antennas, this integral will change only very slowly as additional solid angle is included in the integral after the main lobe and perhaps the first sidelobes of the power pattern are included. Equation (4) is only strictly correct if this variation is negligible.

Since Eq. (4) is identical with the corresponding formula for source flux in terms of brightness temperature except for the $1/\eta_\beta$ factor, we may define an apparent brightness temperature

16

by $T_A(\Omega)/\eta_\beta$. This apparent brightness temperature will be equal to the true brightness temperature for any source whose angular structure is not smeared by the antenna beam, i.e., for a source that is completely resolved. It is thus analogous to the apparent flux density in the spectral plots given in this report. The apparent flux density will be equal to the true flux density for a source whose spectral features are completely resolved by the spectral resolution used.

Equation (4) is applicable to either a point or an extended source; however, for a source whose angular structure is small compared with the antenna beam, an alternative formula is usually more useful, namely:

$$S_\nu = \frac{2k}{A_e} T_A \quad , \tag{6}$$

where A_e is the effective collecting area of the antenna and T_A is the antenna temperature seen in one sense of polarization on the source. The constant k/A_e is ξ listed in Table I. The factor 2 in both these formulas is necessary whenever T_A refers to the antenna temperature measured in one sense of polarization and S_ν refers to the total flux of a source assumed to be unpolarized. For all the spectral plots in this report, the form of Eq. (6) was used without the 2 to convert measured antenna temperature to the corresponding Stokes parameters.

Fig. 3. Typical radio continuum spectrum of an H II region.

H II regions emit thermal continuum by free-free transitions. A typical spectrum from such a region is shown in Fig. 3. In the low frequency part of the spectrum the opacity is large and the radiation corresponds to an opaque black body. The brightness temperature is constant over this region of the spectrum and just equal to T_e, the electron kinetic temperature. As the frequency increases, the opacity drops according to the relationship [Oster (1961)]
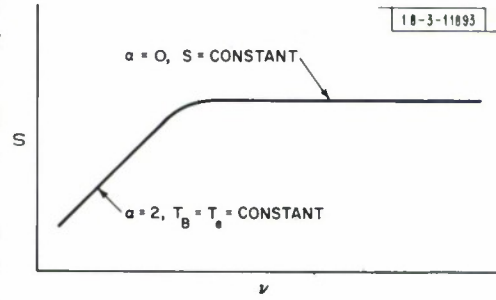
$$\tau_\nu \propto \frac{N_e^2 l}{T_e^{3/2}\nu^2} \log\left[\text{const.}\ \frac{T_e^{3/2}}{\nu}\right] \quad . \tag{7}$$

We have assumed a uniform medium inside the H II region, i.e., constant T_e and N_e, the electron density. For frequencies high enough so that $\tau_\nu \ll 1$ we have

$$S_\nu \simeq \frac{2k\nu^2}{c^2} T_e \tau_\nu \Omega_s \simeq \text{constant} \tag{8}$$

if we neglect the ν dependence in the logarithm. Ω_s is the solid angle subtended by the source and l is its thickness along the line of sight. The $-\log\nu$ term means that the flux will droop a bit from the constant line. The flux in this high frequency portion of the spectrum is approximately proportional to $\Omega_s N_e^2 l / T_e^{1/2}$. Therefore, if the source is resolved and if T_e is known from low frequency measurements or from excited hydrogen emission line measurement, it is possible to use the high frequency measurements to calculate the emission measure ($N_e^2 l$). If, furthermore, the distance to the source is known and it is assumed that l is the same as the transverse dimensions, we may estimate N_e.

The knee of the curve in Fig. 3 corresponds to $\tau \simeq 1$, and this occurs at $EM/\nu_k^2 \simeq 2.5$ [EM in $(el/cm^3)^2$ pc (parsecs); ν in MHz] for an assumed T_e of 10,000°K [see Kraus (1966)]. A typical value for EM might be 10^6 $(el/cm^3)^2$ pc and this corresponds to ν_k = 630 MHz. Turnover frequencies higher than this (corresponding to higher EM) have sometimes been observed [Ryle and Downes (1967)].

In principle then, two widely spaced points on the spectrum of such a source together with resolution in angle suffice for a calculation of the electron temperature, the emission measure, and perhaps the electron density. In practice the uncertainties will be large unless points below the knee of the curve can be measured.

Mezger and Henderson (1967) have shown how to carry out this analysis in detail for several assumed source models. This has not been done for this study for the following reasons: (1) The 8-GHz measurements are almost never low enough in frequency to define the knee of the curve or to get T_e; (2) As previously noted, those sources that are resolved in angle are complex and cannot be adequately described by any of the models suggested by Mezger and Henderson (1967); (3) For those sources to which this analysis might be applicable (such as W3 and W49) because of incipient but not complete angular resolution, the error estimates for the electron densities and masses are so large as to make the measurements meaningless. For a discussion of such problems, see Aikman (1968).

Table VI (page 33) contains fluxes determined as described above, angular sizes uncorrected for antenna beam smearing, and apparent spectral indices, i.e., straight line slopes between the two measured points.

B. Spectral Line

1. Real Time (AUTOCOR)

The real-time spectral line data reduction program (AUTOCOR) was written by G. H. Conant, Jr., to specifications by Dr. Sander Weinreb. It has been described in some detail by Conant and Meeks (1968) and so will only be outlined here. The description below refers to the latest version of this program which has been modified by Mrs. P. P. Crowther.

The AUTOCOR program operates in the U490 computer in the control environment of the antenna pointing system [Heart, et al. (1965)]. AUTOCOR accepts the 100 autocorrelation numbers from the digital autocorrelator every 100 ms and sums them into either of two arrays which represent "on" and "off" source data. It may switch back and forth between these two arrays every 100 ms for Dicke or frequency switching or it may sum exclusively into one array for an entire run in the unswitched mode. AUTOCOR also accepts low speed data from the synchronous and signal power detectors. During a calibration sequence this information allows AUTOCOR to compute the system noise temperature, and while running, to monitor changes in antenna temperature. The length of a run may be selected in half-minute steps from $\frac{1}{2}$ to 500 minutes. At the end of this time AUTOCOR performs the Fourier transform necessary to get from the accumulated autocorrelation numbers to the power spectrum (antenna temperature vs frequency). The total system temperature is used as a scale factor for this transform.

Four temperature points are calculated per frequency resolution interval (i.e., one point per 250 Hz for the 40-kHz window used for most of the spectra given in this report). Although two points per resolution interval suffice to specify the function exactly, experience has shown that it is very difficult to draw in the proper curve by hand if only two points per resolution interval are plotted. And straight lines connecting the points are even less accurate.

18

AUTOCOR prints the autocorrelation and temperature numbers on the high-speed printer and makes a printer plot of the temperatures. The spectrum is thus available to the observer within a few seconds after the end of each run. A magnetic tape record is also written by AUTOCOR at the end of each run. This record contains the accumulated autocorrelation numbers, the temperature numbers, the system temperature, the date and the times of the start and end of the run, and numerous other parameters pertaining to the run.

2. Post Real Time (SLREDUCE)

The post-real-time spectral line processing program (SLREDUCE), written for the CDC 3300, reads the magnetic tape records made by AUTOCOR, and further processes them to produce averaged spectra, Stokes parameters, and other polarization parameters. SLREDUCE has been described by Ball (1968) and will only be outlined here.

The instructions to SLREDUCE are punched on cards and tell the program which spectra to search for on the data tape and what to do with them. For circular polarization runs or runs on an unpolarized source, SLREDUCE may be directed to just average the runs with a frequency shift if necessary. If desired, this frequency shift may be recalculated by the program using the local oscillator synthesizer setting and a velocity calculation subroutine. This procedure was followed for all the data presented in this report. Errors in the pre-observation velocity calculation program are therefore unimportant. The largest error in this velocity calculation subroutine is due to the motion of the earth with respect to the earth-moon barycenter, which is neglected, and which amounts to about 0.015 km/sec at most. In order to align runs exactly, it may be necessary to shift some of them by a fraction of the separation of points on the frequency axis, i.e., to calculate interpolated temperatures. This may be done either by convolving the temperatures by $\sin(\Delta\nu)/(\Delta\nu)$ or by redoing the Fourier transforms with a shift. The latter method was used for aligning individual runs, but the convolution method was used to align averaged runs for restoration (see Sec. IV-B-4).

3. Stokes Parameters

The Stokes parameter definitions used in this report are those of Born and Wolf (1964) except that the electrical-engineering definition of the sense of circular polarization is used rather than the optical definition. This section contains abbreviated definitions and some relationships used in the data reduction.

The four Stokes parameters are defined as follows:

$$S_0 = T_R + T_L = T(\Theta) + T(\Theta + 90°)$$

$$S_1 = T(O) - T(90°)$$

$$S_2 = T(45°) - T(135°)$$

$$S_3 = T_R - T_L$$

where T_R and T_L are the antenna temperatures measured at right and left circular polarization, respectively, and where $T(\Theta)$ is the antenna temperature measured in linear polarization with a polarization position angle Θ. For a point source, these Stokes parameters defined in terms of antenna temperature differ from the Stokes parameters defined in terms of flux by a constant factor (see Sec. II). The polarization position angle for linear polarization is the angle from the

line of constant right ascension through the source around to the line corresponding to the E vector of the antenna projected onto the sky. Counterclockwise rotation is taken as positive. Values of Θ differing by 180° are equivalent except possibly for instrumental effects. Right circular polarization denotes clockwise rotation of the E vector as seen along the direction of propagation, i.e., the E vector traces a right-handed screw thread.

The above equations are used to process circular polarization data to determine S_3 and for one of two statistically independent determinations of S_o. To process the linear polarization data, the relation

$$T(\Theta) = T_A + T_B \cos 2(\Theta - \phi)$$

was used. The linear data consist of a number of values of antenna temperature (T_i) each with an associated polarization position angle (Θ_i). These were fit to the above equation in a least square sense, i.e., the quantity

$$\sum [T_i - T_A - T_B \cos 2(\Theta_i - \phi)]^2$$

was minimized for variations of T_A, T_B and ϕ, to give a best estimate of these three quantities at each frequency point. Then the Stokes parameters were calculated from

$$S_1 = 2 T_B \sin 2\phi$$

$$S_2 = 2 T_B \cos 2\phi$$

$$S_o = 2 T_A \quad .$$

This value of S_o from the linear polarization data was compared with the value of S_o from the circular polarization data as a consistency check and as a check on the relative gains of the feeds used for the different polarizations (see Table I).

Other useful quantities are the fraction linear polarization

$$p_L = \frac{\sqrt{S_1^2 + S_2^2}}{S_o} = \frac{2 T_B}{S_o} = \frac{T_B}{T_A}$$

the fraction circular polarization

$$p_c = \frac{S_3}{S_o} = \frac{T_R - T_L}{T_R + T_L} = \frac{T_R - T_L}{2 T_A}$$

and the total fraction polarization

$$p = \sqrt{p_c^2 + p_L^2} = \frac{\sqrt{S_1^2 + S_2^2 + S_3^2}}{S_o} \quad .$$

Note that with this definition a positive p_c corresponds to dominantly right circular polarization and a negative p_c to left. The ellipticity angle χ is obtained from

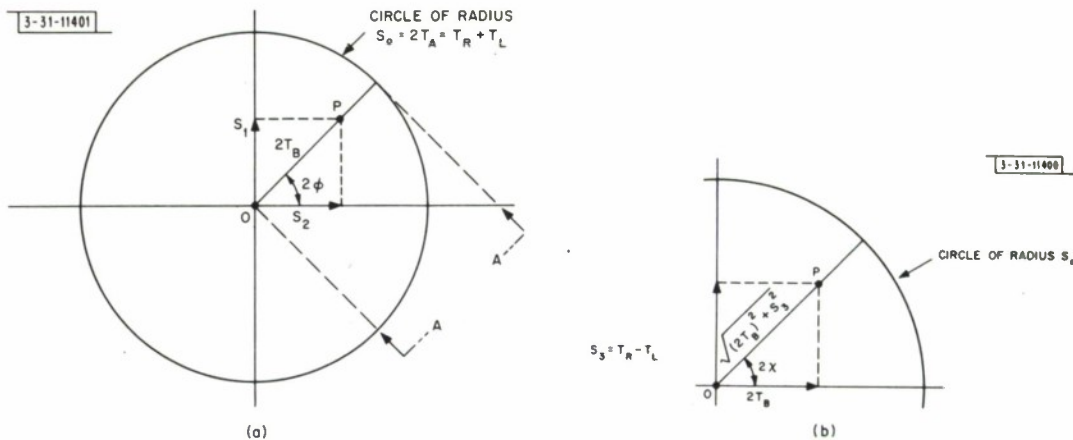$$\sin 2\chi = \frac{S_3}{\sqrt{S_1^2 + S_2^3 + S_3^3}} \quad .$$

20

Fig. 4. Three-dimensional Poincaré sphere: (a) Top view; (b) side view (section A-A above).

Figure 4, which is a sketch of the three-dimensional Poincaré sphere, is useful in visualizing these relations. The fraction polarization is represented by the fraction of the radius of the circle inside P, the fraction linear polarization is represented by the fraction of the radius inside the projection of P onto the equatorial plane, and the fraction circular polarization is represented by the fraction of the radius inside the projection of P along the vertical axis.

The angle 2ϕ is the longitude and the angle 2χ is the latitude on the Poincaré sphere. Further details on the Stokes parameters may be found in Born and Wolf (1965) and Ball (1968) gives details on how the Stokes parameters and other polarization parameters were obtained from the data.

4. Restoration

Two of the OH emission sources studied for this report (NGC 6334 and W75) are actually pairs of small diameter OH emission sources far enough apart to be distinguished with the 22 arc-minute beam of Haystack. When one of the two OH emission sources in such a region is being observed, the other emission source is on the side of the beam so that features from the off-beam position are present on the spectrum but with reduced amplitude. Using spectra taken with the antenna pointed at each of the emission points, and using a knowledge of the antenna beam pattern and the positions of the sources, it is possible to calculate the spectra which would have been seen if the sources could have been observed separately. This process will be referred to as "restoration," and the resulting spectra as "restored" spectra. The equations used in restoration are discussed below.

Let $T_1^R(\nu)$ and $T_2^R(\nu)$ be the restored antenna temperatures, i.e., the antenna temperatures (in a given sense of polarization) that would be measured with the other nearby source turned off. And let $T_1(\nu)$ and $T_2(\nu)$ be the actual antenna temperatures measured. Then we may write

$$T_1(\nu) = T_1^R(\nu) + \alpha T_2^R(\nu)$$

$$T_2(\nu) = T_2^R(\nu) + \alpha T_1^R(\nu)$$

where α is the fractional reduction in the antenna power pattern at the position of the other nearby source. α will not be a function of ν for the measurements at a given OH transition.

We have assumed that the antenna beam is symmetrical and that the antenna was pointing exactly at each source in turn; if either of these conditions fails to hold, then somewhat more complicated equations result. We also assume that the polarization properties of the antenna beam are the same at the off-axis and on-axis positions. We invert the above equations to obtain

$$T_1^R(\nu) = \frac{T_1(\nu) - \alpha T_2(\nu)}{1 - \alpha^2}$$

and

$$T_2^R(\nu) = \frac{T_2(\nu) - \alpha T_1(\nu)}{1 - \alpha^2}$$

However, these equations do not tell the whole story. Between two sources even this close together there is a noticeable differential Doppler shift, i.e., a difference in the components of the observer's motion projected onto the lines of sight to the sources. Since the differential Doppler varies as a function of the time of year (and even varies through a day, although the daily variation is negligible for the measurements described herein) it is necessary to restore spectra taken months apart before they can strictly be intercompared. Failure to do this may lead to apparent time variations when in fact the source itself is unchanged. This effect also makes it necessary to calculate for each source separately the conversion from frequency to velocity for the abscissa axis.

Successful restoration depends on knowing the antenna pattern and the source positions accurately and controlling the pointing to within a small fraction of a beamwidth. We have also tacitly assumed that the sources remain constant during the time interval between the measurements on the two sources. No noticeable difficulties were experienced with any of these requirements except with respect to the pointing of the Millstone antenna. This problem is discussed under the individual sources in Sec. V.

C. Interferometer Data Reduction

1. Introduction

This section describes a procedure which may be used to process interferometer data taken on an extended source. The data obtained from a two-antenna fixed-baseline interferometer may be presented in the form of a map, such as would be obtained from a single antenna with a particular pattern. The pattern of this equivalent single antenna depends on the source declination as well as the baseline parameters and for noncircumpolar sources the sidelobes are so bad that this technique is not recommended.

The procedure for calculating this equivalent antenna pattern and processing the data to produce such a map is given in this section. This procedure may be thought of as aperture synthesis with only two fixed antennas involved. An indication of how to generalize these results for any number of antennas and spacings (true aperture synthesis) is presented at the conclusion of this section.

The results of this section were used to write a computer program which was used to calculate several equivalent antenna patterns. The program, however, was not actually used to reduce any of the interferometer data for the reasons indicated in Secs. V-A and V-J.

2. Fringe-Amplitude Plane Coverage

From Rogers (1967b), Eqs. (7.2-51) and (7.2-52),

$$k = N \cos \delta_B \sin (L_S - L_B) \tag{9}$$

and

$$\ell = N \sin \delta_B \cos \delta_S - N \cos \delta_B \sin \delta_S \cos (L_S - L_B) \tag{10}$$

give the coverage of the fringe-amplitude plane for a fixed-baseline interferometer, where L_S and L_B are the local hour angles of the source and baseline, respectively, and δ_S and δ_B are the declinations of the source and baseline, respectively. N is the baseline length in wavelengths.

These equations may be written as

$$k = A \sin t \tag{11}$$
$$\ell = B - C \cos t \tag{12}$$

where

$$A = N \cos \delta_B \tag{13}$$

$$B = N \sin \delta_B \cos \delta_S \tag{14}$$

$$C = N \cos \delta_B \sin \delta_S \tag{15}$$

$$t = L_S - L_B \tag{16}$$

These equations represent an ellipse in the $k\ell$ plane as shown in Fig. 5. The whole ellipse, which corresponds to t running through a complete cycle, can be observed only for a circumpolar source.

Several special cases are worth noting in passing. If $\delta_B = 0$, which corresponds to an east-west baseline, $B = 0$, and the ellipse is centered on the origin. In this case, as we shall see below, it is sufficient to take only 12 hours of data instead of the full 24 hours. If $\delta_S = 0$, $C = 0$, and the ellipse degenerates into a horizontal line corresponding to an unending series of lobe

Fig. 5. Typical interferometer fringe plane coverage.
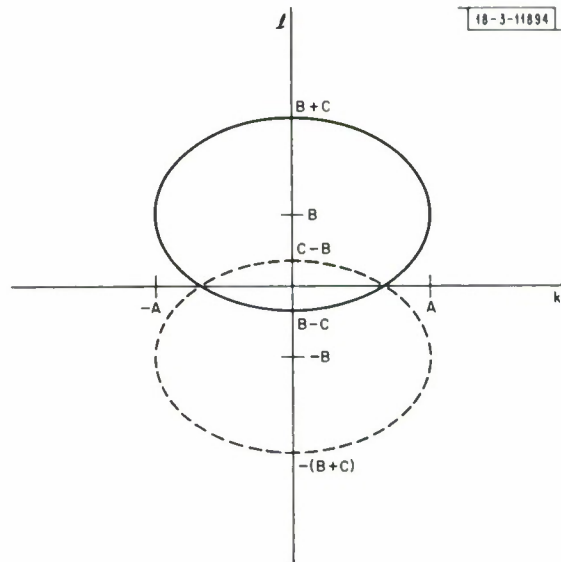
ambiguities in declination, or, in our terminology, an equivalent antenna pattern which has a series of zero decibel sidelobes in the declination direction. If $\delta_B = \delta_S$, we have B = C and the ellipse goes through the origin. This case has special significance for sources with assumed symmetry. And finally, if $\delta_B = \delta_S = 0$, B = C = 0 and the ellipse becomes a horizontal line through the origin.

3. Equivalent Antenna Pattern

The equivalent antenna pattern of any instrument is the response of that instrument to a point source at the origin of coordinates. For an interferometer, the data are usually reduced in such a way that a point source at the reference point on the sky produces a fringe amplitude of unity and a fringe phase of zero for all local hour angles.

If f(x, y) represents the sky brightness temperature inferred from the data, and F(k, l) represents the fringe amplitude and phase, then the two are connected by a two-dimensional Fourier transform

$$f(x, y) = \frac{1}{2\pi} \int_{-\infty}^{\infty} \int_{-\infty}^{\infty} e^{-i(kx+ly)} F(k, l) \, dk \, dl \quad . \tag{17}$$

The integral in practice can be carried out only over the range of k and l to which the instrument responds. If we take F to be zero for those values of k and l which cannot be measured, and a constant weighting function, then our result will correspond to the "principal solution" of Bracewell [Bracewell and Roberts (1954), Bracewell (1958)].

We therefore integrate along the ellipse of Fig. 5

$$f(x, y) = \frac{1}{2\pi} \int_0^{2\pi} e^{-i(kx+ly)} K(t) \, 2\pi R(t) \, \sigma(t) \, dt \tag{18}$$

where

$$R^2(t) = l^2 + k^2 = A^2 \sin^2 t + B^2 - 2BC \cos t + C^2 \cos^2 t \tag{19}$$

and the other quantities are indicated in Fig. 6. We think of σ tending to zero and K to ∞ while their product remains finite. The product $K\sigma R$ represents the data (which we have taken to be
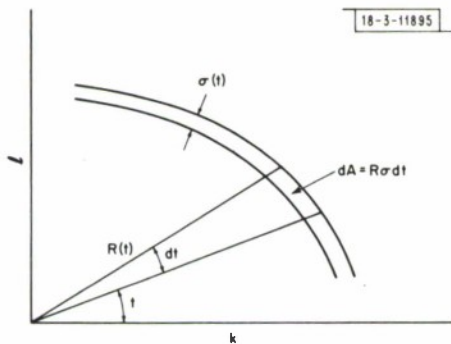

Fig. 6. Area differential in the k-1 plane.

unity for all t) times an arbitrary weighting function. This arbitrary weighting function is analogous to the feed illumination for a single antenna. We have rather limited control over the equivalent antenna pattern by varying this weighting function.

If we define

$$W(t) \equiv K(t)\ \sigma(t)\ R(t) \tag{20}$$

then we may write

$$f(x, y) = 2\, \mathcal{R}_e \int_0^{2\pi} \exp\left[-i(xA\sin t + yB - yC\cos t)\right]\ W(t)\ dt \quad . \tag{21}$$

Note that the integral in Eq. (21) will be complex, but f, since it represents a brightness or brightness temperature, must be real. The problem is that we have taken the integral only over a region of the $k\ell$ plane that is not symmetrical about the origin. If we demand that f be real, we have from Eq. (17) that

$$F^*(-k, -\ell) = F(k, \ell) \tag{22}$$

where * represents complex conjugation. In effect, we have measured the fringe phase and amplitude not only along the original ellipse, shown in Fig. 5 by a solid line, but also along another ellipse, obtained from the first ellipse by reflection through the origin. This second ellipse is shown in Fig. 5 by a dashed line. If we add the integrals along the two ellipses, we obtain the expression in Eq. (21).

Now if we substitute, according to Fig. 7

$$S^2 = (xA)^2 + (yC)^2 \tag{23}$$

and

$$xA = S\cos\phi \tag{24}$$

and

$$yC = S\sin\phi \tag{25}$$

then

$$xA\sin t - yC\cos t = S\cos\phi \sin t - S\sin\phi \cos t = -S\sin(\phi - t) \tag{26}$$

and we get

$$f(x, y) = 2\, \mathcal{R}_e\ e^{-iyB} \int_0^{2\pi} \exp\left[+iS\sin(\phi - t)\right]\ W(t)\ dt \quad . \tag{27}$$

For $W(t) = 1$, this integral can be done:

$$f_1(x, y) = 2\, \mathcal{R}_e\ e^{-iyB} \int_0^{2\pi} \exp\left[iS\sin(\phi - t)\right]\ dt = 4\pi \cos(yB)\ J_0(S) \quad . \tag{28}$$

Fig. 7. Typical point on the source in the xA-yC plane.

25
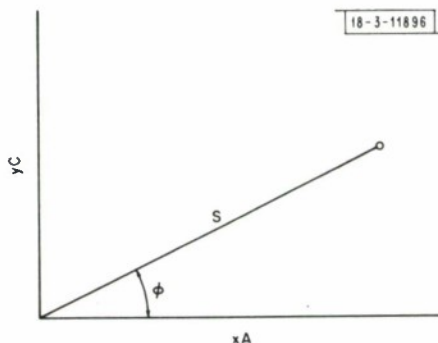
So for this case we have an equivalent antenna pattern with a width to half-power of S = 1.52 (along the x axis) and a first (negative) sidelobe of -0.403 at S = 3.83, y = 0. We shall see later what this means for certain specific values of A and C.

We return now to the general case in Eq. (27) and assume that W(t) is expanded in a Fourier series,

$$W(t) = \sum_{n=-k}^{k} M_n e^{int} \tag{29}$$

W(t) and M_n may be complex. So we get

$$f(x, y) = 2 \, \mathcal{R}_e \, e^{-iyB} \sum_n M_n \int_0^{2\pi} \exp \{i \, S[\sin(\phi - t) + nt]\} \, dt \tag{30}$$

or

$$f(x, y) = 2 \, \mathcal{R}_e \, e^{-iyB} \sum_n M_n \int_0^{2\pi} e^{i[S \sin\Theta + n(\phi - \Theta)]} \, d\Theta \tag{31}$$

which is

$$f(x, y) = 4\pi \, \mathcal{R}_e \, e^{-iyB} \sum_n M_n J_n(S) \, e^{in\phi} \tag{32}$$

So we see that an expansion of W(t) in a Fourier series corresponds to an expansion of f(x, y) in Bessel J_n functions, and this relationship may be used in the data processing.

Partial coverage of the ellipse of Fig. 5 corresponding to a noncircumpolar source, may be handled by setting W(t) = 0 for that range of t for which the source is not observable, and then performing the Fourier series expansion of Eq. (29) with sufficient terms to approximate the discontinuous function. It is not correct, however, to determine the Fourier coefficients to fit the data over the observable range and allow W(t) to be nonzero over the unobservable range, because this corresponds to arbitrarily introducing $k\ell$ plane coverage that was not in fact observed.

4. Sampling the Data

We know from the sampling theorem that a band-limited function need be measured only at uniform intervals equal to one-half of the wavelength at the maximum frequency. If W(t) is a band-limited function, then we may specify Δt, the maximum time interval between observations, and the appropriate k in Eq. (29).

It is immediately clear that W(t) cannot be a band-limited function of t unless $F(k, \ell)$ is band-limited, and this can only be the case if f(x, y) is spatially limited, i.e., only if f = 0 for $S > S_o$. But this will always be approximately true in practice because f will be limited by the beam-width of a single antenna, if not by the source itself.

So consider a point source at S_o, ϕ_o, which we take to be a representative point on the edge of an extended but limited source. Then since

$$F(k, \ell) = 2\pi \int_{-\infty}^{\infty} \int_{-\infty}^{\infty} f(x, y) \, e^{i(kx + y\ell)} \, dxdy \tag{33}$$

26

we get

$$F(k, \ell) = 2\pi \, e^{i(kx_o + \ell y_o)} \tag{34}$$

or

$$W(t) = 2\pi \exp[iy_o B - iS_o \sin(\phi_o - t)] \tag{35}$$

for this case.

To find whether this is a band-limited function of t, we consider $\overline{F}(\omega)$ defined by

$$\overline{F}(\omega) = \int_0^{2\pi} W(t) \, e^{i\omega t} \, dt \tag{36}$$

which is

$$\overline{F}(\omega) = 2\pi \, e^{iy_o B} \int_0^{2\pi} \exp\{-i[S_o \sin(\phi_o - t) + \omega t]\} \, dt \tag{37}$$

or

$$\overline{F}(\omega) = 2\pi \, e^{i(y_o B + \phi_o \omega)} \int_0^{2\pi} e^{-i[S_o \sin u + \omega u]} \, du \tag{38}$$

where $u = \phi_o - t$. This integral gives us

$$\overline{F}(\omega) = -(2\pi)^2 \, e^{i(y_o B + \phi_o \omega)} J_\omega(S_o) + \text{other terms for } \omega \text{ noninteger} \tag{39}$$

Because $J_\omega(S_o)$ does not become precisely zero for all $\omega > \omega_o$, $W(t)$ is not strictly a band-limited function. But there is a practical cut-off frequency ω_o for which $J_\omega(S_o) < \epsilon$ for all $\omega > \omega_o$, where ϵ may be chosen as small as we please. For $\epsilon \sim 10^{-4}$ we have as an approximation that

$$\omega_o \simeq \frac{3S_o + 8}{2} \quad \text{and} \quad \Delta t = \frac{\pi}{\omega_o} \simeq \frac{2\pi}{3S_o + 8} \tag{40}$$

This practical cut-off frequency corresponds approximately to the naive cut-off that we may calculate from Fig. 8 which shows an $f(x, y)$ specified at the critical interval corresponding to the maximum values of k and ℓ. We get $\Delta\phi \simeq \pi/S_o$ from Fig. 8 and for large S_o this is just $3/2$ of the Δt above.
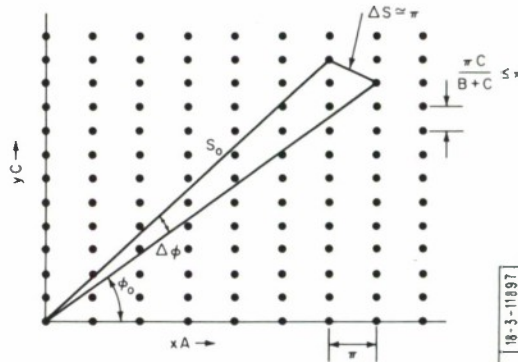

Fig. 8. Sampling in the xA-yC plane.

TABLE IV
HAYSTACK-MILLSTONE INTERFEROMETER ON CAS A

Hardware parameters

$$\delta_B = 43°2667$$

$$L_B = -153°3083$$

$$N = 3800 \text{ (approximate, at 1665 MHz)}$$

Source parameters

$$\delta_s \simeq 58°6$$

$$x_{max} \simeq y_{max} \simeq 3'$$

System parameters

$$A = 2767$$

$$B = 1357$$

$$C = 2362$$

$$S_o \simeq 3.28$$

Conversion factors

Units of S to arcminutes along x axis $= \dfrac{1}{A}\dfrac{10800'}{\pi} = 1.24$

along y axis $= \dfrac{1}{C}\dfrac{10800'}{\pi} = 1.46$

Equivalent antenna pattern parameters

Width between half-power points in declination $(y) = 3.1$

in right-ascension $(x) = 3.77$

Location of first sidelobe (-0.403): $y = 0$, $x = 4.75$

Data characteristics

Maximum sampling interval $\Delta t = \dfrac{1440^m}{3S_o + 8} = 81^m$

Maximum Fourier component $k = 18$

5. Specific Numeric Example

Table IV lists the relevant parameters for the source Cas A as observed with the Haystack-Millstone interferometer system.

Fig. 9. Interferometer equivalent antenna pattern (Haystack-Millstone on Cas A at 1665 MHz).
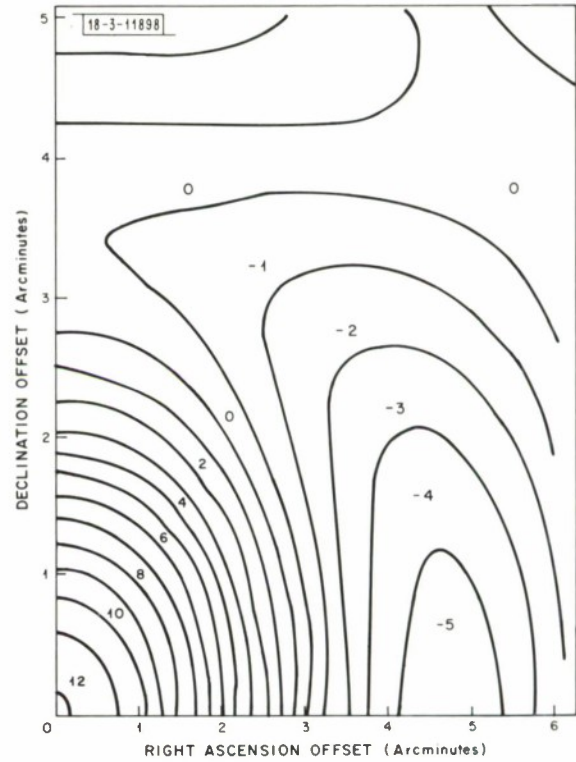
A contour diagram of one quadrant of the equivalent antenna pattern for this case is shown in Fig. 9.

6. Conclusion

Because it is possible in principle to recover the original fringe amplitude and phase data from the map, it is clear that in presenting the data in the form of a map we have not discarded any information contained in the data. However, we may not have made full use of other knowledge about the source. For example, we assumed in Sec. IV-C-4 that the source was spatially limited, but we have not incorporated this assumption fully into the map. Specifying that $f(x, y)$ shall be zero outside some region of x and y is equivalent to convolving $F(k, \ell)$ by the Fourier transform of a function which is zero outside the prescribed region of x and y. This convolution will smooth our original $F(k, \ell)$, which was essentially a line function along the ellipses, into a band. It will also perform some smoothing along the ellipses. However, there is no necessity for actually performing this convolution; it is preferable to manipulate $f(x, y)$.

The flux in the map

$$\text{Flux} = \int_{-\infty}^{\infty} \int_{-\infty}^{\infty} f(x, y) \, dxdy = F(0, 0) = 0 \tag{41}$$

is zero because we have not incorporated the information from single antenna measurements into the map. However, this may be done by adding a constant to f, unless the source is so large that it is resolved by the single antennas used.
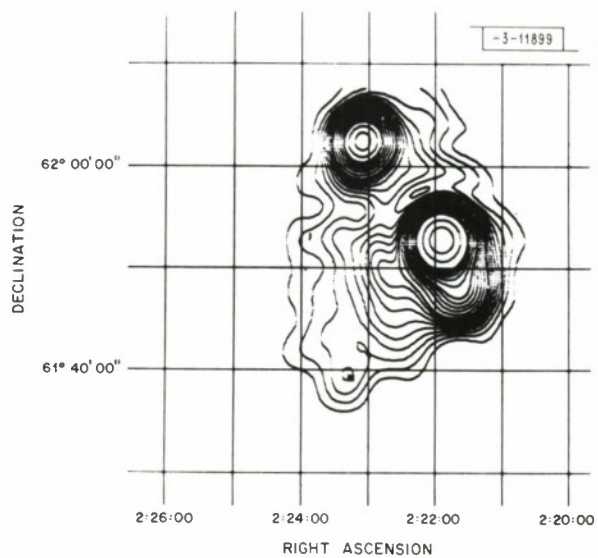
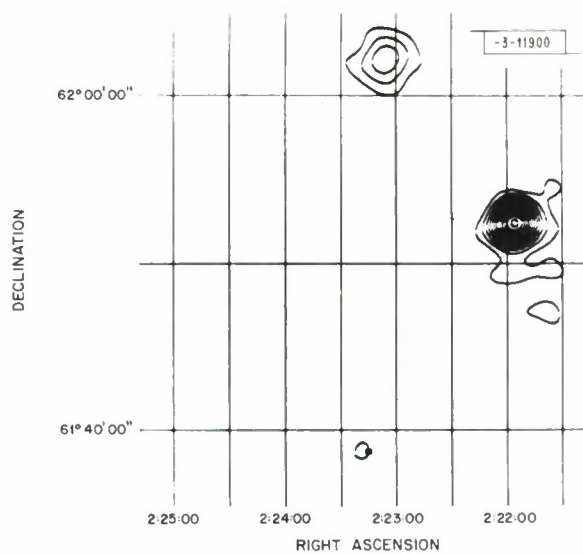Fig. 10.   W3 region map made at 7.795 GHz at Haystack.

Fig. 11.   W3 region map made at 15.5 GHz at Haystack.

In more general terms, we may incorporate any additional kℓ plane coverage by adding the corresponding functions in the xy plane, provided that there is no overlap in the corresponding kℓ plane coverages. This allows us to do true aperture synthesis by adding a series of individual maps made by this technique.

V. SOURCES – DATA AND PRELIMINARY INTERPRETATION

Data of one kind or another were taken for this study on nine regions of the sky that either contain OH emission sources or are interesting in relation to the problem of understanding the anomalous OH emission. These data are presented in this section together with a discussion of some of the other published data on these sources.

A number of continuum maps of some of these sources were made and some essential characteristics of the maps are summarized in Table V. All of the maps were made with the Haystack antenna using the drift curve technique. A number of spectra of the OH emission from some of these sources were made and some essential characteristics of the spectra are summarized in Table VI. These maps and spectra are presented in this section under the individual sources.

A number of individual sources were separated out on the continuum maps, and their pertinent parameters are summarized in Table VII. Similarly, a number of OH emission features were separated out on the spectra, and the pertinent parameters for these features are summarized in Table VIII. As an aid in this process, we used a computer program that compares the spectral data with a model consisting of a series of uniformly polarized, Gaussian-shaped features that add incoherently in any region of overlap [Ball and Meeks (1968)].

A. W3 (IC1795/IC1805)

W3 is one of the most intensively observed of the sources studied for this report. Radio continuum observations have been made by Akabane, et al. (1967), Mezger and Henderson (1967), Mezger, et al. (1967), Aikman (1968), and others [see Aikman (1968) for a list]. Excited hydrogen lines have been observed in this region by Mezger and Höglund (1967), Dieter (1967), and Reifenstein (1968). The OH emission from this region has been observed with a single antenna by Weaver, et al. (1965), Weinreb, et al. (1965), Dieter, et al. (1966b), Barrett and Rogers (1966), Davies, et al. (1966), Meeks, et al. (1966), Weaver, et al. (1968), and Coles, et al. (1968), and with an OH interferometer by Rogers, et al. (1966), Cudaback, et al. (1966), Davies, et al. (1967), Moran, et al. (1967), Moran, et al. (1968), and by Raimond and Eliasson (1969). The $^2\pi_{1/2}$, J = 1/2 line of excited OH has been detected from this source by Zuckerman, et al. (1968), the $^2\pi_{3/2}$, J = 5/2 line by Yen, et al. (1969), and the $^2\pi_{1/2}$, J = 5/2 line by P. Schwartz (1969, private communication).

This region has been photographed and studied optically. The W3 region from the Palomar Sky Survey prints was reproduced in Rogers, et al. (1966) and in Weaver, et al. (1968). Ishida and Akabane (1968) show a photograph taken at the Tokyo Astronomical Observatory. Aikman (1968) studied in some detail the association of the radio continuum sources in this region with their optical counterparts.

A contour map made at Haystack at 7.795 GHz is shown in Fig. 10 and one made at 15.5 GHz is shown in Fig. 11. Although this is clearly an extended complex region, it is divided into three principal sources listed in Table VII. The position of the OH emission source is coincident within the error bars with W3γ (G133.9 + 1.0). This continuum source has been discussed in some detail by Mezger, et al. (1967) and by Aikman (1968).

TABLE V

SPECIFICATIONS FOR CONTINUUM MAPS

Figure [*]	Source Name	Center Frequency (GHz)	Nominal Band-width (MHz)	Center Wave-length (cm)	Feed	Front End	Polarization	Date	Number of Scans	$\Delta\delta$ (deg)	Number [†] Scans per Declination Step	Filter Beam-width (deg)	Minimum Effective Integration Time (sec)	Calculated [‡] rms Noise Antenna Temperature (°K)	Peak Negative Antenna Temperature (°K)	Contours [§] of Antenna Temperature (°K)
10	W3	7.795	10	3.846	Radar horn	Maser	Left circular	2/9/67	23	0.025	1	0.073	3.7	0.02	0.06	0.05, 0.5, 0.05; 0.5, 1.0, 0.1; 1.0, 2.0, 0.2; 2.0, 4.0, 1.0
11	W3	15.5	1000	1.934	Rotatable horn	New TDA	Vertical	9/19/67 9/20/67	83	0.015	6, 3, 2	0.036	3.7	0.03	0.21	0.2, 2.6, 0.2; 2.0, 3.2, 0.4
15	W28, W29	7.795	10	3.846	Radar horn	Maser	Left circular	6/8/68 6/21/68 7/4/68	125	0.03	2	0.072	3.8	0.02	0.07	0.1, 1.0, 0.1; 1.0, 2.0, 0.2; 2.0, 3.2, 0.4
16	W28	15.5	1000	1.934	Rotatable horn	New TDA	Vertical	5/2/68 5/3/68	54	0.015	3, 2	0.036	1.9	0.029	0.17	0.2
17	W28	15.5	1000	1.934	Rotatable horn	New TDA	Vertical	5/2/68 5/3/68	54	0.015	3, 2	0.072	3.8	0.026	0.06	0.1, 0.2
19	W43	7.795	10	3.846	Radar horn	Maser	Left circular	7/9/68	68	0.03	2, 1	0.072	1.7	0.03	0.09	0.1, 1.0, 0.1; 1.0, 2.0, 0.2; 2.0, 5.4, 0.2
20	W43	15.5	1000	1.934	Rotatable horn	New TDA	Vertical	5/8/68 5/9/68 6/26/68	64	0.015	2	0.036	1.7	0.04	0.19	
22	W44	7.795	10	3.846	Radar horn	Maser	Left circular	6/6/68 6/7/68	58	0.03	2	0.079	3.8	0.02	0.07	0.1, 1.0, 0.1; 1.0, 1.8, 0.2
23	W44	15.5	1000	1.934	Rotatable horn	New TOA	Vertical	5/8/68	45	0.015	1	0.036	0.9	0.05	0.21	0.2, 1.2, 0.2
25	NGC 6334	7.795	10	3.846	Radar horn	Maser	Left circular	4/23/68 6/22/68	45	0.03	2	0.073	4.3	0.018	0.18 [′]	0.2, 2.0, 0.2; 2.0, 5.0, 0.5
26	NGC 6334	7.795	10	3.846	Radar horn	Maser	Left circular	4/23/68 6/22/68	45	0.03	2	0.073	4.3	0.018	0.18 [′]	0.2, 2.0, 0.2; 2.0, 5.0, 0.5
27	NGC 6334	15.5	1000	1.934	Rotatable horn	Old TDA	Vertical	3/4/66 4/3/66	53	0.015	2, 1	0.036	1.1	0.13	0.28	0.2, 1.0, 0.2
38	W49	8	1000	3.747	Clavin	TOA	Vertical	4/4/66 9/17/66	20	0.03	4, 3	0.073	5.3	0.035	0.07	0.1, 1.0, 0.1; 1.0, 2.0, 0.2; 2.0, 3.5, 0.5
39	W49	15.5	1000	1.934	Rotatable horn	Old TDA	Vertical	2/27/66 4/3/66	27	0.015	5, 3, 2	0.036	1.8	0.105	0.16	0.2, 2.2, 0.2
43	W51	8	1000	3.747	Clavin	TOA	Vertical	9/16/66	18 [¶]	0.03	2	0.072	3.6	0.042	0.07	0.2, 1.0, 0.2; 1.0, 3.0, 0.5; 3.0, 6.0, 1.0
44	W51	15.5	1000	1.934	Rotatable horn	Old TDA	Vertical	10/3/66	22	0.015	3, 2	0.036	1.8	0.105	0.24	0.4, 2.0, 0.4; 2.0, 4.0, 0.5
46	W75	7.795	10	3.846	Radar horn	Maser	Left circular	7/18/68 7/19/68	130	0.03	7 – 2	0.072	4.7	0.017	0.1 (0.05) [•]	0.05, 0.1; 0.2, 1.0, 0.2; 1.0, 3.0, 0.5
47	W75	15.5	1000	1.934	Rotatable horn	New TOA	Vertical	8/4/68	193	0.015	6 – 2	0.036	2.3	0.033	0.16 (0.08) [•]	0.2, 1.0, 0.2; 1.0, 1.8, 0.4

[*] The coordinates on all the maps are epoch 1950.

[†] For the central region, sometimes the edges have fewer scans.

[‡] Approximate values, based on the numbers in Table III.

[§] The notation a_1, a_2, a_3; where a stands for the numbers in this column, means that contours are plotted from a_1 to a_2 in steps of a_3. The units are °K of antenna temperature.

[¶] But four of the scans used only 0.5–GHz bandwidth.

[′] The noise is larger, probably because of the low elevation.

[•] The number in parentheses applies to the top half of the map alone.

			Pointing Position *											Number of Runs	
Figure	Source Name	Transition (MHz)	α (1950) hr min sec	δ (1950) deg min sec	l^{II} (deg)	b^{II} (deg)	Antenna	Feed	Polarization	T_{System} (°K)	Mode	Date		Total	At Each ν
13 †	W3	1665	2 23 16.3	61 38 57	133.949	1.064	Haystack	Clavin	Linear	370	Dicke	11/29/65 11/30/65		15	7
							Haystack	Andrew	Circular	370	Dicke	12/ 7/65 3/ 7/66 3/12/66 10/ 6/66		15	6
14 †	W3	1665	2 23 16.3	61 38 57	133.949	1.064	Haystack	Clavin	Linear	260	Dicke	3/ 3/69 3/ 6/69		29	6
							Haystack	Andrew	Circular	250	Dicke	9/21/67 9/23/67		18	7
18 ‡	W28	1720	17 58 48	−23 17	6.76	−0.27	Millstone Millstone	Horn Horn	Linear Circular	260 260	Unswitched Unswitched	4/ 9/68. 3/30/68 3/31/68		6 6	6 6
21	W43	1612	18 45	−1 45.5	30.99	0.08	Millstone	Horn	Circular	230	Unswitched	7/11/68		14	7
24 ‡	W44	1720	18 53 34	1 14	34.63	−0.45	Millstone Millstone	Horn Horn	Linear Circular	260 260	Unswitched Unswitched	4/ 9/68 3/30/68 3/31/68		4 6	4 6
28 †	NGC 6334N	1665	17 17 33.5	−35 45 35	351.37	+0.63	Haystack	Clavin	Linear	420	Dicke	9/ 2/66 9/23/66 10/ 2/66		15	14
							Haystack	Andrew	Circular	420	Dicke	10/ 4/66 10/ 7/66		7	5
29 †	NGC 6334S	1665	17 16 50.1	−35 53 17	351.18	+0.67	Haystack	Clavin	Linear	420	Dicke	9/21/66 9/23/66 10/ 2/66		14	6
							Haystack	Andrew	Circular	420	Dicke	10/ 4/66 10/ 7/66		10	8
30 †	NGC 6334N	1667	17 17 33.5	−35 45 35	351.37	+0.63	Haystack	Clavin	Linear	420	Dicke	9/ 2/66 9/30/66 10/ 1/66		10	9
							Haystack	Andrew	Circular	420	Dicke	10/ 5/66 10/ 8/66		12	6
31 †	NGC 6334S	1667	17 16 50.1	−35 53 17	351.18	+0.67	Haystack	Clavin	Linear	420	Dicke	9/24/66 9/30/66 10/ 1/66		10	5
							Haystack	Andrew	Circular	420	Dicke	10/ 5/66 10/ 8/66		11	8
32	NGC 6334N	1665	17 17 32.1	−35 44 15	351.18	+0.64	Haystack	Andrew	Circular	260	Unswitched	5/ 1/68 5/20/68		10	6
33	NGC 6334S	1665	17 16 36.3	−35 54 57	351.13	+0.70	Haystack	Andrew	Circular	260	Unswitched	5/ 1/68 5/20/68		14	6
34	NGC 6334N	1667	17 17 32.1	−35 44 15	351.38	+0.64	Haystack	Andrew	Circular	260	Unswitched	5/ 1/68 5/20/68		6	4
35	NGC 6334S	1667	17 16 36.3	−35 54 57	351.13	+0.74	Haystack	Andrew	Circular	260	Unswitched	5/ 1/68 5/20/68		7	5
36	NGC 6334S	1667	17 16 36.3	−35 54 57	351.13	+0.70	Millstone	Horn	Circular	230	Unswitched	1/21/68 1/24/68		12	8
40 †	W49	1665	19 07 54	9 01 46	43.19	−0.00	Haystack	Clavin	Linear	360	Dicke	7/ 5/66 7/ 6/66		24	6
							Haystack	Andrew	Circular	370	Dicke	3/12/66 10/ 6/66 10/ 7/66 10/ 8/66		16	4
41 †	W49	1667	19 07 54	9 01 46	43.19	−0.00	Haystack	Clavin	Linear	360	Dicke	4/12/66 4/13/66		12	6
							Haystack	Andrew	Circular	370	Dicke	3/13/66		9	2
42	W49	1720	19 07 54	9 00 38	43.19	−0.00	Millstone	Horn	Circular	260	Unswitched	7/16/66		4	4
45 †	W51	1665	19 21 33	14 23	49.48	−0.38	Haystack	Andrew	Linear	380	Dicke	9/20/66 9/22/66		11	9
							Haystack	Andrew	Circular	380	Dicke	10/ 5/66		6	6
48	W75N	1665	20 36 51	42 25 30	81.86	0.76	Millstone	Horn	Circular	200	Unswitched	7/22/68		6	2
49	W75S	1665	20 37 28	42 12	81.75	0.54	Millstone	Horn	Circular	200	Unswitched	7/22/68		3	3

TABLE VI
SPECIFICATIONS FOR STOKES PARAMETER PLOTS

* The pointing position is the position actually used for the observations, but is not necessarily the best known position for the OH emission. Refer to the text for each source.

† The S_a curves are from the linear data, the S_3 curves from the circular.

‡ The plot is the average of circular and linear.

TABLE VII

CONTINUUM SOURCE SUMMARY

Source Name	α (1950) hr	min	sec	δ (1950) deg	min	l^{II} (deg)	b^{II} (deg)	7.795 or 8 GHz Apparent Angular Size (arcminutes)	Peak Antenna Temperature (°K)	Peak Apparent Brightness Temperature (°K)	Flux (from temperature sum) (fu)	Flux (from Gaussian) (fu)	15.5 GHz Apparent Angular Size (arcminutes)	Peak Antenna Temperature (°K)	Peak Apparent Brightness Temperature (°K)	Flux (from temperature sum) (fu)	Flux (from Gaussian) (fu)	Spectral Index δ
W3α	02	21	55	+61	52.5	133.72	+1.22	4.4	4.8	10.5	60 ± 6	35	2.0	2.6	8.0	41 ± 1	32	−0.6
W3β	02	23	05	+62	02.5	133.79	+1.42	5.0	1.5	3.3	17 ± 3	14	3.0	0.8	2.3	17 ± 4	20	0
W3γ	02	23	20	+61	39	133.96	+1.07	5?	0.2	0.5	2.0 ± 0.5	2.0	−	0.2	0.7	2.4 ± 1	0.3	+0.3
NGC 6334α	17	16	57	−35	52	351.21	+0.67	13 × 7	5.0	11.0	224 ± 25	170	2.5 × 3	1.2	3.6	185 ± 70	23	−0.3
NGC 6334β	17	17	23	−35	47	351.33	+0.64						3 × 4	1.1	3.3		33	−
NGC 6334γ	17	17	10	−35	49	351.28	+0.66						3 × 4	1.1	3.2		32	−
NGC 6334δ	17	16	25	−36	02	351.01	+0.66	7.5 × 8	2.1	4.6	52 ± 5	47	−	−	−	−	−	−
NGC 6334ε	17	17	30	−36	00	351.17	+0.50	6 × 5.5	1.6	3.4	26 ± 4	20	−	−	−	−	−	−
NGC 6334ζ	17	19	50	−35	52	351.54	+0.19	9 × 5	1.1	2.3	19 ± 5	18	−	<0.2	<0.6	<40	−	−
W28	17	57	45	−23	20	6.61	−0.10	(30 ×20) ¶	0.4	1.0	81 ± 30	100	−	−	−	68 ± 40	−	−0.3
W28C	17	57	45	−23	20	6.61	−0.10	6 × 8	0.6	1.4		12	−	−	−	−	−	−
M20	17	59	18	−23	01	7.04	−0.25	7.5 × 8	0.7	1.5	21 ± 3	16	−	0.2	0.7	25 ± 4	−	+0.3
W28S	17	57	30	−24	04	5.94	−0.40	5.5 × 6	1.5	3.3	33 ± 4	18	−	−	−	−	−	−
W29	18	00	35	−24	22.5	6.04	−1.18	6 × 6	3.2	7.0	146 ± 20	42	−	−	−	−	−	−
W43	18	45	03	−01	59	30.80	−0.04	6 × 6.5	5.9	12.9	180 ± 20	86	4.5 × 5	2.0	5.4	174 ± 40	72	−0.1
W43S	18	43	28	−02	44	29.95	−0.03	6.5 × 5	1.6	3.5	31 ± 3	19	−	−	−	−	−	−
W44	18	54		+01	15	34.69	−0.53	(25 ×18) ¶	0.6	1.3	116 ± 20	(102) ¶	−	−	−	65 ± 10	−	−0.8
W44W	18	50	50	+01	11	34.27	+0.14	5 × 4.5	1.9	4.0	22 ± 3	16	2.5 × 2.5	1.2	3.4	36 ± 6	30	+0.7
W49A	19	07	52	+09	01.5	43.19	+0.01	4.5 × 5	3.7	13.1	63 ± 6	46	2.5 × 3	2.4	7.2	62 ± 10	45	−0.0
W49B	19	08	42	+09	01	43.27	−0.18	5 × 5	0.9	3.1	16 ± 3	12	2.5 × 3?	0.5	1.6	17 ± 5	10?	+0.0
W51α	19	21	23	+14	25	49.50	−0.38	4.5 × 5	6.4	23.0	113 ± 20	81	2.5 × 3	4.1	12.7	95 ± 20	77	−0.2
W51β	19	20	55	+14	21.5	49.40	−0.30	5 × 5	1.7	6.0	35 ± 5	23	4 × 3	0.9	2.7	30 ± 5	27	−0.2
W75/DR21	20	37	14	+42	09	81.68	+0.54	4.5 × 4.5	2.9	6.3	20	20	2 × 2	2.1	5.8	20	20	0

* The error limits for the positions are about ± 1 arcminute or ±20 percent of the stated apparent angular size, whichever is larger.

† The apparent angular sizes are given to the nearest half arcminute and are not corrected for antenna resolution.

‡ The error limit for the peak antenna temperature is given by the peak noise temperature in the corresponding entry in Table V, or ±10 percent, whichever is larger.

§ The spectral indices were computed from those fluxes that are based on the sum of the antenna temperature.

¶ Values enclosed in parentheses are estimates.

34

TABLE VIII

OH EMISSION FEATURE SUMMARY *

Source Name	Transition (MHz)	Feature No.	Velocity ‡ (km/sec)	S_o Peak Flux (fu)	Feature Width § (kHz)	(km/sec)	Instrumental Resolution (kHz)	(km/sec)	P_c (percent) ¶	P_L (percent) ¶	Center Polarization Position Angle (deg)	Remarks
W3	1665	1	−49.1 ± 0.1	54 ± 5	1.5 ± 0.5	0.27 ± 0.1	1	0.18	−50 ± 15	14 ± 14	170 ± 90	
		2	−46.4 ± 0.1	137 ± 15	3.7 ± 0.5	0.68 ± 0.1	1	0.18	−94 to −100	<10	−	
		3	−45.4 ± 0.1	170 ± 20	3.1 ± 0.5	0.55 ± 0.1	1	0.18	−95 to −100	17 ± 5	65 ± 40	
		4	−45.1 ± 0.1	245 ± 30	2.5 ± 0.5	0.45 ± 0.1	1	0.18	+91 ± 4	55 ± 12	55 ± 12	Blended
		5	−44.6 ± 0.1	78 ± 9	2.8 ± 0.5	0.50 ± 0.1	1	0.18	−80 to −100	34 ± 10	105 ± 40	
		6	−43.7 ± 0.1	147 ± 18	1.9 ± 0.5	0.35 ± 0.1	1	0.18	+83 ± 5	21 ± 5	165 ± 60	
		7	−43.1 ± 0.1	39 ± 5	1.4 ± 0.5	0.26 ± 0.1	1	0.18	+60 to +100	24 ± 20	90 ± 90	
		8	−41.7 ± 0.1	69 ± 8	2.0 ± 0.5	0.36 ± 0.1	1	0.18	+80 to +100	<15	−	
W28	1720	1	10.8 ± 0.1	119 ± 10	5.0 ± 0.5	0.9 ± 0.1	1	0.17	<8	<8	−	
		2	9.4 ± 0.1	72 ± 7	5.0 ± 0.5	0.9 ± 0.1	1	0.17	<16	<12	−	
		3	5.2 ± 0.4	17 ± 7	14 ± 5	2.4 ± 0.9	3	0.52	−	−	−	
W43	1612	1	40.4 ± 0.2	83 ± 9	6.5 ± 0.5	1.2 ± 0.1	1	0.19	<7 †	−	−	Probably a double feature
		2	27.4 ± 0.4	30 ± 10	7.7 ± 0.6	1.4 ± 0.1	1	0.19	<70	−	−	
W44	1720	1	44.0 ± 0.3	24 ± 2	9.0 ± 1	1.6 ± 0.2	3	0.52	<30	<24	−	
		2	46.3 ± 0.3	18 ± 2	6.0 ± 1	1.0 ± 0.2	3	0.52	<30	<30	−	
NGC 6334N	1665	1	−12.7 ± 0.1	54 ± 5	2.2 ± 0.5	0.40 ± 0.1	1	0.18	+80 to +100	<20	−	Blended into a single feature
		2	−12.3 ± 0.1	115 ± 10	1.8 ± 0.5	0.33 ± 0.1	1	0.18	+90 to +100	<10	−	
		3	−9.0 ± 0.1	200 ± 20	1.8 ± 0.5	0.32 ± 0.1	1	0.18	−95 to −100	16 ± 5	90 ± 10	
		4	−8.1 ± 0.1	29 ± 4	1.4 ± 0.5	0.25 ± 0.1	1	0.18	−80 to −100	26 ± 15	175 ± 90	
NGC 6334N	1667	1	−12.0 ± 0.1	27 ± 4	3.0 ± 0.5	0.54 ± 0.1	1	0.18	+75 to +100	40 ± 40	60 ± 90	
		2	−10.6 ± 0.1	29 ± 4	2.5 ± 0.5	0.45 ± 0.1	1	0.18	−50 ± 20	<50	−	Blended
		3	−10.1 ± 0.1	59 ± 6	1.7 ± 0.5	0.31 ± 0.1	1	0.18	−73 to −100	18 ± 18	0 ± 90	
NGC 6334S	1665	1	−11.8 ± 0.1	29 ± 4	1.8 ± 0.5	0.32 ± 0.1	1	0.18	+70 to +100	50 ± 30	15 ± 60	
		2	−10.5 ± 0.1	44 ± 4	3.0 ± 0.5	0.55 ± 0.1	1	0.18	0 to +44	60 to 100	100 ± 20	
		3	−9.7 ± 0.1	22 ± 4	3.3 ± 0.5	0.60 ± 0.1	1	0.18	−20 to −100	60 to 100	30 ± 40	The variable features are omitted
		4	−8.1 ± 0.1	49 ± 5	1.7 ± 0.5	0.30 ± 0.1	1	0.18	+49 ± 15	26 ± 15	150 ± 30	
		5	−6.0 ± 0.1	61 ± 5	1.8 ± 0.5	0.32 ± 0.1	1	0.18	−25 to +9	80 to 100	10 ± 10	
		6	−5.6 ± 0.1	34 ± 4	1.7 ± 0.5	0.30 ± 0.1	1	0.18	+62 to +100	64 ± 30	100 ± 60	
NGC 6334S	1667	−	−	−	−	−	−	−	−	−	−	The major features are time varying
W49	1665	1	5.2 ± 0.1	59 ± 6	3.9 ± 0.5	0.70 ± 0.1	1	0.18	−75 ± 25	<17	−	
		2	7.7 ± 0.1	54 ± 5	3.1 ± 0.5	0.55 ± 0.1	1	0.18	+75 ± 28	<19	−	
		3	11.1 ± 0.1	34 ± 5	2.5 ± 0.5	0.45 ± 0.1	1	0.18	−50 ± 44	<39	−	Blended
		4	12.0 ± 0.1	108 ± 11	3.3 ± 0.5	0.60 ± 0.1	1	0.18	−65 ± 14	<10	−	
		5	13.6 ± 0.1	49 ± 5	5.5 ± 0.5	1.00 ± 0.1	1	0.18	0 ± 31	<21	−	
		6	15.0 ± 0.1	44 ± 5	4.3 ± 0.5	0.77 ± 0.1	1	0.18	+32 to +100	<23	−	
		7	15.1 ± 0.1	73 ± 7	1.7 ± 0.5	0.30 ± 0.1	1	0.18	−58 to −100	<14	−	
		8	15.6 ± 0.1	157 ± 16	2.5 ± 0.5	0.45 ± 0.1	1	0.18	−20 ± 10	<7	−	
		9	16.0 ± 0.1	200 ± 20	2.2 ± 0.5	0.40 ± 0.1	1	0.18	+80 ± 8	<6	−	
		10	16.6 ± 0.1	200 ± 20	3.6 ± 0.5	0.65 ± 0.1	1	0.18	−84 to −100	<6	−	
		11	16.8 ± 0.1	186 ± 19	3.0 ± 0.5	0.54 ± 0.1	1	0.18	−84 to −100	<6	−	Blended
		12	17.4 ± 0.1	83 ± 8	1.4 ± 0.5	0.25 ± 0.1	1	0.18	−20 ± 18	<13	−	
		13	17.8 ± 0.1	98 ± 10	4.4 ± 0.5	0.80 ± 0.1	1	0.18	−70 to −100	<11	−	
		14	18.0 ± 0.1	44 ± 5	2.5 ± 0.5	0.45 ± 0.1	1	0.18	+36 to +100	<24	−	
		15	18.5 ± 0.1	64 ± 6	5.5 ± 0.5	1.00 ± 0.1	1	0.18	−54 to −100	<17	−	
		16	20.0 ± 0.1	64 ± 6	1.9 ± 0.5	0.35 ± 0.1	1	0.18	−50 ± 23	<17	−	
		17	20.9 ± 0.1	226 ± 23	2.8 ± 0.5	0.50 ± 0.1	1	0.18	−90 ± 7	<5	−	
W49	1667	1	2.0 ± 0.1	74 ± 7	2.5 ± 0.5	0.45 ± 0.1	1	0.18	+50 ± 16	<14	−	
		2	2.6 ± 0.1	83 ± 8	3.9 ± 0.5	0.70 ± 0.1	1	0.18	−60 ± 14	<12	−	
		3	2.8 ± 0.1	39 ± 5	3.6 ± 0.5	0.65 ± 0.1	1	0.18	+70 to +100	<26	−	
		4	3.3 ± 0.1	24 ± 5	3.1 ± 0.5	0.55 ± 0.1	1	0.18	−52 to −100	<42	−	
		5	3.9 ± 0.1	59 ± 6	9.4 ± 0.5	1.70 ± 0.1	1	0.18	+80 to +100	<17	−	
		6	4.9 ± 0.1	88 ± 9	7.5 ± 0.5	1.35 ± 0.1	1	0.18	−87 to −100	<11	−	
		7	5.6 ± 0.1	44 ± 5	6.8 ± 0.5	1.22 ± 0.1	1	0.18	+80 27	<23	−	
		8	6.2 ± 0.1	24 ± 5	3.1 ± 0.5	1.55 ± 0.1	1	0.18	−52 to −100	<24	−	
		9	7.5 ± 0.1	39 ± 5	11.1 ± 0.5	2.00 ± 0.5	1	0.18	+35 ± 30	<26	−	
		10	19.0 ± 0.1	98 ± 10	3.3 ± 0.5	0.59 ± 0.1	1	0.18	−88 to −100	<10	−	
W49	1720	1	15.22 ± 0.1	48 ± 5	3.9 ± 0.5	0.68 ± 0.1	1	0.17	−84 to −100	−	−	In July 1968
W51	1665	1	56.8 ± 0.1	29 ± 6	1.8 ± 0.5	0.32 ± 0.1	1	0.18	−35 ± 38	<35	−	
		2	57.7 ± 0.1	127 ± 13	1.9 ± 0.5	0.35 ± 0.1	1	0.18	+6 ± 9	<8	−	
		3	58.1 ± 0.1	49 ± 6	2.8 ± 0.5	0.50 ± 0.1	1	0.18	+50 ± 23	<20	−	
		4	59.1 ± 0.1	78 ± 8	4.1 ± 0.5	0.74 ± 0.1	1	0.18	+15 ± 14	<13	−	Blended
		5	59.9 ± 0.1	20 ± 6	3.1 ± 0.5	0.55 ± 0.1	1	0.18	−42 to −100	<50	−	
		6	61.4 ± 0.1	44 ± 6	2.2 ± 0.5	0.40 ± 0.1	1	0.18	−74 to −100	<23		
W75S	1665	1	−0.4 ± 0.1	10 ± 8)	2.5 ± 0.5	0.45 ± 0.1	1	0.18	−57 to −100	<27	−	
		2	+0.5 ± 0.1	48 ± 8	3.3 ± 0.5	0.59 ± 0.1	1	0.18	−78 ± 6	42 ± 7	2 ± 10	
		3	+1.0 ± 0.1	34 ± 8	2.8 ± 0.5	0.50 ± 0.1	1	0.18	−75 to −100	16 ± 12	30 ± 25	Blended
		4	+1.8 ± 0.1	20 ± 8	2.2 ± 0.5	0.40 ± 0.1	1	0.18	+64 to +100	42 ± 25	113 ± 50	
W75N	1665	1	3.0 ± 0.1	24 ± 4	1.4 ± 0.5	0.25 ± 0.1	1	0.18	−82 to −100	−	−	
		2	4.9 ± 0.1	14 ± 4	2.2 ± 0.5	0.40 ± 0.1	1	0.18	−75 ± 20	−	−	
		3	5.3 ± 0.1	15 ± 4	2.1 ± 0.5	0.38 ± 0.1	1	0.18	+60 to +100	−	−	Blended
		4	5.8 ± 0.1	26 ± 4	1.8 ± 0.5	0.32 ± 0.1	1	0.18	+84 to +100	−	−	
		5	9.1 ± 0.1	15 ± 4	2.0 ± 0.5	0.36 ± 0.1	1	0.18	+64 to +100	−	−	
		6	11.8 ± 0.1	42 ± 5	1.9 ± 0.5	0.34 ± 0.1	1	0.18	+93 to +100	<14	−	
		7	12.9 ± 0.1	10 ± 4	2.0 ± 0.5	0.36 ± 0.1	1	0.18	+73 to +100	−	−	

* The feature summary for W3 is taken from Meeks, et al. (1966); for W28 and W44 from Ball and Staelin (1968); and for NGC 6334, W49, and W51 from Ball and Meeks (1968), with occasional corrections.

† But P_c rises to 30 ± 8 percent at 40.7 km/sec and to −31 ± 13 percent at 41.0 km/sec on the side of this feature. This is a complex or multiple feature.

‡ The velocities are measured with respect to the local standard of rest (see Sec. IV-B). The assumed line rest frequencies are those given in Sec. I-A.

§ The widths are the total widths between half power points and are not corrected for instrumental resolution.

¶ The error limits on P_c (percent circular polarization) and P_L (percent linear polarization) represent about 2 standard divisions estimated on the basis of measured receiver noise. These limits apply only to the centers of the features. P_c is positive for right circular polarization and negative for left circular polarization.

♯ This source is time varying; the fluxes here are from the circular data taken in July 1968. See Sec. V-H.

Figure 12 shows a map of the W3 region made by Mezger [Mezger, P. G. (1965) unpublished] at 1415 MHz using the NRAO 300-foot antenna. The beamwidth is about 10 arcminutes. The contours of this map are shown superimposed on the National Geographic-Palomar Sky Survey plate of this region.
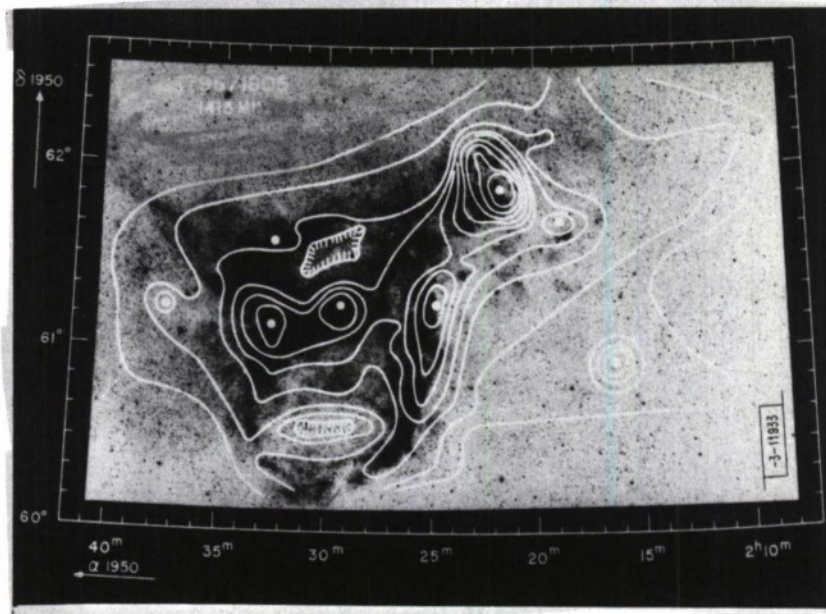

Fig. 12. W3 region mop mode ot 1.415 GHz ond superimposed on the Notionol Geogrophic-Polomor Sky Survey Print of this region. The NRAO 300-foot ontenno wos used by P. G. Mezger (1965, unpublished).

The SNR HB-3 is located at 2^h15^m; 62°30' (1950), i.e., near the upper right edge of Mezger's map, and is about 110 arcminutes in diameter [Poveda and Woltjer (1968)]. An association between HB-3 and W3 has been pointed out by Caswell (1967). Moreover, Mezger's map shows what may possibly be another SNR arc extending from 2^h25^m; 60°40' up around to 2^h18^m; 61°45' (1950). Studies of the spectrum, polarization, and hydrogen recombination lines from this arc would establish whether it is an SNR or not. However, if this arc turns out to be an SNR, it shares with the SNR W28 (see Sec. V-B) the property of having an OH emission source along its outer edge and the property of having a small-diameter continuum source at its center. On Mezger's map this center source is at $2^h16.^m2$; 60°55" (1950). W41 is also an SNR with a center source and associated OH emission [Kesteven (1968a and b), Goss (1968)].

Figure 13 shows the 1665-MHz OH emission Stokes parameters of W3 measured at Haystack in 1965 and 1966. This is a re-reduction of some of the data of Meeks, et al. (1966) combined with some more recent circular polarization data as indicated in Table VI. An error in the Meeks, et al. spectra, namely reversed labeling of S_1 and S_2, has been corrected. A summary of the features seen on these spectra is given in Table VIII. The properties of the W3 region are summarized in Table IX.

Figure 14 shows the results of a re-measurement of the same Stokes parameters in 1967 and 1969. This re-measurement was partly in response to the suggestion by Coles, et al. (1968) that the polarization properties of two of the features in the OH emission spectrum of W3 had changed in time without any corresponding change in flux. Coles, et al. found substantial linear
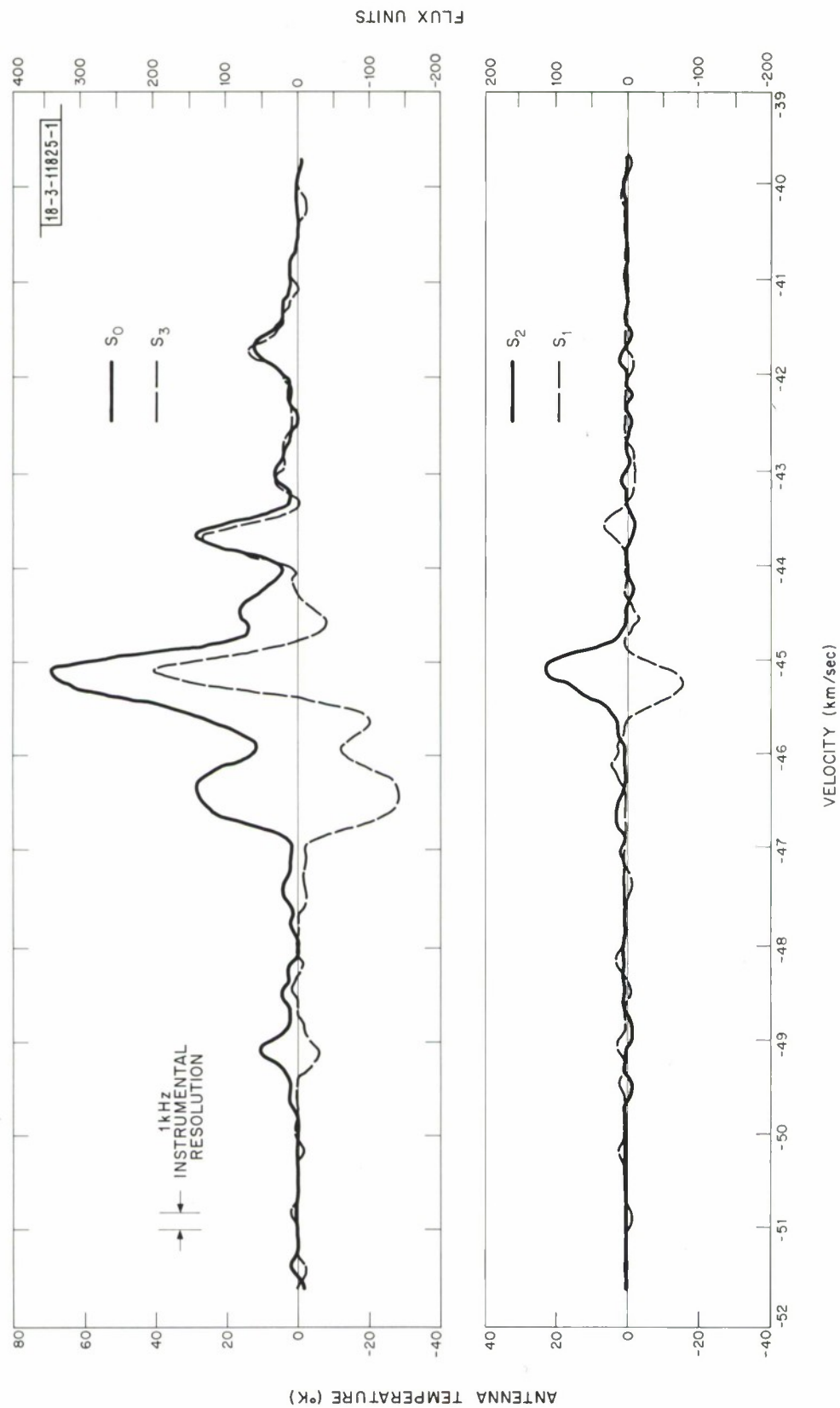
Fig. 13.   W3 spectrum at 1665 MHz; 1965 and 1966 data.
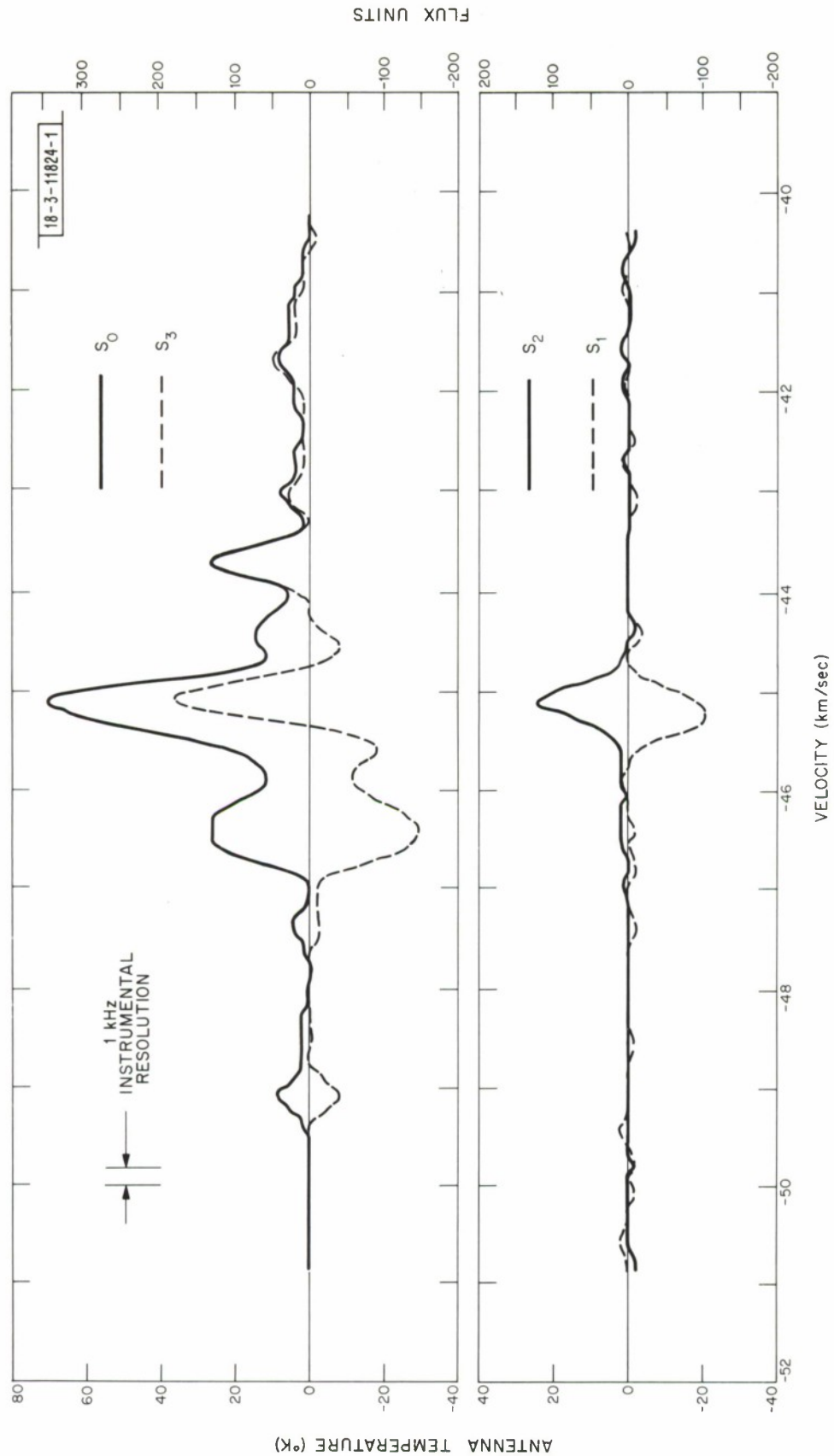
Fig. 14. W3 spectrum at 1665 MHz; 1967 and 1969 data.

TABLE IX							
W3 REGION – SUMMARY OF PROPERTIES							
Distance		Excited Hydrogen Line Observations		21-cm Hydrogen Line Observations		OH Observations *	
		v_r (km/sec)	Notes	v_r (km/sec)	Notes	v_r (km/sec)	Notes
kpc	Notes						
2.6	Mezger ond Höglund (1967)	−43.5 −50.4	Mezger and Höglund (1967)	−48 to −37	Absorption Rogers (1967)	−50 to −38	Emission Meeks, et ol. (1966)
3.19	Dieter (1967)	−41.4	Dieter (1967)				Weaver, et al. (1968), etc.
3.1	Reifenstein (1968)	−42.3	Reifenstein (1968)			−41 to −36	Absorption Weover, et ol. (1968)
* The OH emission is displaced from the continuum sources to which most of these meosurements opply.							

polarization in the feature at −46.4 km/sec, whereas neither Fig. 13 or 14 shows any linear polarization in this feature to an upper limit of 13 percent (see also Table VIII).

Coles, et al. also found no linear polarization in the feature at −43.7 km/sec. A comparison of Figs. 13 and 14 shows that this feature does indeed seem to show significantly less linear polarization on the later date and a small frequency shift as well. These data are probably compatible with the assumption that a weak but strongly linearly polarized feature, which was blended on the high velocity side of the −43.7 km/sec feature, has decreased or disappeared. Otherwise, the spectra of OH emission from W3 appear unchanged.

Some salient features of these spectra are worth noting. The features are highly polarized — some are likely to be nearly 100 percent. Furthermore, the complex features near the center may be made up of several Gaussian features, each 100 percent polarized, which add incoherently in the region of overlap [Meeks, et al. (1966)]. The percent linear polarization, the percent circular polarization, the total percent polarization, and the linear polarization position angle all vary as a function of velocity across the central region of the spectra.

The kinetic temperatures implied by the feature widths are 15° to 700°K, but the brightness temperatures implied by the measured fluxes and angular sizes are perhaps 10^{12}°K [Moran, et al. (1968)]. Each of these numbers must be viewed with caution, however. The calculated kinetic temperatures may be too small if maser amplification has narrowed the feature widths or too large if microturbulence or some other line broadening mechanism has an appreciable effect. The non-Gaussian shape of some of the features probably means that some influence other than kinetic broadening is effective. And the calculated brightness temperatures may be too small if interstellar scintillation has broadened the apparent feature sizes or if absorption has appreciably reduced the flux, or too large if refraction or reflection effects occur in a masering medium.

The pointing position used for the spectra and listed in Table VI is from Rogers, et al. (1967). Raimond and Eliasson (1968) give a slightly more accurate position, namely $2^h 23^m 16.^s8 \pm 0.2s$; $61°38'54'' \pm 1''$ (1950).
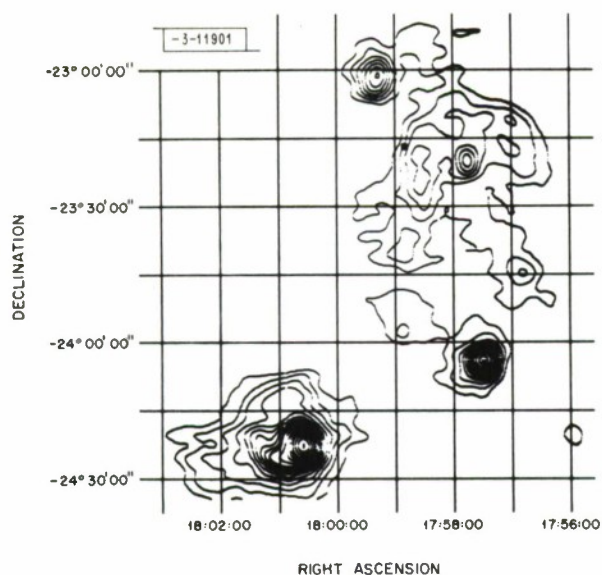
Fig. 15.   W28–W29 regian map at 7.795 GHz at Haystack.
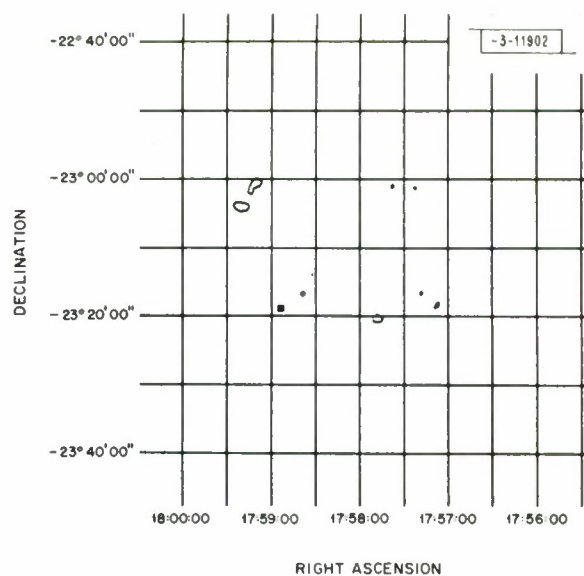
Fig. 16.   W28 region map at 15.5 GHz at Haystack.
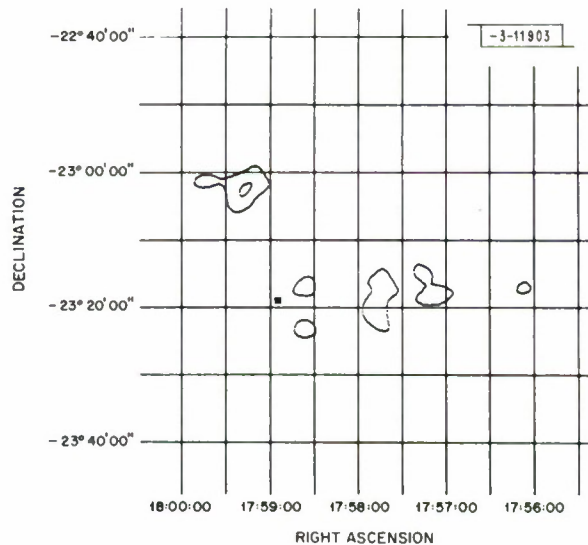
Fig. 17.   W28 regian map at 15.5 GHz at Haystack.   Map cantains same data as in Fig. 16; however, data have been smoothed to a 0°.072 equivalent beam-width (see Table V and Sec. IV-A-1).

40

The early detection at 8 GHz of the weak continuum source coincident with the W3 OH emission position (W3γ in Table VII) suggested that lower frequency continuum measurements would be desirable. Initially, it was not known whether W3γ was a thermal or nonthermal source, or whether it might be a representative of a new class of source. Also, it was not known whether the OH emission and continuum positions were truly coincident or only approximately so. A series of measurements was undertaken with the Haystack-Millstone interferometer to measure the continuum emission from W3 at about 18 cm.

The initial measurements were made with a 4-MHz window approximately centered on the 1665-MHz emission from W3. Rogers (1967b) shows that the vector average of the fringe amplitude and phase across the window (for an add-subtract-autocorrelation interferometer) contains no contribution from any narrow line emission but only a contribution due to the continuum. This mode of observation is ideal because the emission line phase may be used as a reference with which to compare the average (continuum) fringe amplitude and phase.

The first series of observations, which were made in this mode, gave a clear indication of a continuum source with essentially no phase offset from the phase of the OH emission line. Subsequently, other measurements were made with a 4-MHz and a 1.2-MHz spectral window that was offset to exclude the OH emission line. These measurements gave, by contrast, no indication of any continuum emission near the OH position in W3. For a continuum source that is small in angular size compared with the fringe spacing and coincident in position with the OH emission source, these measurements imply an upper limit of 0.4 flux unit. This upper limit is compatible with an extrapolation of the flux determinations of this source by Mezger, et al. (1967) and Aikman (1968). There is some indication in the interferometer data of a rapidly changing continuum fringe amplitude and phase which is due to continuum emission well away from the reference position (the OH emission position).

It is likely that some unknown instrumental effect caused the anomalous results that were seen in the initial series of measurements.

B. W28

The M20-W28-W29 (M8) region has been studied in the radio continuum by Rieu (1963), Mezger and Henderson (1967) and Kesteven (1968a and b) among many others. Table VII lists the four prominent continuum peaks in this region, but Fig. 15 also shows several subsidiary peaks and a ridge of continuum emission extending along the Galactic plane. In Table VII the W28 entry refers to the SNR which appears in Fig. 15 as a semicircular arc some 20 arcminutes in diameter. In the center of this arc is a small diameter source listed as W28C in Table VII. The marginal detection of W28C at 15 GHz shown in Figs. 16 and 17 makes it likely but not certain that W28C has a thermal spectrum. Low frequency maps have so far failed to separate W28 and W28C because of lower resolution and probably also because of the relative spectra. M20 on the north and W29 on the south are known to be H II regions. The source G5.9 − 0.4 was, unfortunately, not covered by the 15-GHz map; however, it probably corresponds to source A_2 of Rieu (1963), who measured 58 fu at 1430 MHz. If this identification is correct, then G5.9 − 0.4 is a thermal source.

Table X, which summarizes the properties of these four sources, contains a number of gaps and questionable entries. If the distance determinations are all correct, then we conclude that M20 is separated in distance from W28 and W29 which are at about the same distance. But the

| | | | TABLE X | | | | | |
| | | | W28-M20-W29 (M8) — SUMMARY OF PROPERTIES [*] | | | | | |

| | | | Excited Hydrogen Line Observations | | 21-cm Hydrogen Line Observations | | OH Observations | |
| | Distance | | v_r (km/sec) | Notes | v_r (km/sec) | Notes | v_r (km/sec) | Notes |
Region	kpc	Notes						
M20 [†]	4.15	Dieter (1967)	17.9	Dieter (1967)	–	–	–	–
	4.2	Goss (1968)	16.4	Reifenstein (1968)				
	3.8	Reifenstein (1968)						
	1.5	Miller (1968)						
W28 [‡]	3.3	Aizu and Tabara (1967)	14.2	Reifenstein	7.5	Absorption, Menan and Williams in Goss (1968)	6 to 7.5	Absorption at 1612, 1665, 1667 MHz, Goss (1968).
	2	Goss (1968)					3 to 17	Emission at 1720 MHz, Goss (1968), Ball and Staelin (1968), Coles et al. (1968), Goss and Robinson (1968)
	1.3	Povedo and Waltjer (1968)						
	3.6	Reifenstein (1968)						
G5.9 − 0.4 [§]	3.0	Reifenstein (1968)	10.5	Reifenstein (1968)	–	–	−35 to +30	1612-MHz emission at −20.5 km/sec,
								1665 MHz emission at −20 to 30 km/sec,
								1667 MHz emission at −35 to 27 km/sec,
								1720 MHz possible absorption at 9 km/sec. (Coles, et al. (1968), Turner (1969))
W29 [¶]	1.2	Clark (1965)	3.5	Mezger and Höglund (1967)	6.3	Absorption, Clark (1965)	10.6	Weak absorption, Goss (1968)
	1.4	Goss (1968)			0			
	1.1	Mezger and Höglund (1967)	4.6	Lilley, et al. (1966)				
	1.0	Reifenstein (1968)	−4	McGee and Gardner (1968)				
	1.4	Miller (1968)	3.0	Reifenstein (1968)				

[*] Refer to Table VII for additional information about the corresponding continuum sources.

[†] These measurements probably belong here, notwithstanding that Dieter (1967) gives her pointing position close to W28.

[‡] CTB46, an SNR but there is thermal emission in this region also; see text.

[§] The 1612-MHz OH emission position coincides within 2 arcminutes with the continuum peak.

[¶] M8, NGC 6523, AMWW37, CTB46, the Lagoon Nebula, an H II region. Optical velocities: −7.1 km/sec, Courtes (1960), or −3 km/sec, Campbell and Moore in Wilson (1953).

picture is not at all clear, because, for example, the 4.2 kpc distance of Dieter (1967) and Goss (1968) may refer to the ridge of continuum radiation near W28 rather than M20. Also the 1720-MHz OH emission, presumably associated with W28, extends almost up to the velocity found by Dieter (1967) for M20. And in W29 the various hydrogen recombination line velocities listed in Table X suggest a complex or multiple source. The 1612-MHz OH emission velocity (about -20.5 km/sec) for G5.9 $-$ 0.4 is not near any of the other velocities listed and corresponds to a kinematic location on the far side of the galaxy. However, the 1665- and 1667-MHz emission extends over the range -35 to $+30$ km/sec. The center of this velocity range is probably a more reasonable estimate for the velocity of the OH source [see Turner (1969)].
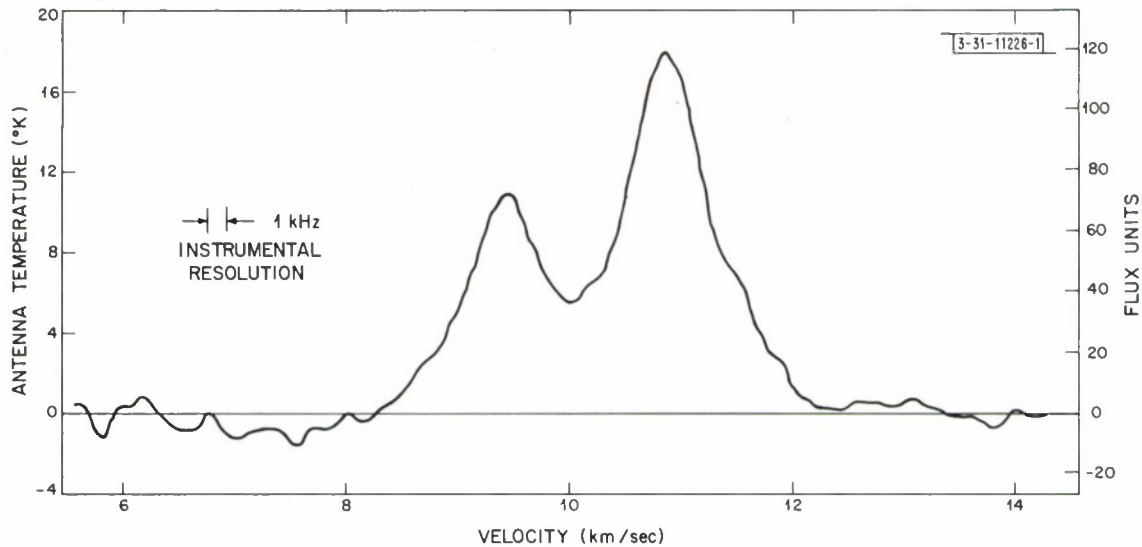
Fig. 18. W28 spectrum at 1720 MHz (S_o).

Figure 18 shows the 1720-MHz emission measured with the Millstone antenna. The linear and circular polarization properties of this OH emission were also observed and upper limits are listed in Table VIII. Using the Haystack antenna, the position of the two strongest 1720-MHz OH emission features from W28 was measured to be $17^h58^m52^s\pm5^s$; $-23°18'\pm1'$ (1950) and this position has been confirmed by Goss and Robinson (1968) who also measured the circular and linear polarization parameters with a better signal to noise ratio than ours and who confirm the low percentage of polarization.

The 1720-MHz OH observations of W28 were made in collaboration with Professor D. H. Staelin of M.I.T. [Ball and Staelin (1968)].

C. W43

The continuum emission around W43 is the most complex studied for this report. Although only two sources in the W43 region are listed in Table VII, a complex extended region with several subsidiary peaks is revealed in the maps of Figs. 19 and 20. Also the emission continues on northward from where the mapping stopped and perhaps on southward also.

The continuum emission from this region has been studied by numerous other workers including Mezger and Henderson (1967), Kesteven (1968a), and MacLeod and Doherty (1968). The H I radiation in this direction has been studied by Clark (1965) and others, and the hydrogen
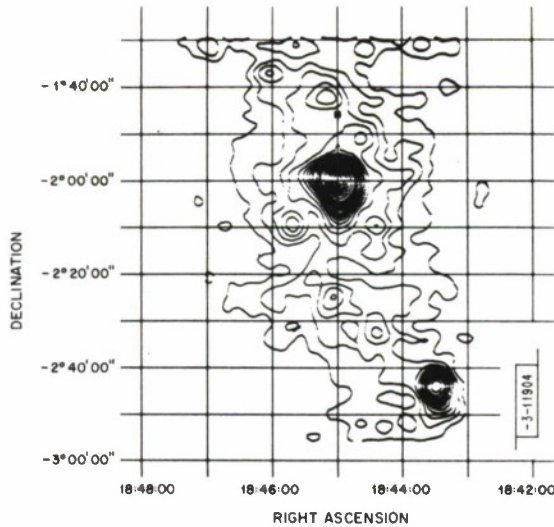
Fig. 19. W43 region map at 7.795 GHz at Haystack.   Fig. 20. W43 region map at 15.5 GHz at Haystack.
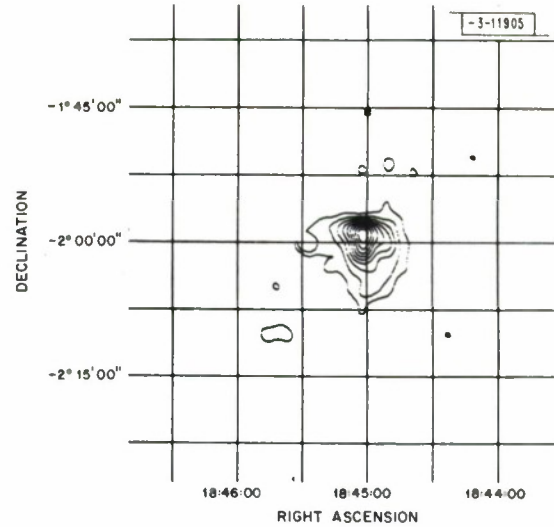
recombination line radiation from this region has been studied by Mezger and Höglund (1967), Dieter (1967), Goss (1968), and McGee and Gardner (1968).   And the OH emission and absorption in this region have been studied by Goss (1968) and Coles, et al. (1968).   Figure 21 shows the 1612-MHz OH emission observed for this report.

In the direction of W43 we are probably seeing at least three regions separated in distance but approximately coincident on the sky.   Table XI summarizes the properties of these regions. The recent observations of Coles, et al. (1968) have elucidated the nature of the OH source in region II by showing that the 1665- and 1667-MHz OH spectrum is made up of narrow polarized emission lines masked by strong absorption at about the same velocity.

The continuum radiation from W43 is not known to have a nonthermal component and there are no known nonthermal sources nearby.   The region around the south source (G30.0 − 0.0) has not been well studied.   The W43 region clearly deserves much more work.

On 11 July 1968, using the Millstone antenna, the 40.5 km/sec OH emission feature at 1612 MHz in W43 was mapped to determine its position and angular size.   These data show that this emission is coming from $18^h45^m.0\pm0^m.5$; $-1°45'.5\pm6'$ (1950).   This position is about 15 arc-minutes north of the continuum maximum and does not agree with the position given by Turner (1969) for the same feature.   Turner's position for this OH feature is essentially coincident with the continuum maximum.   Although the Millstone antenna occasionally gives trouble with pointing, no errors as large as 15 arcminutes have been noted on other occasions.   Only additional obser-vations will resolve this discrepancy.

D.   W44

The W44 (3C392) region has been studied in the radio continuum by Scheuer (1963), Hollinger and Hobbs (1966), Kesteven (1968a and b) and Milne [in Goss and Robinson (1968)] among many others.   The neutral hydrogen absorption from this region has been studied by Menon and Williams [in Goss (1968)] and the OH emission by Goss (1968), Ball and Staelin (1968), Goss and Robinson (1968), and Coles, et al. (1968).   Excited hydrogen line emission from this region was not detected by Dieter (1967), but was found by Reifenstein (1968) in the nearby source W44W.
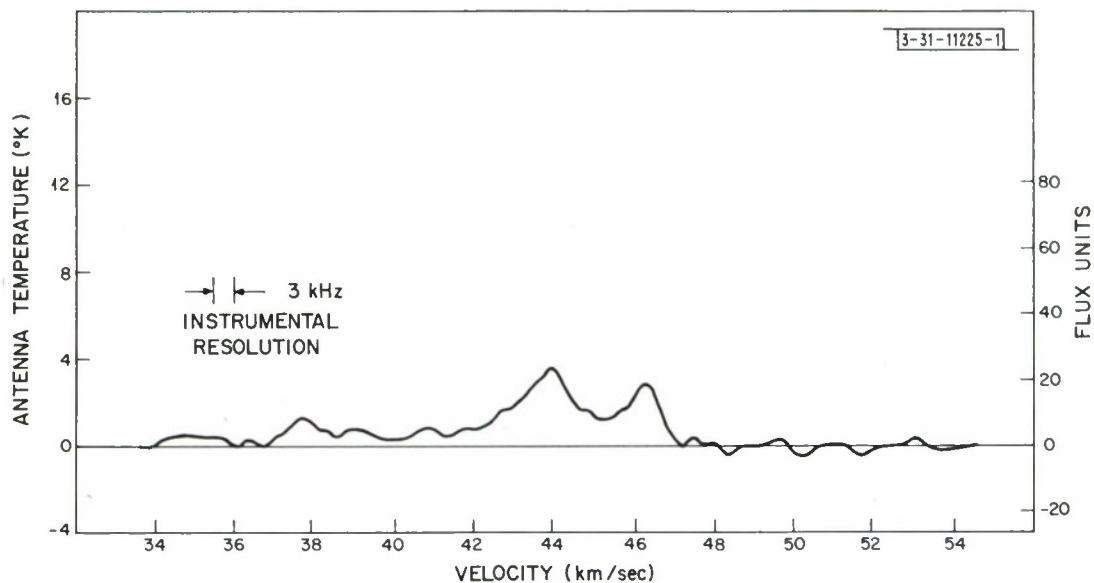
44
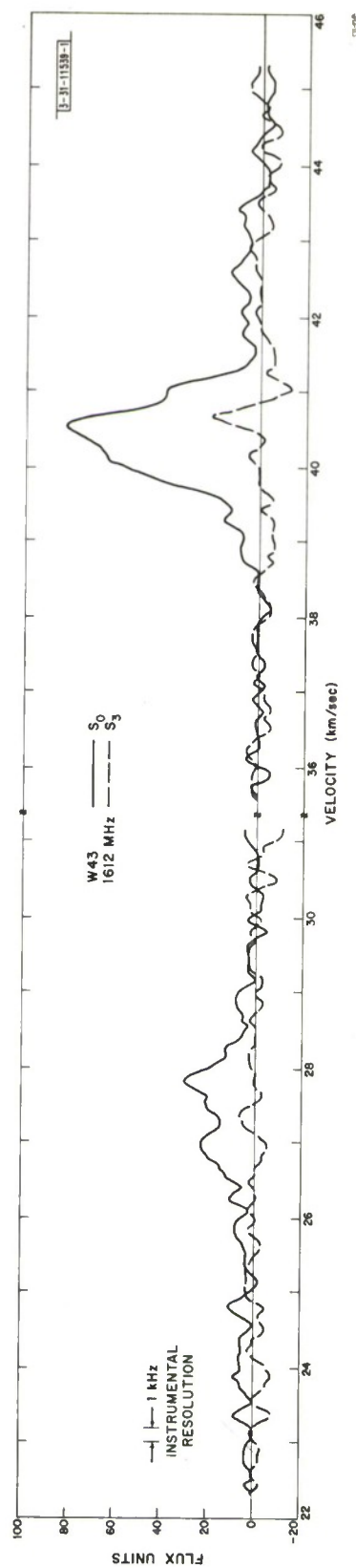
Fig. 21. W43 spectrum at 1612 MHz.

45

TABLE XI

W43 REGION – SUMMARY OF PROPERTIES

Region	Distance		Excited Hydrogen Line Observations		21-cm Hydrogen Line Observations		OH Observations	
	kpc	Notes	v_r (km/sec)	Notes	v_r (km/sec)	Notes	v_r (km/sec)	Notes
I *	0.6 to 1.0	Goss (1968)	—	—	12.9	Absorption, Menon and Williams in Goss (1968)	5 to 15	Emission at 1720; only absorption at the other transitions, Goss (1968)
					12	Absorption, Kerr in Mezger and Höglund (1967)		
II †	6.5	Mezger and Höglund (1967)	88.6	Mezger and Höglund (1967)	64 to 94	Absorption, Kerr in Mezger and Höglund (1967)	65 to 105	Emission, probably strongest at 1667 MHz, and strong absorption, Goss (1968), Coles, et al. (1968)
	7.5	Goss (1968)	97	Goss (1968)	61	Absorption, Menon and Williams in Goss (1968)		
	7.52	Dieter (1967)	97	Dieter (1967)	81			
	7.0	Reifenstein (1968)	89	McGee and Gardner (1968)	91			
			92.3	Reifenstein (1968)				
III ‡	14	Goss (1968)	44	Goss (1968)	40	Emission, Kerr in Mezger and Höglund (1967), and in Goss (1968)	25 to 45	1612-MHz emission strongest with a low degree of polarization. 1665 and 1667 MHz emission also but no absorption. Polarization unknown, Goss (1968), Coles, et al. (1968)
	13.99	Dieter (1967)	44.2	Dieter (1967)				

* This may be a type II_a OH source. The angular position is unknown. The lack of excited hydrogen radiation at this velocity may correspond to an NTS or to a weak or absent thermal continuum source.

† This region probably contains a Type I OH source, but the very broad 1720-MHz emission does not fit the pattern very well. Goss and Robinson (1968) find the 1720-MHz emission feature at 90 km/sec at $18^h44^m49^s \pm 8^s$, $-2°04' \pm 2$ (1950); i.e., slightly southwest of the continuum maximum.

‡ Goss (1968) finds the 1667-MHz emission feature at 37 km/sec at $18^h45^m \pm 40^s$, $-2°10' \pm 10'$ (1950), i.e., slightly south of the continuum maximum.

Figure 22 shows a 7.795-GHz map and Fig. 23 a 15.5-GHz map of this region. The central extended source, W44 proper, is an SNR and shows the arc structure typical of most such sources. However, the small diameter source designated W44W in Table VII has a thermal spectrum and the ridge of continuum emission connecting the two may also be thermal.
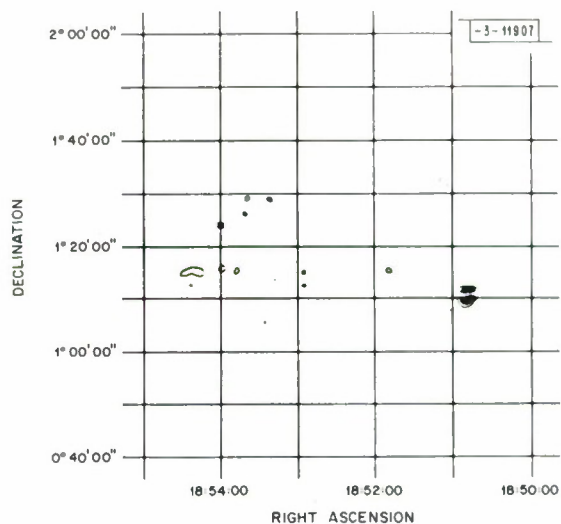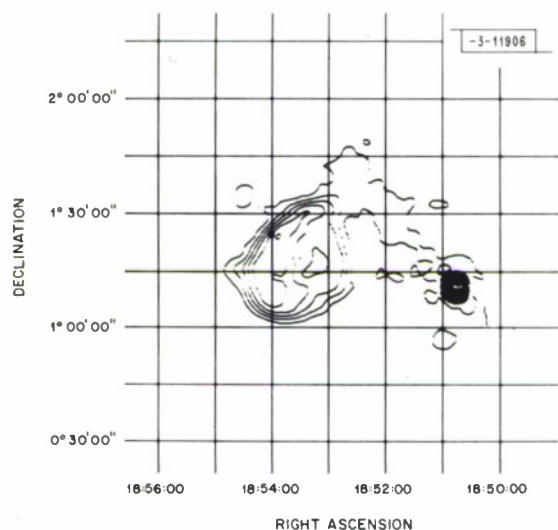
Fig. 22. W44 region map at 7.795 GHz at Haystack. Fig. 23. W44 region map at 15.5 GHz at Haystack.

Table XII summarizes the properties of W44 and divides it into two regions separated by 20 or 30 km/sec in radial velocity and probably also separated in angle as indicated in the notes in Table XII.

The 1720-MHz OH emission from W44 is shown in Fig. 24 and upper limits for the polarization of these features are listed in Table VIII. The spectrum in Fig. 24 is not identical with the spectrum of Goss and Robinson (1968) who list a feature at 43.4 km/sec which does not agree

Fig. 24. W44 spectrum at 1720 MHz (S_o).

TABLE XII

W44 REGION — SUMMARY OF PROPERTIES

Region	Distance		Excited Hydrogen Line Observations		21-cm Hydrogen Line Observations		OH Observations	
	kpc	Notes	v_r (km/sec)	Notes	v_r (km/sec)	Notes	v_r (km/sec)	Notes
I *	3.4	Aizu and Tabara (1967)			30	Absorption, Menon and Williams in Goss (1968)	35 to 50	Emission at 1720 MHz, absorption at other transitions, Goss (1968), Ball and Staelin (1968), Goss and Robinson (1968), Coles, et al. (1968)
	3	Goss (1968)			42			
	1.6	Poveda and Woltjer (1968)						
	1	Goss (1968)						
II †					12	Absorption, Menon and Williams in Goss (1968)	10 to 15	Emission at 1612 MHz, absorption at other transitions, Goss (1968), Goss and Robinson (1968)
W44W ‡	3.8	Reifenstein (1968)	53.9	Reifenstein (1968)				

* Goss and Robinson (1968) find a 1720-MHz OH emission feature at 43.4 km/sec at $18^h53^m53^s$, $1°23.9$ (1950). The distance problem is discussed in the text.

† Goss and Robinson (1968) failed to find the 1612-MHz OH emission feature at 13.5 km/sec at either of the 1720-MHz emission positions above; it is therefore probably displaced in angle as well as distance.

‡ It is not clear whether there is a physical association between W44 and W44W.

with the 44.0 km/sec feature in Fig. 24; however, the 46.3 km/sec feature agrees well. Both the antenna beamwidths and the pointing positions are different, so the most likely explanation of the discrepancy involves the existence of two or more features overlapping in velocity but separated in position. Another possibility involves the existence of a feature extended in angle. Such a feature would appear relatively more pronounced in the Millstone spectrum as compared with the spectrum made with the Parkes 210-foot antenna. The recent observations of Turner (1969) confirm the existence of spatially separated features.

The distances for W44 listed in Table XII do not agree. The distance determination of Poveda and Woltjer (1968) is based on their empirical relation between the radio surface brightness and the linear diameter of an SNR. There will, of course, be some scatter in this relation. The kinematic distance may also be in error because of peculiar motions. The OH absorbing cloud is certainly in front of the SNR, so a hypothetical spatial separation between them does not reconcile the discrepancy. For subsequent calculations, Goss' distance is used, but definitive conclusions about this region must await further work. An excited hydrogen line measurement would be particularly helpful.

E. NGC 6334

NGC 6334, a complex H II region at a declination of about $-36°$, is difficult to observe from the latitude of Massachusetts. However, it has proved to be an interesting source, both in the continuum and in OH emission, and well worth the extra effort necessary to make accurate measurements. Radio continuum observations of this region have been made by Haddock, et al. (1954), Wilson and Bolton (1960), Wilson (1963) (CTB39), Kesteven (1968a), and others. Excited hydrogen lines from this region have been observed by Dieter (1967), McGee and Gardner (1968), and Reifenstein (1968). The OH emission from this region has been observed with a single antenna by Weaver, et al. (1965), Rogers (1967a), Gardner, et al. (1967), McGee and Gardner (1967), Weaver, et al. (1968), and Ball and Meeks (1968), and with an OH interferometer by Rogers, et al. (1967), and Raimond and Eliasson (1969).

This region is not too heavily obscured at optical wavelengths and optical photographs have been shown by Rogers, et al. (1967), Gardner, et al. (1967), Weaver, et al. (1968) and others.

A continuum map made at Haystack at 7.795 GHz is shown in Fig. 25 and an enlarged portion of this map is shown in Fig. 26. A 15-GHz map made at Haystack is shown in Fig. 27. The main ridge of continuum emission was divided into three principle sources on the basis of the 15-GHz map (Fig. 27). These, together with three other continuum sources from Fig. 25, are listed in Table VII. The Howard and Maran (1965) catalog entries for this source (number 497) are confusing but seem to indicate that the source designated NGC 6334ξ is the component seen at low frequencies and is therefore possibly nonthermal. However, Reifenstein (1968) found an excited hydrogen line from this source at a velocity very different from the velocity of NGC 6334 (see Table XIII) and this velocity implies that NGC 6334ξ is much farther away. No prominent optical object can be seen at the position of NGC 6334ξ on a photograph taken with the ADH Baker-Schmidt telescope in South Africa. It seems unlikely that NGC 6334ξ is associated with NGC 6334 itself.

The OH emission in NGC 6334 comes from two small-diameter regions separated by about 15.5 arcminutes. The northern region emits most strongly at 1665 MHz and the southern region most strongly at 1667 MHz. In Table VI and in the Berkeley papers these regions are referred to as NGC 6334N and NGC 6334S, but in Ball and Meeks (1968) they are referred to as NGC 6334I
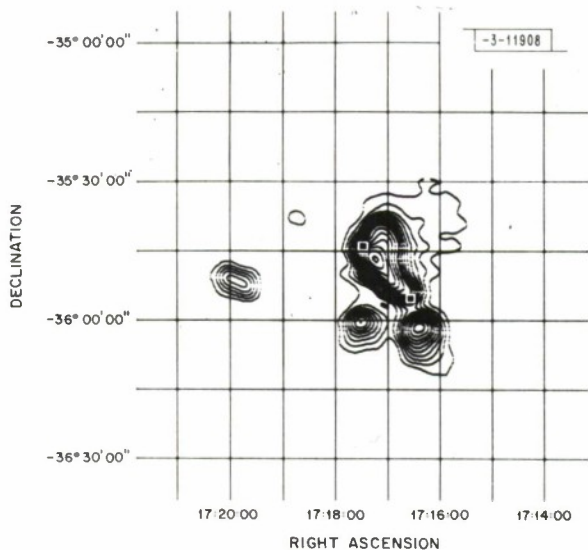
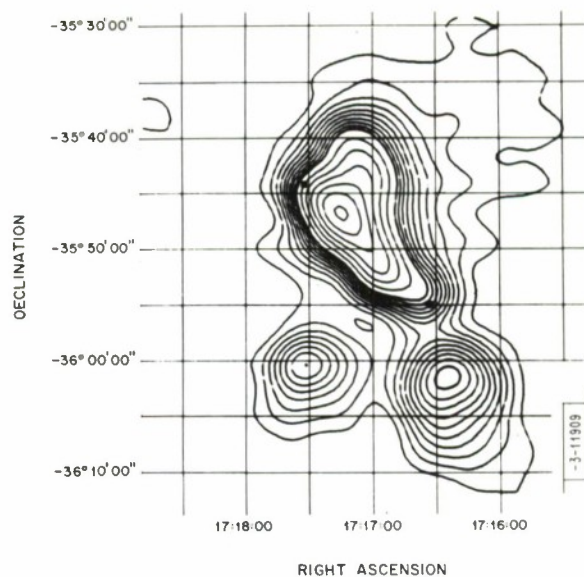Fig. 25. NGC 6334 region map at 7.795 GHz ot Haystack.

Fig. 26. NGC 6334 regian map ot 7.795 GHz at Haystack (enlorged portion af Fig. 25).
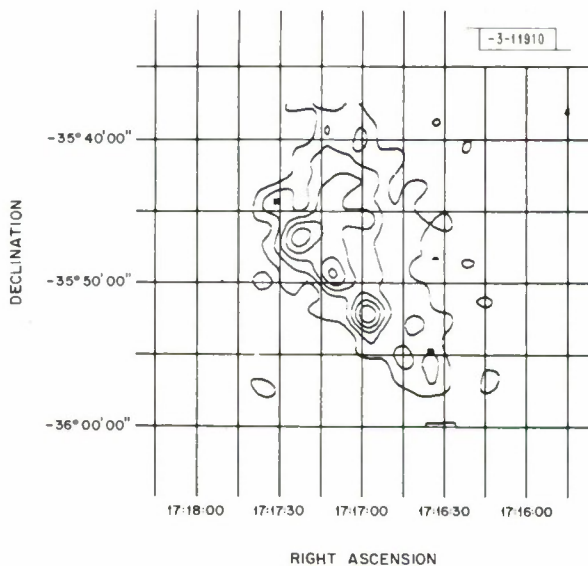

Fig. 27. NGC 6334 region map at 15.5 GHz at Haystack.

TABLE XIII

NGC 6334 REGION – SUMMARY OF PROPERTIES

Region	Distance		Excited Hydrogen Line Observations		21-cm Hydrogen Line Observations		OH Observations	
	kpc	Notes	v_r (km/sec)	Notes	v_r (km/sec)	Notes	v_r (km/sec)	Notes
CTB39 *	1.14	Dieter (1967)	-5.1	Dieter (1967)	4.2	Absorption, Clark, et al. (1962)	–14 to –3	Emission at 1665, 1667, 1720, and possibly 1612 MHz, Rogers (1965), Ball and Meeks (1968), Weaver, et al. (1968).
	0.7	Reifenstein (1968)	–4	McGee and Gardner (1968)	–5.7			
			–2.5	Reifenstein (1968)				
G351.5 + 0.2 †	6.2	Reifenstein (1968)	–42.5	Reifenstein (1968)	–	–	–7 to 0 5 to 7	Absorption, Weaver, et al. (1968)
							–	–

* The distance estimates are very uncertain.

† NGC 6334ξ (see Table VII).

51
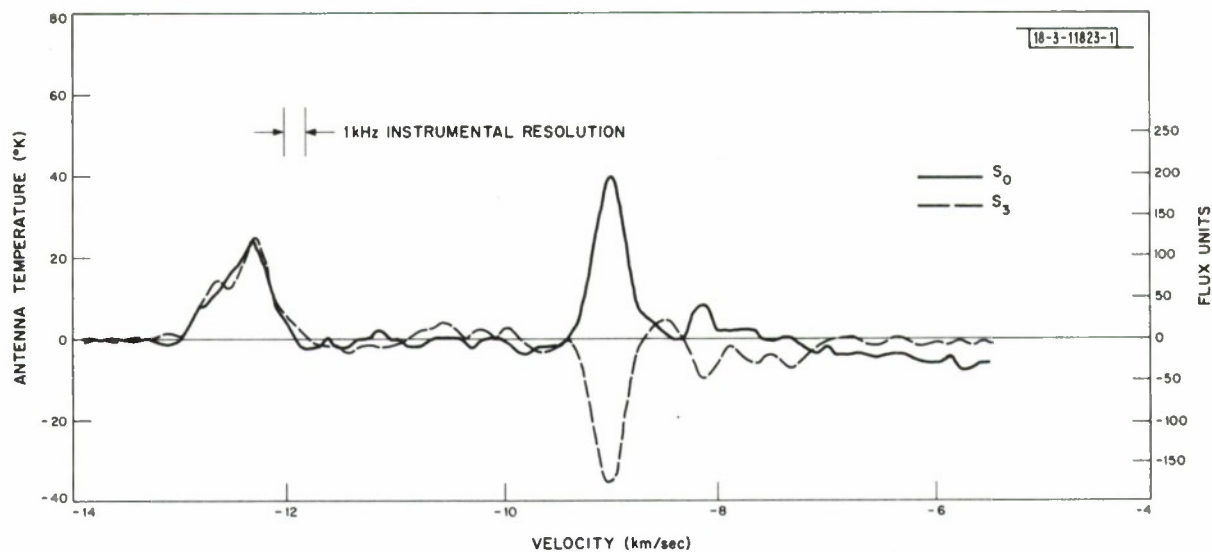
Fig. 28. NGC 6334N restored spectrum ot 1665 MHz; Haystack dota of September ond October 1966.

18-3-11822
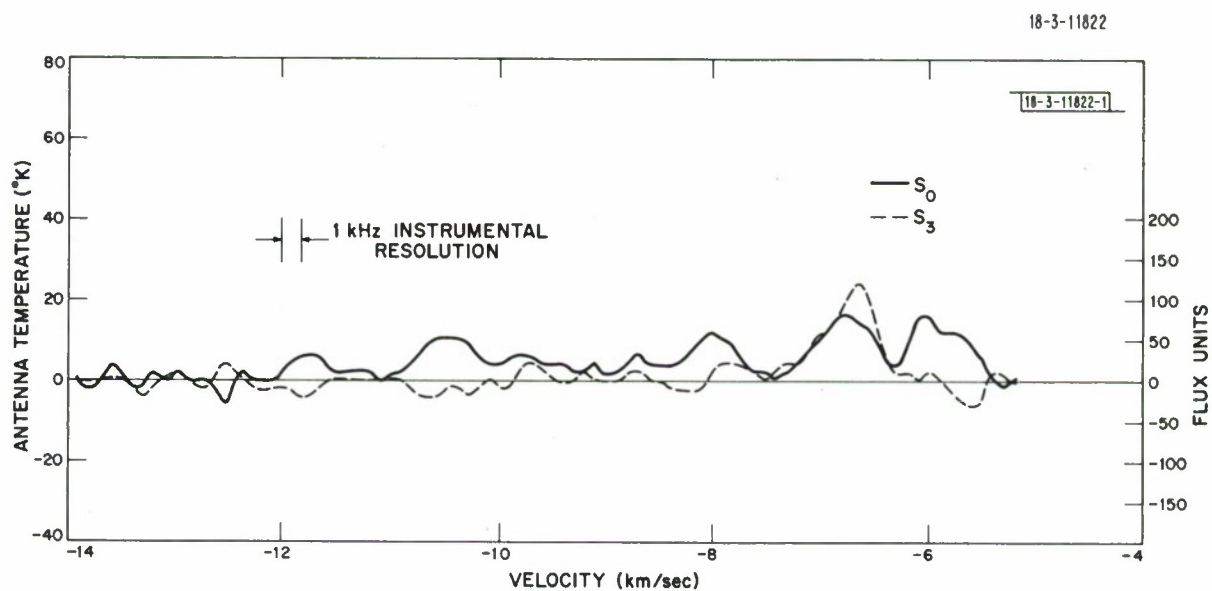
Fig. 29. NGC 6334S restored spectrum ot 1665 MHz; Haystock doto of September ond October 1966.

and NGC 6334II, and Gardner, et al. (1967) refer to them as NGC 6334A and NGC 6334B. Apparently it has not occurred to anyone to call them α and β.

Figures 28 through 31 show restored spectra (see Sec. IV-B-4) of NGC 6334 taken with Haystack in 1966. These data have been presented in another form and discussed in some detail by Ball and Meeks (1968). The circular and linear data near -6.6 and -7.8 km/sec at the south position at 1665 MHz are mutually incompatible because a time variation occurred between the dates on which these data were taken.

Figures 32 through 35 show restored spectra of NGC 6334 taken with Haystack in 1968. A comparison of these two sets of figures shows no evidence for time changes in any of the features from the north position, but the -8.9 km/sec feature at 1667 MHz from the south position has decreased over this period. Figure 36 shows more recent data taken at Millstone that also indicate that the -9.8 km/sec feature has increased. The Millstone data were not restored because the accuracy of the pointing of the Millstone antenna was inadequate.

A very considerable amount of additional data was taken at Millstone and Haystack and these data were examined carefully for the presence of any additional time variations. For the most part, the features at both positions are very stable not only in flux but also in polarization. These unchanged features lend confidence in the ability to make accurate and reproducible flux measurements. The time variation situation is summarized below.

Time variations in the OH emission from NGC 6334 have been reported by Dieter, et al. (1966a and b), Weaver, et al. (1968), Ball and Meeks (1968), and Goss, et al. (1968). At Haystack four features have been seen to vary. At 1665 MHz, two features at about -6.6 and -7.9 km/sec showed a dramatic increase in flux on one and probably two occasions. The time scale for the increase was 9 days or less on one occasion. Within a month or so, the features were back to "normal." At 1667 MHz, two features at about -8.9 and -9.8 km/sec varied on a longer time scale, the former decreasing and the latter increasing slowly over a period of months. All four of these variable features are from NGC 6334S; none of the features from NGC 6334N have been seen to vary at Haystack.

An important question is whether the polarization properties vary in time as suggested by Goss, et al. (1968) or whether the variation may be interpreted as a change in the flux of a feature whose polarization properties remain constant in time as suggested by Ball and Meeks (1968). The spectra show that the variable features are blended with other features which remain constant. Since these nearby constant features have different polarization properties from the variable features, the polarization of the resulting blend will change in time even if the variable feature itself maintains constant polarization. This question will be answered with certainty only with more complete data preferably made with higher frequency resolution.

The original Haystack-Millstone interferometer measurements of Rogers, et al. (1967) located NGC 6334N at $17^{h}17^{m}33\overset{s}{.}5\pm2^{s}$; $-35°45'35"\pm10"$ (1950). More recently Raimond and Eliasson (1969) determined this position to be $17^{h}17^{m}32\overset{s}{.}1\pm0\overset{s}{.}4$; $-35°44'15"\pm10"$ (1950). To resolve this disagreement and to verify the position given by Raimond and Eliasson for NGC 6334S $[17^{h}16^{m}36\overset{s}{.}3\pm0\overset{s}{.}4$; $35°54'57"\pm4"$ (1950)], the Haystack-Millstone interferometer was used to observe these sources at 1665 MHz on 3, 4, and 5 January 1968. A 120-kHz spectral window was used with 3-kHz resolution and both antennas were set for vertical linear polarization. The reference position for NGC 6334N was the Rogers, et al. position above, and the reference position for NGC 6334S was the Raimond and Eliasson position above. The fringe phase for the two strongest features from NGC 6334N and the strongest feature from NGC 6334S is plotted in Fig. 37.
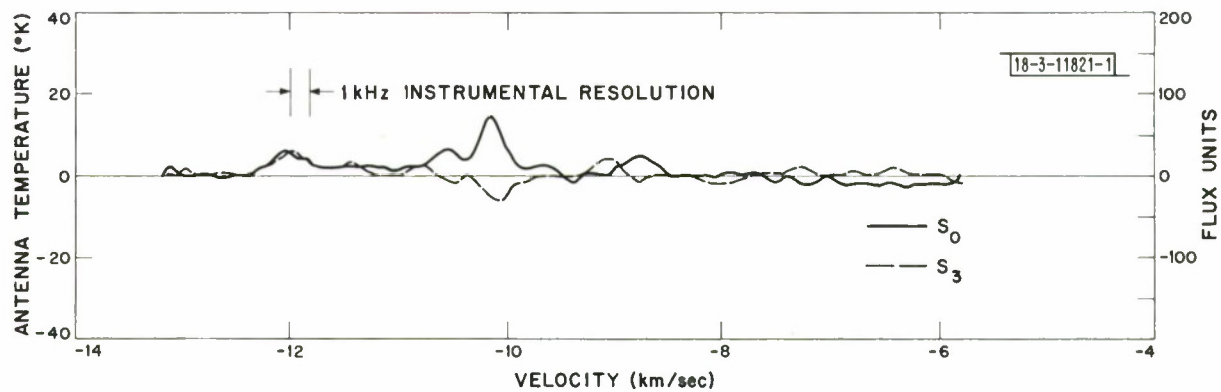
Fig. 30.   NGC 6334N restored spectrum ot 1667 MHz; Hoystock doto of September ond October 1966.
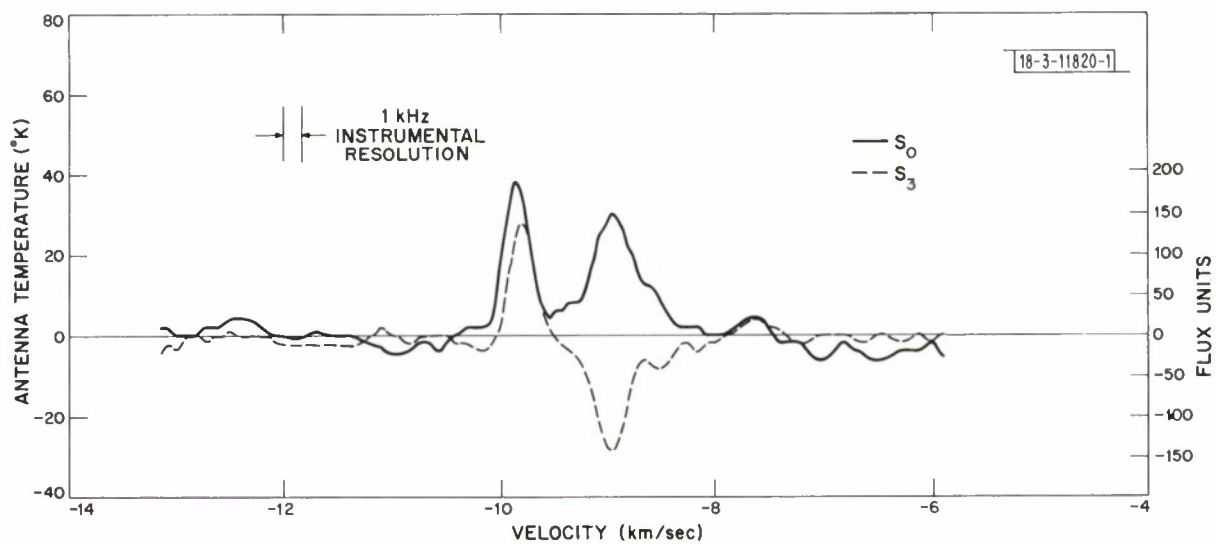

Fig. 31.   NGC 6334S restored spectrum ot 1667 MHz; Hoystock doto of September ond October 1966.
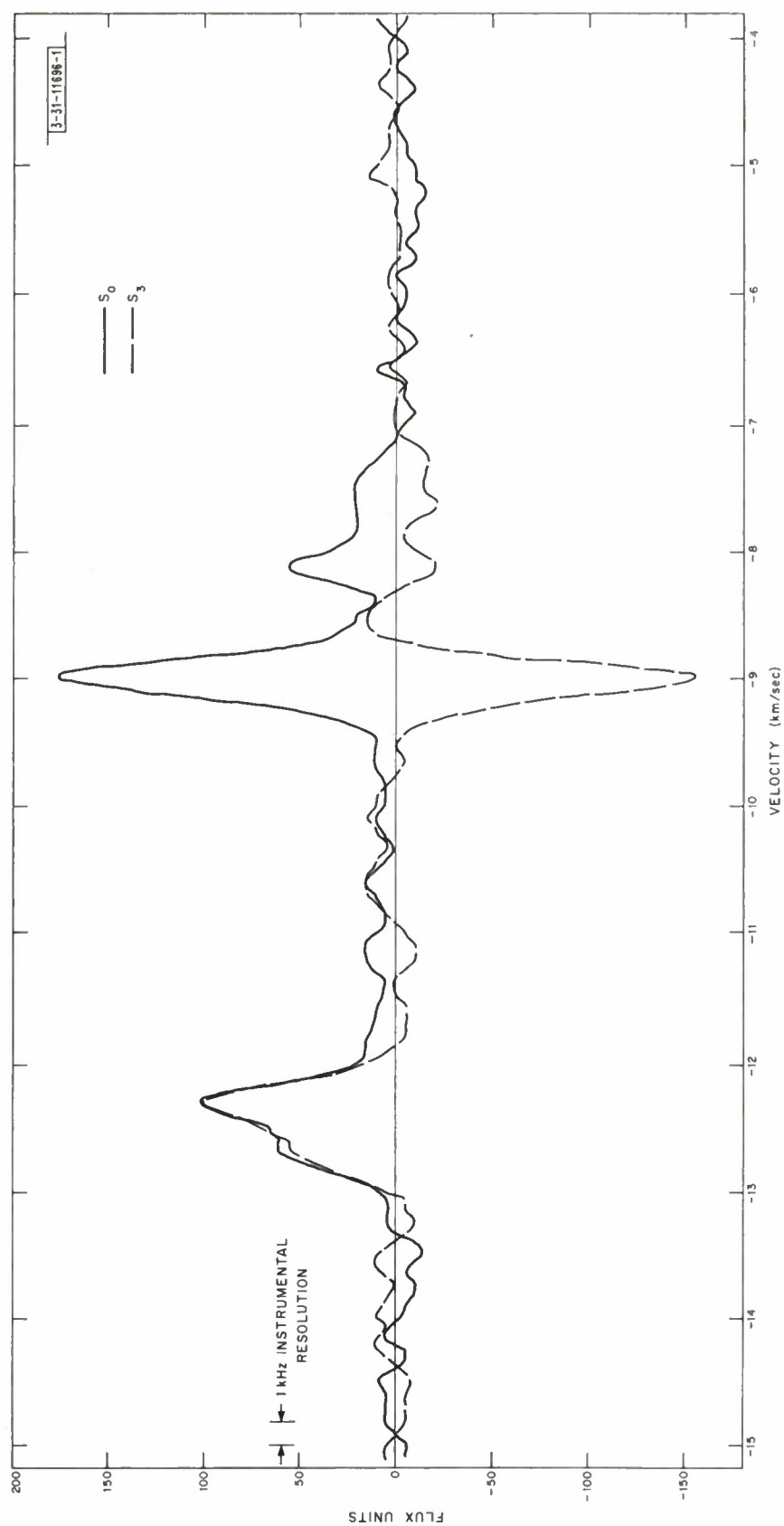
Fig. 32. NGC 6334N restored spectrum at 1665 MHz; Haystack data of May 1968.
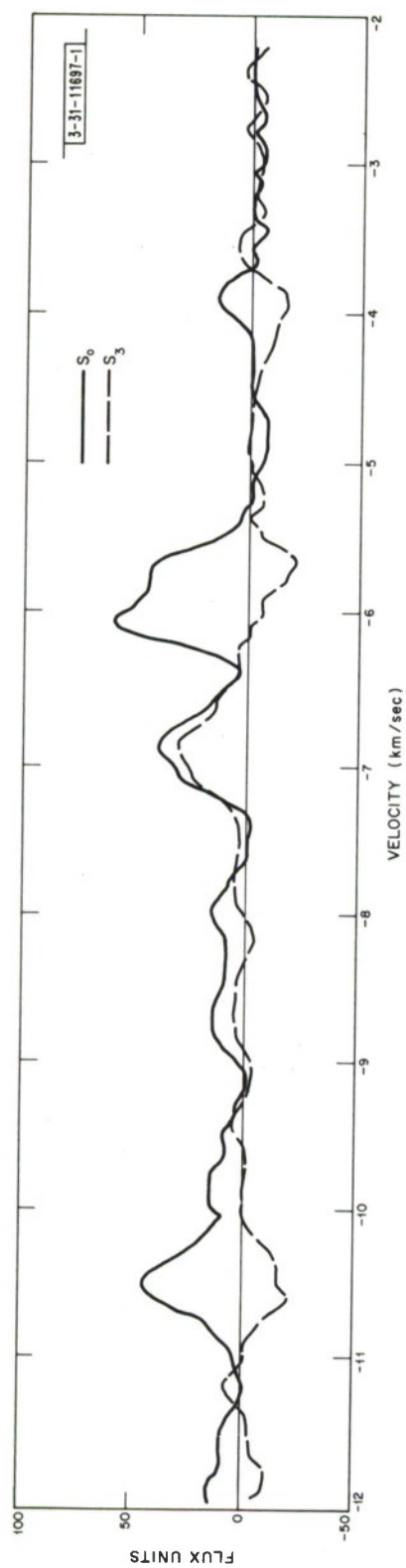
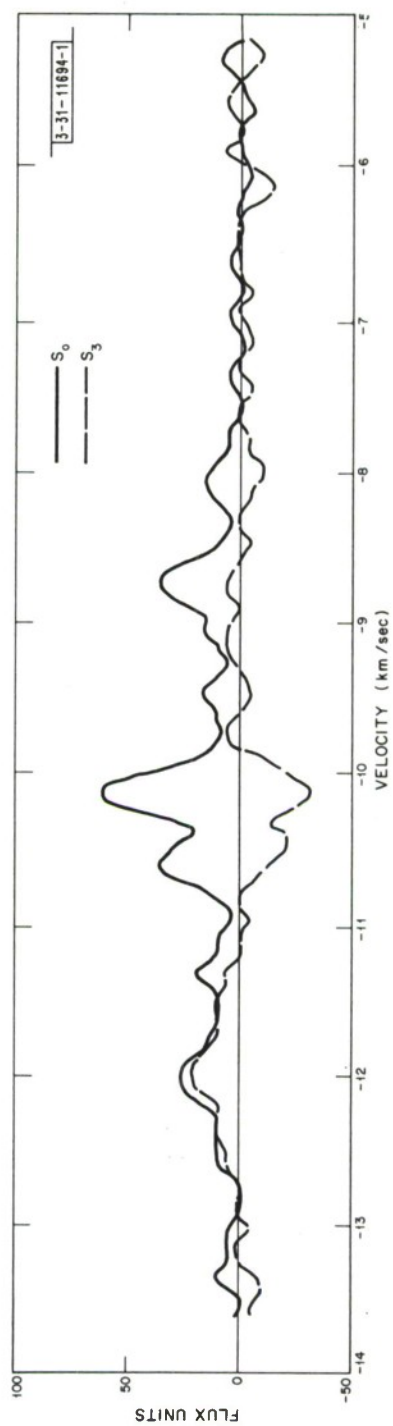Fig. 33. NGC 6334S restored spectrum at 1665 MHz; Haystack data of May 1968.

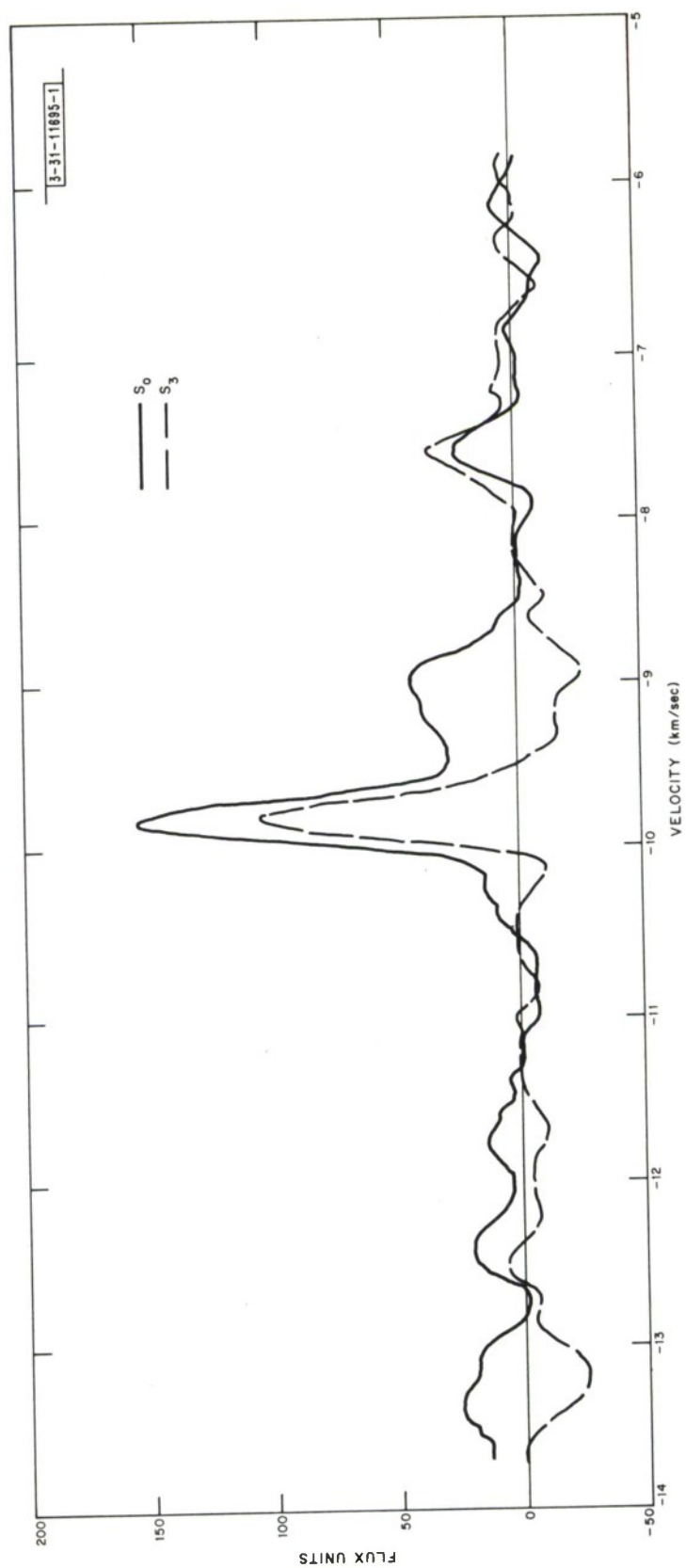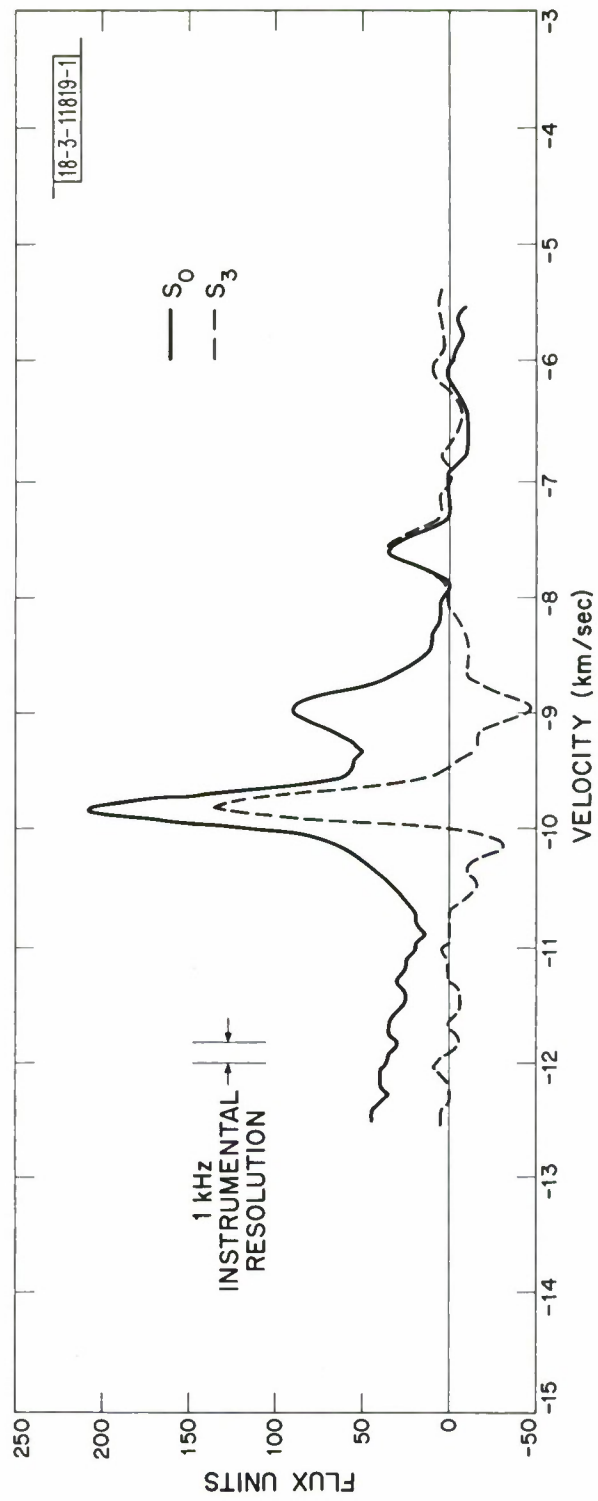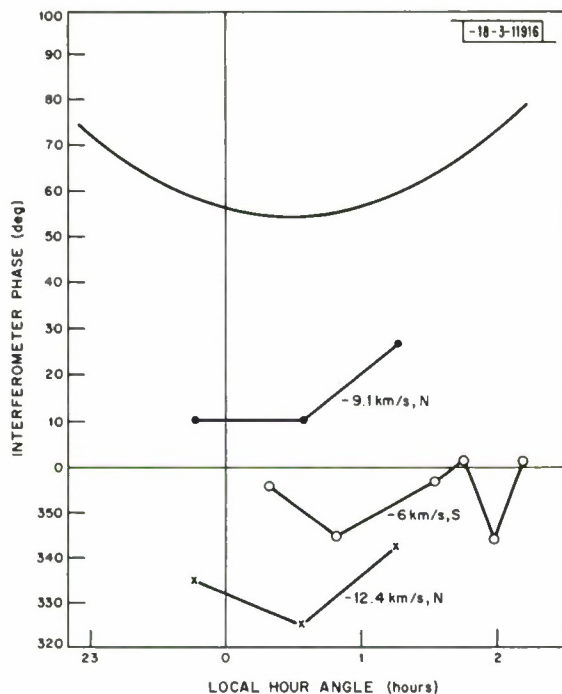Fig. 34. NGC 6334N restored spectrum at 1667 MHz; Haystack data of May 1968.

Fig. 35. NGC 6334S restored spectrum at 1667 MHz; Haystack data of May 1968.

57

Fig. 36. NGC 6334S unrestored spectrum at 1667 MHz; Millstone data of January 1968.

58

Fig. 37. NGC 6334, 1665-MHz Haystack-Millstone interferometer data.

The offset in fringe phase between the two features from the north position is probably an instrumental effect related to their opposite circular polarizations. For example, a 20° offset between the polarization position angles of the two linear feeds could cause this effect; however, the actual error in setting the feeds to be vertical was almost certainly much smaller than 20°.

Figure 37 also includes a line representing the calculated fringe phase for a feature coming from the position given by Raimond and Eliasson for the north source. This line illustrates that it is very difficult to measure declination offsets for southern declination sources with the Haystack-Millstone interferometer or with any two-element fixed baseline interferometer with an approximately north-south baseline. The measurements of Raimond and Eliasson made with a variable interferometer do not suffer from this problem. The present measurements do not allow a distinction between these two positions.

In conclusion, it is likely that this discrepancy results from an underestimation of the declination errors for NGC 6334 (and W24 also) by Rogers, et al. and the positions given by Raimond and Eliasson are probably correct.

F. W49

The source W49, a combination of a very large H II region and a supernova remnant, has been studied in the radio continuum by Mezger and Henderson (1967), Mezger, et al. (1967) and others. The excited hydrogen emission from this region has been studied by Mezger and Höglund (1967), Dieter (1967), McGee and Gardner (1967), and Reifenstein (1968). Since its discovery, referred to in Sec. I-B, this OH emission from W49 has been studied with a single antenna by many workers including Palmer and Zuckerman (1967), Weaver, et al. (1968), and Ball and Meeks (1968), and with an OH interferometer by Rogers, et al. (1966), Cudaback, et al. (1966), Davies, et al. (1967), Moran, et al. (1968), and by Raimond and Eliasson (1969). The $^2\pi_{1/2}$, $J = 1/2$ line of excited OH was detected from this source by Zuckerman, et al. (1968). The region is heavily obscured in the optical, and photographs have failed to reveal this source.

TABLE XIV

W49 REGION – SUMMARY OF PROPERTIES

Distance		Excited Hydrogen Line Observations		21-cm Hydrogen Line Observations		OH Observations	
kpc	Notes	v_r (km/sec)	Notes	v_r (km/sec)	Notes	v_r (km/sec)	Notes
14.1	Mezger and Höglund (1967)	17	Gudnov and Sorochenka (1966)	12	Emission, McGee, et al. (1966)	−2 to 23	Emission, Palmer and Zuckerman (1968), Weaver, et al. (1968), Ball and Meeks (1968)
14.16	Dieter (1967)	7.4	Mezger and Höglund (1967)				
13.8	Reifenstein (1968)	5.2	Dieter (1967)				
		7	McGee and Gardner (1967)				
		8.6	Reifenstein (1968)				

OH emission at all four transitions

A thorough discussion of most of the known properties of W49 has been given by Mezger, et al. (1967), and so these properties will only be summarized here (see Table XIV). Component A of W49 has a complex thermal spectrum which Mezger, et al. (1967) have analyzed into two components, a large low-density H II region (A1) and a small high-density H II region (A2) almost coincident in position. One of the two OH emission positions coincides with A2 and the other lies within A1 along what may be a ridge extending outward from A2. Figure 38 shows a 7.795-GHz map and Fig. 39 a 15-GHz map made at Haystack. The OH emission positions are
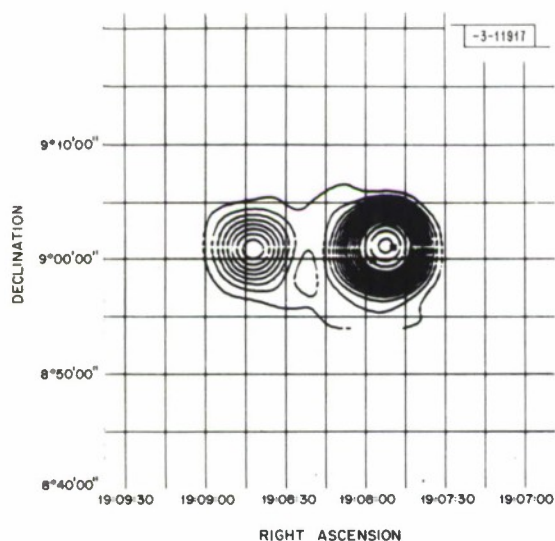
Fig. 38. W49 region at 8 GHz at Haystack.   Fig. 39. W49 region at 15.25 GHz at Haystack.
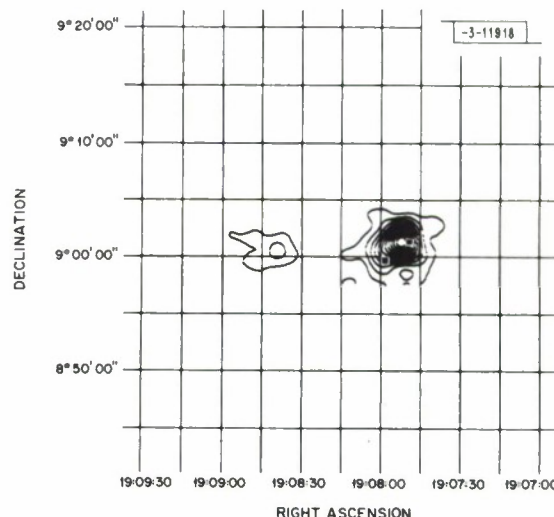
indicated in Fig. 39 by squares. Figure 40 shows the 1665-MHz, Fig. 41 the 1667-MHz, and Fig. 42 the 1720-MHz radiation from W49 as measured at Haystack and Millstone. The OH emission from W49 is notable for containing almost no linear polarization. The flux of the 1720-MHz OH emission feature in Fig. 29 is time varying as pointed out by Zuckerman, et al. (1969). The excited hydrogen velocity for W49 (+5 to +7 km/sec) agrees within about 10 km/sec with the centroid of the OH emission.

The other continuum source, W49B, is a supernova remnant at about the same distance as W49A (14 kpc) as pointed out by Mezger, et al. (1967). This SNR is apparently too far from the OH emission position for any causal relationship.

G. W51

The W51 region has been studied in the radio continuum by Mezger and Henderson (1967) and McLeod and Doherty (1968) and others, and in excited hydrogen by Lilley, et al. (1966), Mezger and Höglund (1967), Dieter (1968), and McGee and Gardner (1968). The OH emission from this region has been studied with a single antenna by Weaver, et al. (1968), Ball and Meeks (1968), and others, and with an OH interferometer by Raimond and Eliasson (1969). A summary of W51 properties is given in Table XV.

Figure 43 shows an 8-GHz and Fig. 44 a 15-GHz map of this region made at Haystack. However, the region over which appreciable emission exists is much larger as shown in the maps of
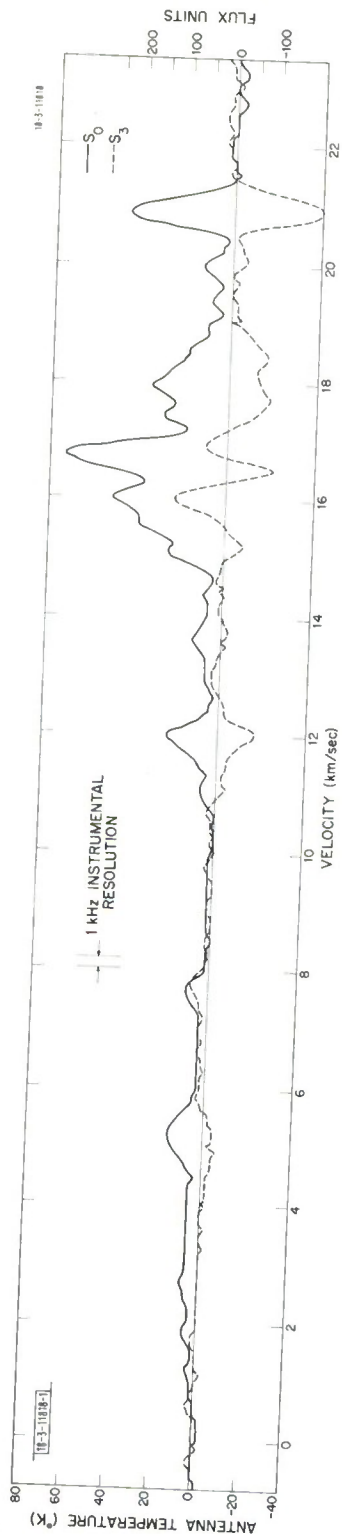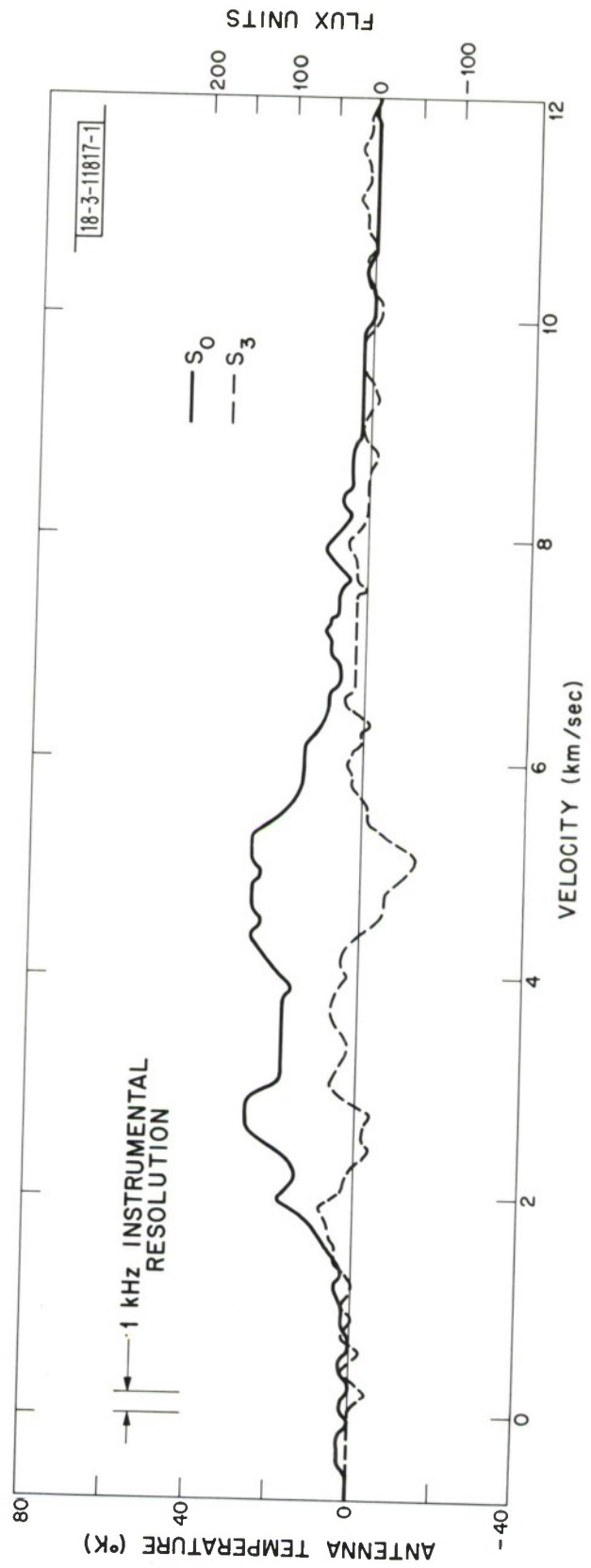
Fig. 40. W49 spectrum at 1665 MHz (S_a and S_3).

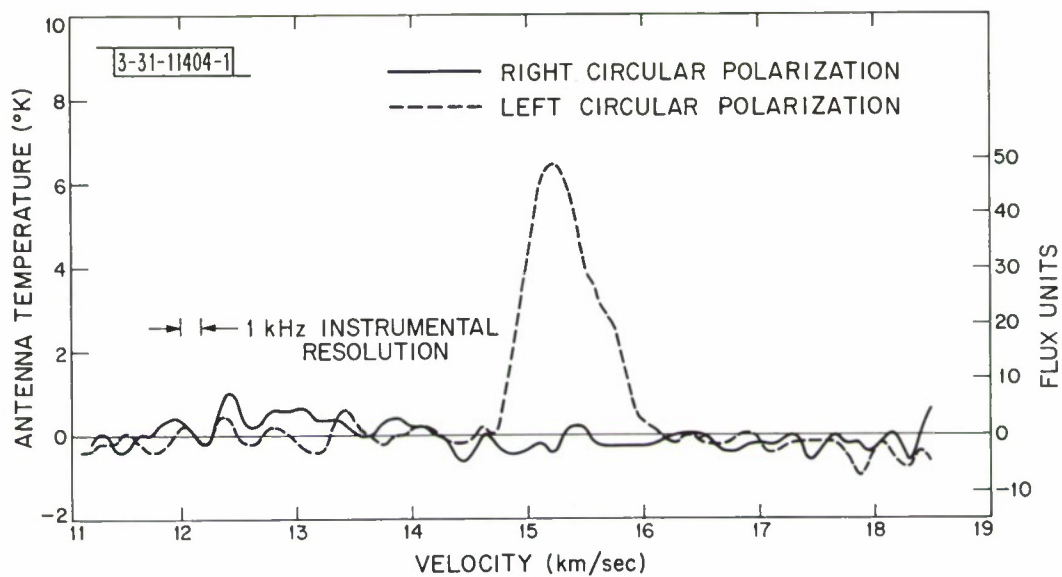Fig. 41. W49 spectrum at 1667 MHz (S_a and S_3).

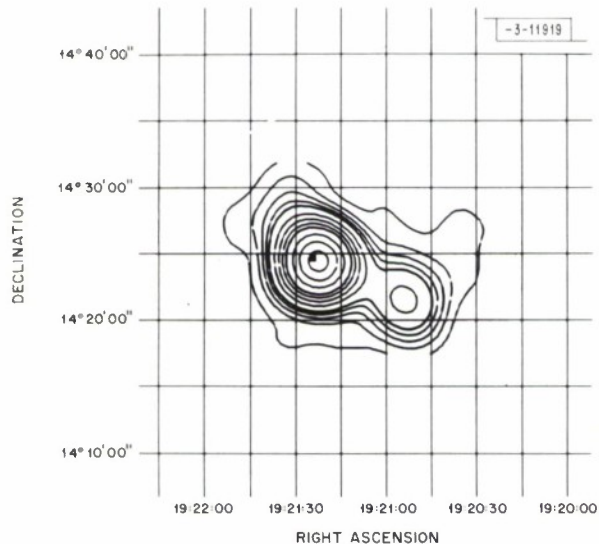Fig. 42. W49 spectrum at 1720 MHz.

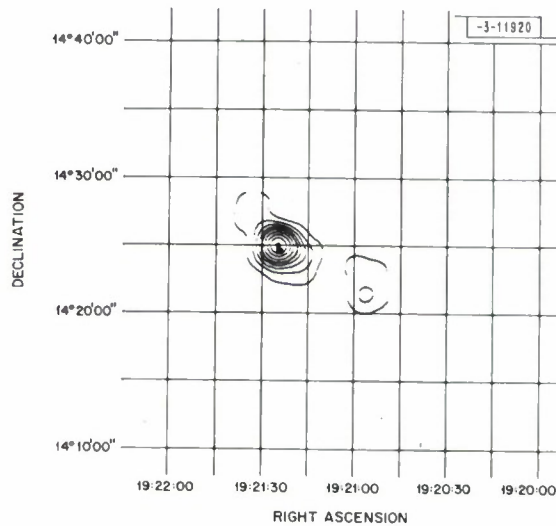Fig. 43. W51 region at 8 GHz at Haystack.

Fig. 44. W51 region at 15.25 GHz at Haystack.

TABLE XV

W51 REGION – SUMMARY OF PROPERTIES

Region	Distance		Excited Hydrogen Line Observations		21-cm Hydrogen Line Observations		OH Observations	
	kpc	Notes	v_r (km/sec)	Notes	v_r (km/sec)	Notes	v_r (km/sec)	Notes
I *	6.5	Mezger and Höglund (1967)	53	Gudnov and Sorachenko (1966)	47.5 54.9	Absorption, Clark (1965)	50 to 70	Emission, Weaver, et al. (1968), Ball and Meeks (1968)
	6.28 5.04	Dieter (1967)	57.6	Lilley, et al. (1967)				
	6.0	Reifenstein (1968)	66.4 59.1	Mezger and Höglund (1967)				
			62.0 57.6	Dieter (1967)				
			55	McGee and Gardner (1968)				
			58.2	Reifenstein (1968)				
			—	—				
II †	0.43	Goss (1968)	—		7.2 12.7	Absorption, Clark (1965)	0 to 10	Goss (1968)
					12	Emission, McGee, et al. (1966)		

* OH emission at 1612, 1665, and 1720 MHz; only absorption at 1667 MHz. See text.

† OH emission at 1720 MHz and OH absorption.

Mezger and Henderson (1967) and McLeod and Doherty (1968). The OH emission position determined by Raimond and Eliasson (1969) is shown by a square on Fig. 44. Figure 45 shows the 1665-MHz emission from W51. This emission is notable for containing two nearly unpolarized features as noted in Table VIII. W51 also shows OH emission at 1612 and 1720 MHz to be about half as strong as the 1665-MHz emission.

The two continuum sources shown in Figs. 43 and 44 are thermal and it is clear that W51 is a large and complex H II region. What is not clear is whether it also contains an SNR as suggested by Mezger and Henderson (1967) and others. The spectrum does turn up at low frequencies; however, McLeod and Doherty (1968) suggest that the spectrum of W51 can be understood in terms of several thermal components becoming optically thick at different frequencies. Shaver (1969) interpreted his recent observations at 408 MHz as indicating the presence of a nonthermal loop well south of the region mapped in Figs. 43 and 44. It would be very helpful to have a measurement of linear polarization on that part of the W51 region which is suspected of being nonthermal.

H. W75

The W75 region has been studied in the radio continuum by Pike and Drake (1964), Downes and Rinehardt (1966), Ryle and Downes (1967), and others. The OH emission from W75 has been studied by Palmer and Zuckerman (1967), Ball and Meeks (1968), Weaver, et al. (1968), and Zuckerman, et al. (1969). Raimond and Eliasson (1969) studied the OH emission from this region interferometrically, but only one of the two OH emission sources near W75 was then known. A summary of properties is given in Table XVI.
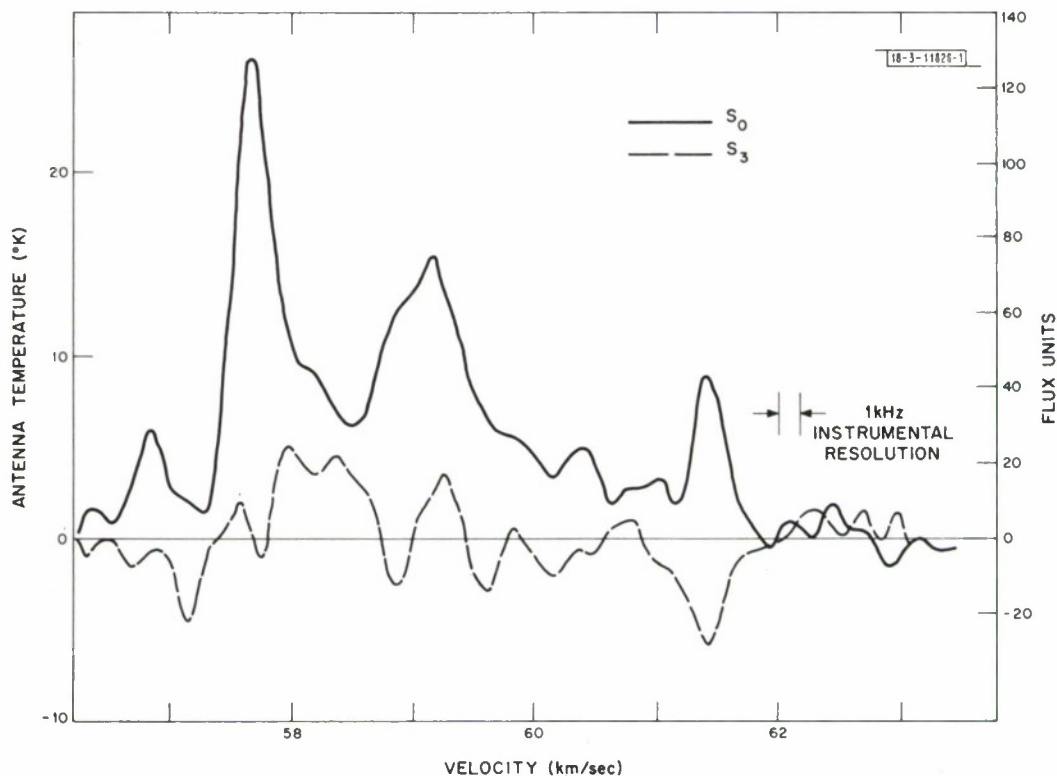

Fig. 45. W51 spectrum at 1665 MHz.

TABLE XVI

W75 REGION – SUMMARY OF PROPERTIES *

Distance		Excited Hydrogen Line Observations		21-cm Hydrogen Line Observations		OH Observations	
kpc	Notes	v_r (km/sec)	Notes	v_r (km/sec)	Notes	v_r (km/sec)	Notes
1.5	Mezger, et al. (1967)	7.8	Dieter (1967)	3.2	Absorption, Clark, et al. (1962)	−2 to +13	Emission, Palmer and Zuckerman (1967); Ball and Meeks (1968), Weaver, et al. (1968), Zuckerman, et al. (1969)
6?	Ryle and Downes (1967)	2.3	Mezger, et al. (1967)	11.4			
1.5	Reifenstein (1968)	1.7	Reifenstein (1968)				

* The velocity is not permitted on a Galactic rotation model and the distance is really unknown.

Figure 46 shows a 7.795-GHz map and Fig. 47 a 15.5-GHz map made at Haystack. Because this source was used as a calibrator (see Secs. II-B and IV-A), neither the flux nor the position of W75-DR21 given in Sec. V can be considered as independent measurements. In Fig. 46 the two OH emission positions are shown by squares. The position of the southern OH emission source (W75S) was taken from Raimond and Eliasson (1969) and the position of the northern source (W75N) was measured at Haystack in May 1968 to be $20^h36^m51^s\pm9^s$; $42°25!5\pm1'$ (1950) [see Zuckerman, et al. (1969)].
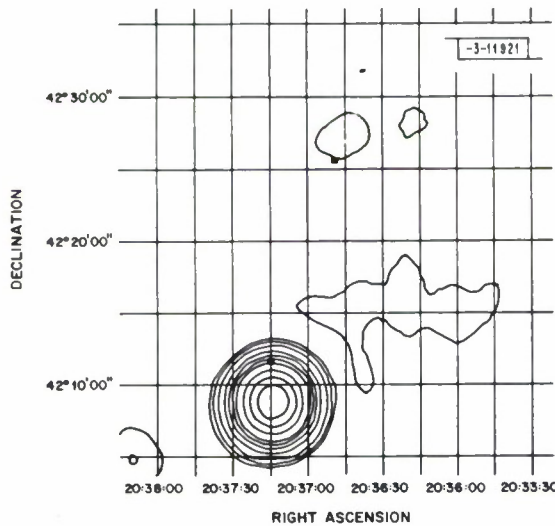

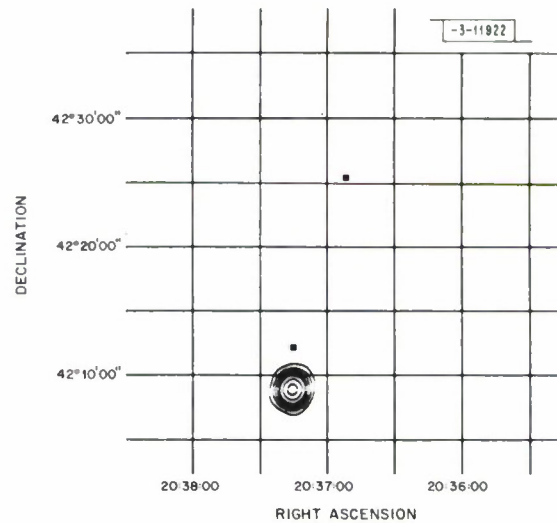Fig. 46. W75 map at 7.795 GHz at Haystack.

Fig. 47. W75 map at 15.5 GHz at Haystack.

In Fig. 46, the contour that touches W75N is marginally significant, but even if it is real, it may correspond to a ridge or extended emission north of DR21 rather than a point source at W75N. Any 8-GHz continuum source that is coincident with W75N is much weaker than the continuum source coincident with the W3 OH position (G133.9 + 1.1) which gives about 0.25°K of antenna temperature with Haystack at 8 GHz (see Table VII). The data in Fig. 47 show that there is no continuum source at 15 GHz near W75N to a limit of about 0.05°K of antenna temperature.

Figure 48 shows the spectrum of W75N at 1665 MHz as measured with the Millstone antenna. This spectrum was not restored and the features between −1 and +1.5 km/sec are from W75S seen on the side of the antenna beam. An attempted restoration of these spectra failed because the pointing of the Millstone antenna was not accurate enough. This leaves open the possibility that some W75N features exist in the range −1 to +1.5 km/sec. W75N has a 1°K left circular feature at 1667 MHz at a velocity of 5.4 km/sec. No features were observed at either 1612 or 1720 MHz to within about the same noise level and over the same velocity range as shown in Fig. 48. There is no linear polarization in the strongest feature, which is at 11.9 km/sec, to an upper limit of 14 percent.

Figure 49 shows the 1665-MHz spectrum of W75S. The strongest feature in this spectrum, which is at 0.5 km/sec, is time varying [see Zuckerman, et al. (1969)]. Figure 50 shows the details of the spectrum of this source on two particular occasions. Despite the flux variations, the linear position angle has probably remained constant in time, although it does vary as a
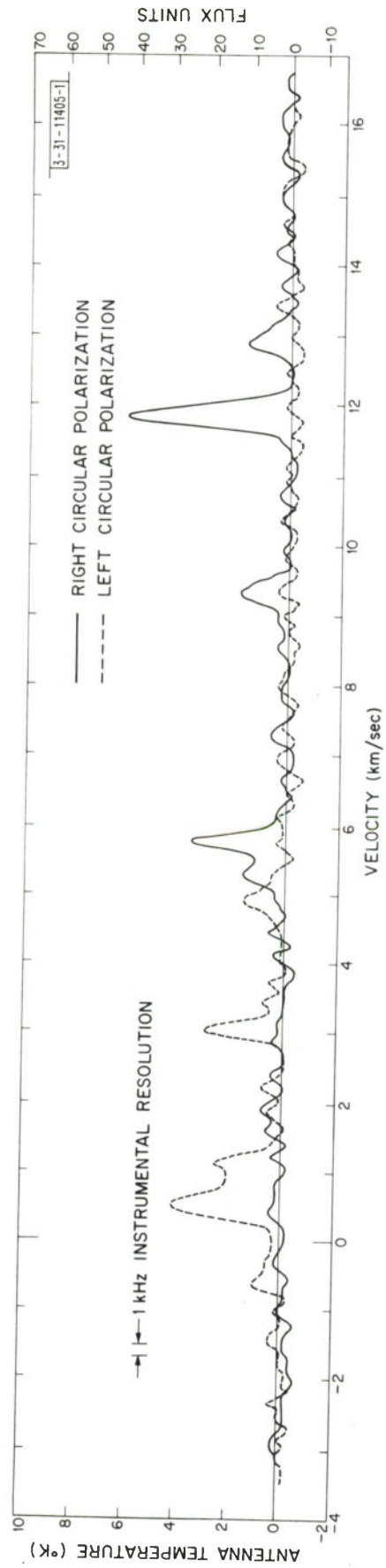
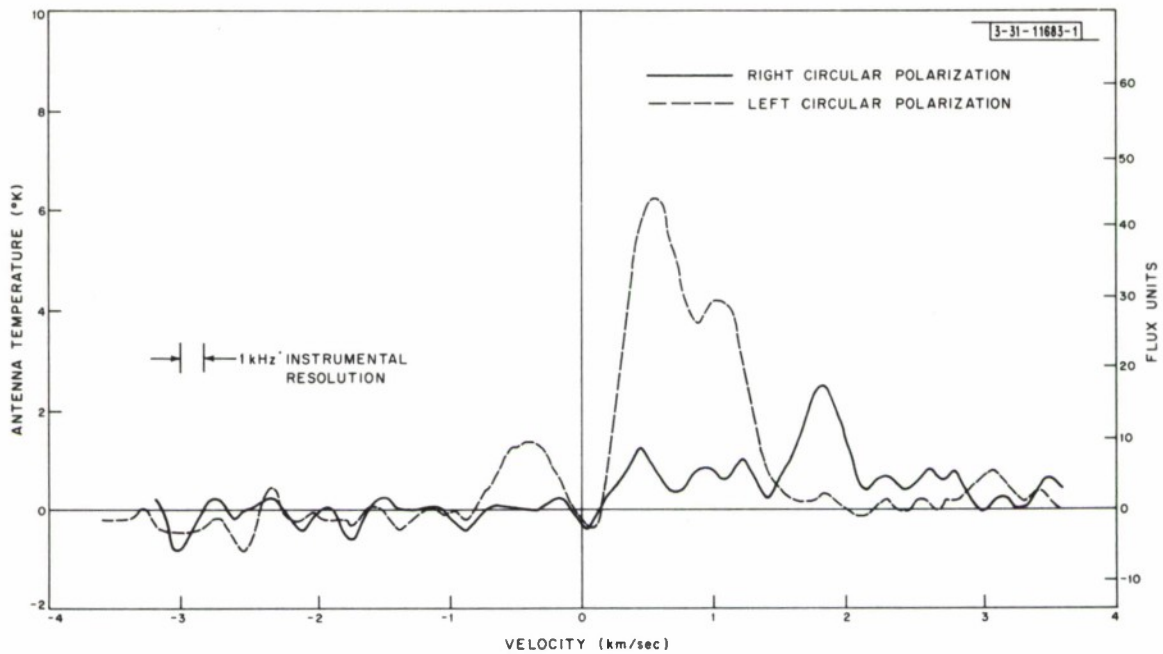Fig. 48. W75N spectra at 1665 MHz (right and left circular polarization).

FLUX UNITS

3-31-11405-1

RIGHT CIRCULAR POLARIZATION
LEFT CIRCULAR POLARIZATION

1 kHz INSTRUMENTAL RESOLUTION

VELOCITY (km/sec)

ANTENNA TEMPERATURE (°K)

68

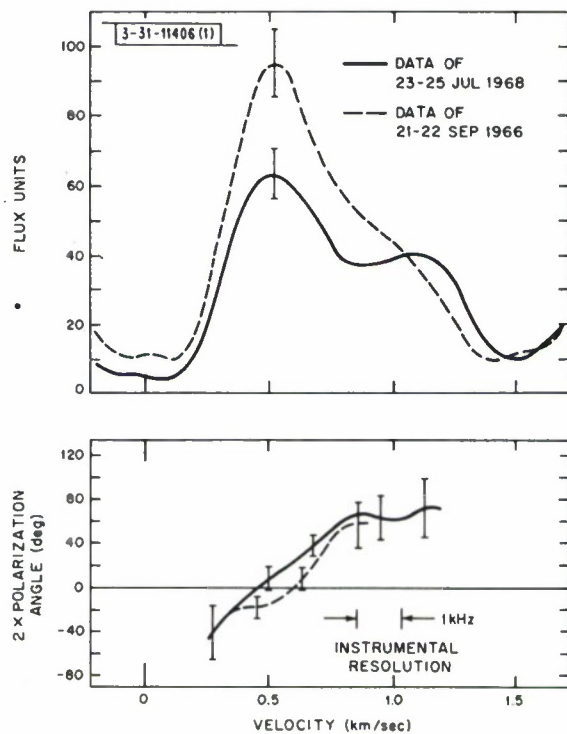Fig. 49. W75S spectra at 1665 MHz (right and left circular polarizatian).

Fig. 50. W75S spectral details at 1665 MHz for the twa dates indicated.

function of velocity across the feature. The percent linear and the percent circular polarization also vary across the feature and this variation makes it difficult to compare results made with different receivers; however, it is likely that these polarization parameters have also remained constant in time.

The Cygnus X region in which these OH emission sources are located is very complex. At least some components of the continuum emission are probably nonthermal. Downes and Rinehart (1966) concluded that DR-4 has a nonthermal spectral index, but both Dieter (1967) and Reifenstein (1968) found excited hydrogen line emission in this source. However, Reifenstein found no 109α line in DR 3, 11, and 12. However, Mrs. Dieter found the 158α line in DR 3. These confusing and partly contradictory results may arise from varying amounts of smearing by the various antenna patterns in a region in which both thermal and nonthermal sources probably exist along some lines of sight. Definitive results will come from higher resolution studies and polarization measurements. However, it seems likely that at least some components of this region will prove to be nonthermal.

Some of these observations of W75 were undertaken in collaboration with Dr. Ben Zuckerman [Zuckerman, et al. (1969)].

J. Cas A

Cas A is a relatively young supernova remnant and the brightest continuum radio source in the sky at most wavelengths. The angular diameter of the radio source is about 4 arcminutes and there is considerable structure. A 21.3-cm continuum map made by Ryle, et al. (1965) shows a ring structure such as would be seen from a shell source with a ratio of thickness to radius of about 0.25. However, there are numerous bright spots, some of which are probably not resolved by Ryle's interferometer.

The OH absorption against Cas A as observed, for example, by Rogers and Barrett (1967) and Goss (1968), is in two parts, one near zero and one near -45 km/sec radial velocity. Each of these parts breaks up into further components; there are at least four absorption features between -50 and -30 km/sec. These features are due to OH near Cas A but the zero velocity absorption is due to OH much closer to the sun.

The problem of the distribution of OH absorption across an extended source such as Cas A can be approached by at least two methods. The first method involves a sum rule for absorption and can be used to get evidence for mottling in the distribution of OH absorption without specifically measuring that OH distribution. The second method involves the use of a spectral-line interferometer. These two methods are discussed below.

Rogers and Barrett (1967) derived a sum rule for OH absorption which says that at a given frequency offset (from the line rest frequencies), the opacities in the four transitions must add up as follows:

$$\frac{d\tau_{1667}}{9} + \frac{d\tau_{1665}}{5} = d\tau_{1612} + d\tau_{1720} \tag{42}$$

For local thermodynamic equilibrium (i.e., all four excitation temperatures equal) we have also the stronger rule

$$\frac{d\tau_{1667}}{9} = \frac{d\tau_{1665}}{5} = d\tau_{1612} = d\tau_{1720} \tag{43}$$

70

Equation (42) will also hold for the total opacity along a given line of sight to the source, and if the OH along all lines of sight to the source that are accepted by the antenna beam is the same in excitation temperature and density, then Eq. (42) will hold for the measured opacities.

Rogers and Barrett (1967) checked this sum rule for their observations of the OH absorption features near zero velocity in the direction of Cas A. They showed that Eq. (42) holds for the apparent opacities to within limits set by noise in spite of the existence of emission at 1720 MHz. The emission at 1720 MHz is associated with unusually strong absorption at 1612 MHz at the same radial velocity as required by Eq. (42). However, for some other sources the sum rule does not hold for the apparent opacities [see Robinson and McGee (1967)]. This may be caused by a mottled distribution of OH across the face of the source. For example, if a small but dense cloud of OH covers only a part of the source, the apparent opacity (over the whole source) will be less than the true opacity through the cloud, as discussed below.

Let us consider the simplified case in which OH clouds cover a fraction x of the face of the source. Then we have

$$T_A \propto T_C [1 - x + x e^{-\tau_t}] + \text{terms proportional to } T_{OH} \tag{44}$$

where T_A is the measured antenna temperature, T_C is the continuum source temperature, τ_t is the true opacity of the OH in a cloud, and T_{OH} is the excitation temperature of the OH. We may define an apparent opacity τ_a as that value of τ_t which makes Eq. (44) hold for an assumed x = 1. Then

$$x(1 - e^{-\tau_t}) = 1 - e^{-\tau_a} \tag{45}$$

Since $0 \leqslant x \leqslant 1$, we underestimate τ_t if we take τ_a for τ_t, and, for a given x we underestimate τ_t by an amount which increases as τ_t increases. For example, for $x = \frac{1}{2}$ and $\tau_t = \frac{1}{2}$, we get $\tau_a = 0.22$, but for $\tau_t = 10$, we get $\tau_a = 0.69$. Equation (42) will not hold for the τ_a's unless either x = 1 or $\tau_t \ll 1$. This model is essentially a two-piece model — uniform OH over a fraction of the source and no OH over the remainder. The real situation is likely to be more complicated.

We now consider the question of detecting the presence of mottling in OH absorption using the Haystack-Millstone interferometer. For a continuum source overlaid with a uniform slab of absorbing OH, the fringe amplitude across the absorption will be proportional to the single-antenna spectrum and the fringe phase will be constant as a function of velocity although it may, of course, vary as a function of local hour angle. For a mottled distribution of OH, the fringe amplitude will depart from the single antenna spectrum and the fringe phase will no longer be constant. The departure from constancy in the fringe phase will be used as the most sensitive test for mottling.

The problem of obtaining data on the OH absorption against Cas A is discussed in Sec. lll-C. Initial measurements were made on 31 November and 1 and 2 December 1967, and again on 3 to 5 January 1968, using a 400-kHz window centered at −25 km/sec to cover both the zero and −45 km/sec absorption features. The 400-kHz window was wide enough to include several frequency fringes and the instrumental effect mentioned in Sec. lll-C was small. Most of the data from this series of observations showed no variation of phase with radial velocity except for that attributed to the instrumental effects, but a few runs at certain local hour angles showed hints of the sought-for effect as shown in Fig. 51.
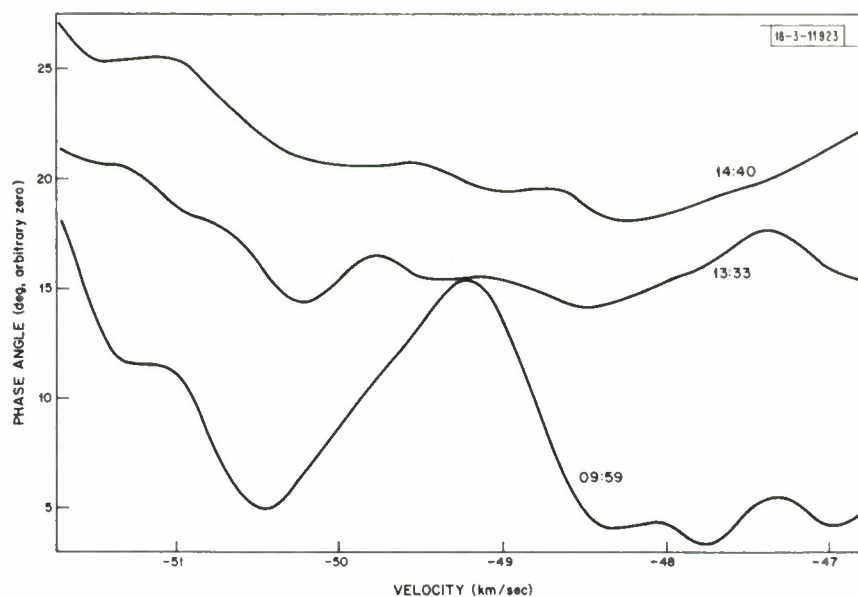
Fig. 51. Interferometer fringe phase on Cas A for the indicated local hour angles.

A further series of Haystack-Millstone interferometer observations of the OH absorption against Cas A was undertaken 27 February to 2 March 1968 using a 120-kHz and a 40-kHz window centered on those regions of the spectrum which had shown some hint of fringe phase variation at the lower resolution. For this last series of observations, the continuum fringe compensation scheme described in Sec. III-C was used. Although this scheme was only partially successful and so the data were difficult to interpret, no certain cases of fringe phase variation were observed. The upper limit that these measurements place on the mottling of the OH distribution is discussed below.

In order to calculate an upper limit to the mottling of the OH absorption against Cas A, it is necessary to have some model for the OH distribution. Aside from signal-to-noise considerations, there are some spatial distributions to which the interferometer does not respond. These are distributions whose transform is zero along the ellipses of Fig. 5. Of the other spatial distributions, some will be below the limit of detectability because of noise. If all the absorbing OH at some frequency were concentrated in a spot small compared with the interferometer fringes, and if this spot were placed so that its fringe phase were in quadrature with the continuum fringe phase (at some local hour angle), then the observed fringe phase offset would be just equal to the percentage absorption expressed in radians, that is, to about 1.5 degrees at most, when the continuum fringe amplitude is unity. However, the observed continuum fringe amplitude was as little as 10 percent, at certain local hour angles, so if the condition above had existed at such a local hour angle the fringe phase offset would be 15 degrees. No fringe phase variation was seen on the narrow band runs to an upper limit of about 5 degrees.

VI. INTERPRETATION

A. OH Source Classification Schemes

Several dozen OH emission sources are now known. These sources were found by a number of different observers engaged in a variety of programs; only two limited but systematic searches

72

for OH emission sources over selected regions of the sky have been made [Zuckerman, et al. (1969), Elldér, et al. (1969)], and these were not, of course, regions chosen at random. One must be wary of the contribution of observational selection to phenomenological associations and also be wary of statistical fluctuations in so small a sample. Table XVII lists all the OH emission sources known to the author with a classification scheme based on suggestions by Turner (1967) and Goss (1968), and used by Ball and Staelin (1968).

Class I OH emission sources emit most strongly at 1665 or 1667 MHz. The features are narrow, typically 0.6 to 4 kHz, and are usually strongly circularly, or less commonly, linearly polarized.

W3 and W49 are typical Class I sources and the descriptions in Secs. V-A and V-F can be taken as typical of this class. For example, these sources have low apparent kinetic temperatures (15 to 700°K) but very high apparent brightness temperatures (perhaps 10^{12} °K for W3). The polarization of the features is often complex with the percent circular polarization, the percent linear polarization, and the linear polarization position angle varying as a function of velocity across a feature. The shape of most features is complex (asymmetrical) suggesting either two or more overlapping features, or a line broadening mechanism which creates asymmetric line shapes. These characteristics are discussed further in Sec. VI-C.

Weaker emission in the wing transitions (1612 and 1720 MHz) is sometimes present in Class I sources and when present it is also narrow and polarized. All known time variable sources are in Class I, but this may be due to the fact that the Class I sources were more carefully studied. Almost all Class I sources seem to be associated with, but not usually coincident with H II regions. One Class I OH emission source (Orion A) also has an IR star [Raimond and Eliasson (1967)] and recent reports indicate that others may also have one [Neugebauer, et al. (1968)]. Many Class I sources also have SNR's or NTS's somewhere around them, but these are far enough away so that one would not suspect any connection if this association did not occur so frequently. Even if these phenomenological associations stand the test of future observations, one cannot necessarily infer an interaction mechanism.

Class II_a OH emission sources emit most strongly at 1720 MHz. The features are wider, typically 4 to 20 kHz, and not strongly polarized. There is usually no emission at the other transitions. There are only a few sources in this class, but an association with SNR's seems likely. This association has also been pointed out by Goss and Robinson (1968). In Sec. VI-B, one possible interaction mechanism between SNR's and OH emission sources is considered.

Class II_b OH emission sources emit most strongly at 1612 MHz. The 1612-MHz features from Class II_b sources are wider than the features from Class I sources, perhaps even wider than those from Class II_a sources, and are not strongly polarized. Several of these sources also show emission at the main transitions (1665 and 1667 MHz) and in at least one case (NML Cygnus) the 1665-MHz emission is similar to that from Class I sources in being circularly polarized and quite narrow in velocity. Some of the Class II_b sources are associated with IR stars and some with H II regions. But since the IR star surveys are incomplete, it may turn out that all the Class II_b sources have IR stars. The similarities between Class II_b and Class I lead one to speculate that the differences may be of degree and not of kind. No Class II_b sources are known to have 1720-MHz emission.

This classification scheme does not contain the "Heiles Clouds" [Heiles (1968), Cudaback and Heiles (1969)] – regions emitting apparently normal (i.e., LTE) OH emission. These clouds are associated with dusty regions and Heiles interprets his results to mean that the OH in dusty

73

TABLE XVII
CLASSIFICATION OF OH EMISSION SOURCES

Source Name(s)	Transition (MHz) *				Class	Nearest 18-cm Continuum	l^{II} (deg)	b^{II} (deg)	Distance	References †
	1612	1665	1667	1720						
CIT3 IR0103 + 12C	U̲	O	U	O	II$_b$		128.6	−50.1		20,21
G127.7 + 14.0			X		HC		127.7	+14.0		5
W3 IC1795	C,A	E̲,A	C,A	C,A	I$_a$	H II	133.95	+1.06	2.6 to 3.2	1,15
G159.7 − 19.6			X		HC		159.7	−19.6		5
NML Taurus	U̲	O ·	U	O	II$_b$	<20 fu	178.0	−31.4		20,21
G168.7 − 15.5			X		HC		168.7	−15.5		5
G173.3 − 16.3			X		HC		173.3	−16.3		5
G173.9 − 15.9			X		HC		173.9	−15.9		5
Cloud 2 G174.6 − 13.7			X		HC		174.6	−13.7		5, 12
G171.4 − 10.6			X		HC		171.4	−10.6		5
IR0507 + 52	U	O	O	O	II$_b$	<20 fu	156.4	+7.8		21
G178.9 − 6.7			X		HC		178.9	−6.7		5
Orion A	C	C̲,T	X	A	I$_a$	H II	209.0	−19.4		17,19
G214.5 − 19.9			X		HC		214.5	−19.9		5
G203.3 − 11.2			X		HC		203.3	−11.2		5
G201.5 + 0.6			X		HC		201.5	+0.6		5
VY Canis Majoris	U̲	X	X	O	II$_b$	<20 fu	240	−6		6,21
RCW38		A,U̲?	A,U?	A	I$_a$?	H II	267.9	−1.1	0.5	13
RCW36		X,A			I$_a$?	H II?	265.1	+1.5	1.5, 3.5	13
IR0942 − 21	U	O?	O?	O	II$_b$	<20 fu	255.8	+23.35		21
RCW46		A,X			I$_a$?	H II?	282.0	−1.2	4?	13
G284.2 − 0.8 (RCW48–RCW49)	U	U̲,C	U,A	O	I$_a$?	H II	284.2	−0.8	3.8, 4.9?	14
1308−62S (RCW74)		E,C	A		I$_a$?	H II	305.3	+0.2	3, 8.5	13
1308−62N		E̲	A		I$_a$?	H II	305.3	+0.2	3, 8.5	13
1404−61		X			I$_a$?		311.9	+0.1	12.5	13
CIT7 IR1525 + 19G	U̲	U	U	O	II$_b$	<20 fu	29.5	+53.5		20,21
1541−53		A,E			I$_a$?		326.7	+0.6	15.5 (or 1)	13
G4.2 + 35.8 L134			X		HC		4.2	+35.8		5, 12
1608−51 (MHR49)	?	A,C̲	A		I$_a$?		331.5	−0.1	11 (or 6.5)	13
1617−50N		C,A	A		I$_a$		332.2	−0.4	3 to 4	13
1617−50S		A	C,A		I$_b$?		332.2	−0.4	3 to 4	13
1618−49		A,X			I$_a$?		333.6	−0.2	2 to 2.5	13
G352.9 + 16.7			X		HC		352.9	+16.7		5
G353.4 + 16.9 Cloud 4			X		HC		353.4	+16.9		5, 12
NGC 6334S	?	E,T,A	E,T,A	A(X?)	I$_b$	H II	351.2	+0.7	0.7 to 1.3 (?)	1,2,8,11,13,19

* See notes at end of table.

† See references at end of table.

74

	Transition (MHz)					Nearest 18-cm	l^{II}	b^{II}		
Source Name(s)	1612	1665	1667	1720	Class	Continuum	(deg)	(deg)	Distance	References [†]
NGC 6334N	?	E,A	C,A	X,A	I_a	H II	351.	+0.5	0.7 to 1.2 (?)	1,2,8,11,13,19
NGC 6357 W22	A	A,X	A	A	I_a?	H II	353.2	+0.67	0.6 or 1.3	9,13
IR1734 − 32 (NGC 6383?)	U	O?	O?	O	II_b?	H II?	356.4	−0.3		21
Sag A-I	O?	X,A	A?	O?	I_a	NTS?	359.95	−0.15	10?	19
Sag A-II	A	A	A	A,U	II_a	NTS?	0	0	10?	10
Sgr. B2 (W24−B2)	U or C,A	C,A	C,A	A	I_b	H II?	0.7	−0.0	10?	17,19
W28S G5.9 − 0.4 W28A_2	U	C,U	C,U	A?	II_b	H II	5.94	−0.40	3.0	4,18
W28N	A	A	A	U	II_a	SNR + H II	6.76	−0.27	1.3 to 3.6	1,3,4,9,10
W33 IC4701	O	E,T,A	C,A	A	I_a	H II + SNR	12.7	−0.0	4.7 or 14.8	4,9,18
W41	X	A	A	?	II_b	SNR + H II (?)	23.2	−0.3	5.8 or 12.6	9,18
G23.5 + 8.2			X		HC		23.5	+8.2		5
W42	X?	A	X	0	I_b	NTS?	24.6	−0.1		9,18
G27.3 + 4.3			X		HC		27.3	+4.3		5
G27.0 + 3.5			X		HC	.	27.0	+3.5		5
G27.1 + 3.5			X		HC		27.1	+3.5		5
W43I	A	A	A	X,A	II_a		30.8	−0.1	0.6 to 1.0	9,18
W43II	X,A	E,A	E,A	X,A	I_b	H II	30.8	−0.1	6.5 to 7.5	4,9,18
W43III	U	X	X	O	II_b	H II	30.8	−0.1	14?	4,9,18
W44I	A	A	A	U	II_a	SNR + H II	34.6	−0.4	1.6 to 3.4	1,3,4,10,18
W44II	X	A	A	A	II_b	?	34.6	−0.4	1	9,10,18
IR1903 + 08	U	?	?	O	II_b	<20 fu	41.95	+0.45		21
W49S	C?	C	C?	C,T?,A	I_a	H II	43.2	−0.0	14	1,2,13,17,19,22
W49N	C?	C	C?	C,T?,A	I_a	H II	43.2	−0.0	14	1,2,13,17,19,22
W51-I	C,A	U,C,A	A(X?)	C(E?)	I_a	H II (NTS?)	49.5	−0.4	6.5	1,2,9,19
W51-II	A	A	A	X	II_a	H II?	49.5	−0.4	0.43	1,2,9,19
ON3 W58, CTB82 NGC 6857	O	C	C	C	II_a	H II	70.37	+1.60	8.2	7
ON1	O	C	C(?)	O	I_a	None	69.58	+0.96	1.8 or 5.2	7
ON2 W64, CTB90	O	C	C	O	I_a	H II?	75.75	+0.35	5.7	7
ON4	U	C?	O	O	II_b	H II	77.93	+0.17	8.1	7
W75N	O	C	C?	O	I_a	H II (or none)	81.86	+0.76	1.5?	1,19,22
W75S	A	E,T	A	A?	I_a	H II	81.75	+0.54	1.5? (or 6?)	1,2,17,19.22
NML Cygnus	U	C	C	O	II_b	< 5 fu	80.8	−1.9	?<300 pc ?	21,22
Cas A	A	A	A	A,L	II_a		111.7	−2.1		9,18
G114.5 + 14.6 Cloud 1B			X		HC		114.5	+14.6		5,12

TABLE XVII (Continued)

*Notes

A   Absorption
C   Circularly polarized emission
L   Linearly polarized emission
E   Both circular and linear emission present
U   Substantially unpolarized (<20 percent) emission

X   Emission, but polarization unknown
?   Questionable
T   Time variable
0   No emission or absorption detected
—   Underline indicates transition of strongest emission.

† References

1. See Sec. V of this report
2. Ball and Meeks (1968)
3. Ball and Stoelin (1968)
4. Coles, et al. (1968)
5. Cudaback and Heiles (1969)
6. Eliasson and Bartlett (1969)
7. Elldér, et al. (1969)
8. Gardner, et al. (1967)
9. Goss (1968)
10. Goss and Robinson (1968)
11. Goss, et al. (1969)
12. Heiles (1968)
13. McGee, et al. (1967)
14. Manchester, et al. (1969)
15. Meeks, et al. (1966)
16. Menon (1967)
17. Palmer and Zuckerman (1967)
18. Turner (1969)
19. Weaver, et al. (1968)
20. Wilson and Barrett (1968)
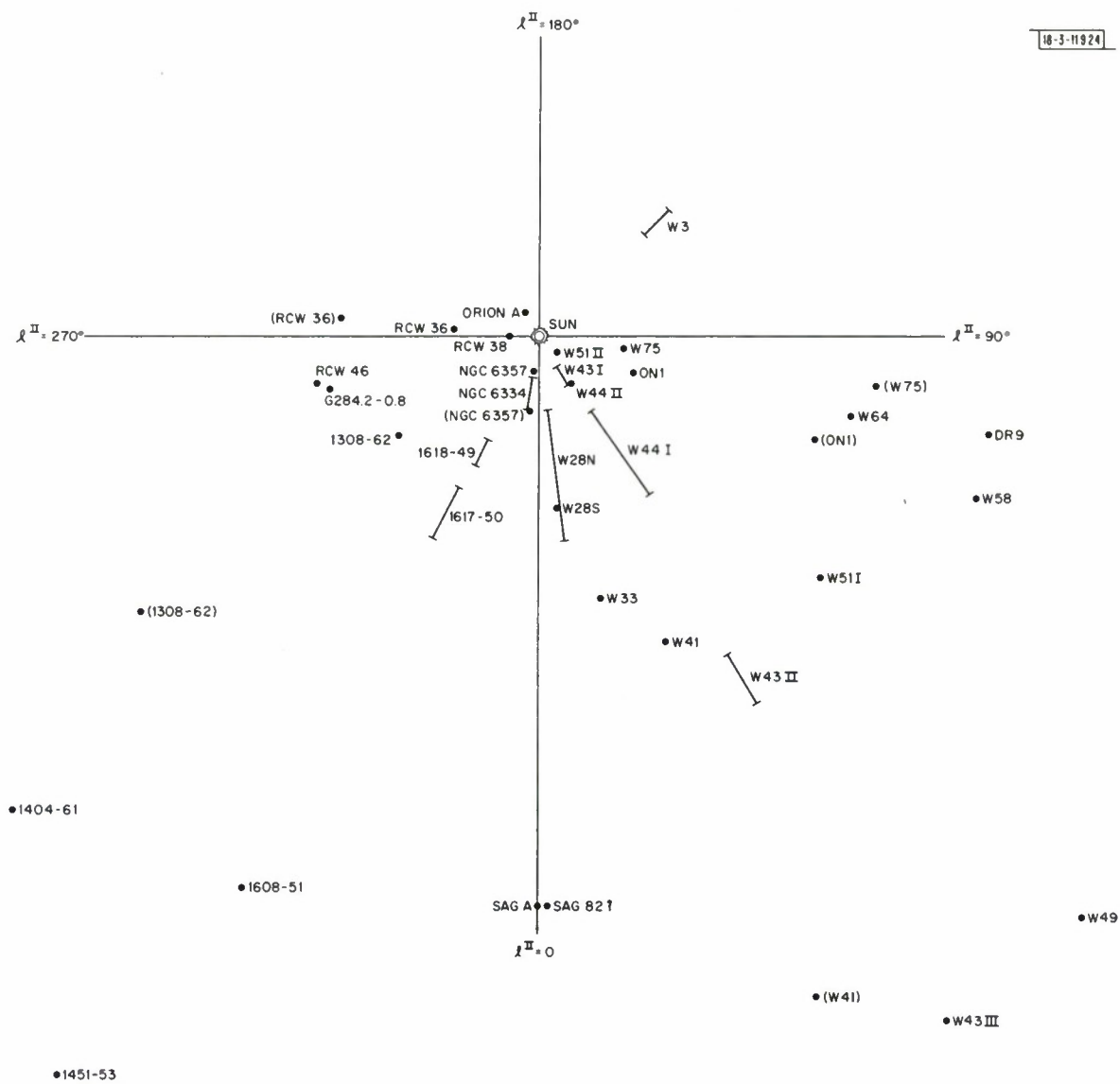21. Wilson and Barrett (1969)
22. Zuckerman, et al. (1969)

Fig. 52. Location of OH emission sources in the galactic plane.

regions has a higher excitation temperature compared with OH in the general interstellar medium, and perhaps a higher relative density also. The polarization of these regions has not been measured and the line ratios are known only very crudely. If the OH in Heiles' clouds does turn out to be in LTE, it will be almost the only extraterrestrial OH known to be in such a state.

The cases of anomalous absorption [Goss (1968)] which may be combinations of absorption and anomalous emission are also not included and not listed in Table XVII. Goss states that there is no case in his survey for which the OH absorption can be characterized by LTE (i.e., a single excitation temperature for the four 18-cm OH transitions). It is clear that some mechanism must be effective in the general interstellar medium which produces these unequal excitation temperatures in OH. It is not clear what this mechanism is or whether the same mechanism produces the population inversion in some or all of the anomalous OH emission sources.

Figure 52 shows a projection onto the galactic plane of all the OH emission sources (from Table XVII) that have some estimate for their distance. No obvious patterns can be seen in this plot, in particular:

(1) The more distant (and intrinsically stronger) sources do not all belong to a given class.

(2) The closer sources are not more strongly polarized, although there may perhaps be some tendency for distant sources to have a lower percentage of linear polarization.

(3) There are at least a few sources which do not lie in spiral arms as traced by neutral hydrogen emission.

These OH emission sources are quite strongly concentrated toward the galactic plane; the largest well-established Z distance is 230 pcs for W58 (ON-3). And no sources are known to be farther than about 13 kpc from the galactic center.

B. Action of Ions on OH Molecules

1. Introduction

Because of the apparent phenomenological association between OH emission sources and SNRs, it is desirable to reexamine the interaction between ions and OH molecules to determine whether this interaction can provide either a pumping mechanism, or a spoiler mechanism to explain the peculiarities of those OH sources (Class II_a) most closely associated with SNRs. The problem of the interaction of ions and OH molecules has been considered by Johnston (1967) and Turner (1967) using an approach that made use of the Born Approximation, and by Rogers (1964), Rogers and Barrett (1968), and Goss and Field (1968) using time-dependent perturbation theory based on an approach by Purcell (1952). Using the latter approach this study extends the previous work by (a) employing the relativistically correct form of the equations and taking relativistic ions into consideration, (b) dropping some of the approximations made in previous work, and (c) using instead of the Maxwell equation, a form for the ion energy density which is thought to be appropriate for the vicinity of a supernova remnant.

2. Order-of-Magnitude of the Effect

It is perhaps best to begin by doing an order-of-magnitude calculation to indicate that it is at least conceivable that the charged particle — OH molecule interaction in the vicinity of an SNR can significantly affect the observed OH radio emission.

We choose the 1720-MHz OH emission from W28 because it is well known (but probably stronger than the average type II_a OH emission source) and we calculate the spectral flux for the two strong features as 9.55×10^{-21} watts/m^2 [Ball and Staelin (1968)]. Using the distance of 4200 pcs suggested by Goss (1968), which is much larger than the 1300 pcs suggested by Poveda and Woltjer (1968), we calculate a spectral luminosity of 1.9×10^{21} watts and this corresponds to about 1.7×10^{45} photons/sec. This calculation assumes that the OH emission is isotropic or at least that the spectral intensity in the direction of the earth is typical of the source. If we had used 1300 pcs for the distance, the inferred spectral luminosity would be smaller by about an order of magnitude.

We have only a rather large upper limit on the angular size of the OH emission source in W28 so we assume a diameter of 4000 au which is approximately the value obtained by Moran, et al. (1968) for the total size of the emitting region in W3. From this we calculate a volume of 9×10^{50} cm^3.

Inside this volume we assume there are 10^{-2} OH molecules/cm^3 and 500 electrons/cm^3 with speeds of 10 to 100 km/sec. This OH density can only be a guess, but it is clear that something is special about the OH emitting region to distinguish it from other nearby regions that do not have OH emission. This high an OH density was used by other workers who calculated maser models. The electron density of 500 electrons/cm^3 is lower than the maximum estimate of Minkowski (1968) and others, but the speed is also slower than the speed of mass motions observed in SNRs. We now read off a transition rate of 10^{-5} cm^3/sec from Fig. 4 of Rogers and Barrett (1968) and with the numbers above we calculate 4.5×10^{46} transitions/sec in the region. This is about an order of magnitude larger than the number of photons/sec calculated above.

We conclude that if the conditions assumed above are reasonable, then the interaction between OH molecules and passing ions will certainly be important and may in fact be sufficient to explain the source of energy for the OH emission.

For the case in which the ions are the sole energy source, another point is worth noting. Because the mechanism under consideration is not a maser, i.e., no inversion of the population levels is expected, the brightness temperature of the 18-cm radiation cannot exceed the equivalent kinetic temperature of the ions. For the case in which the ions have a non-Maxwellian velocity distribution, we must at least have a substantial number of ions with energies comparable to k times the brightness temperature. To see whether this is the case, we first calculate the peak brightness temperature for Feature 1 of W28 at 1720 MHz as 2.5×10^7 °K using the size assumed above. We have no way of knowing whether this is reasonable for a type II_a source, but the type I source in W3 has much higher brightness temperatures [Moran, et al. (1968)]. To correspond to this kinetic temperature, an electron must move at about 3×10^9 cm/sec and a proton about a fortieth of this. This electron speed is nearly relativistic, which suggests the need for a relativistic analysis, and is much higher than we assumed previously, which illustrates that we do not have the whole story.

3. Equivalent Electric Field Energy Density and the Transition Probability

In this section we rederive the appropriate equations of Rogers (1964), Rogers and Barrett (1968) and Goss and Field (1968) in their relativistically correct form.

Consider an ion with charge q and velocity $\vec{v}$ passing an OH molecule with impact parameter b. Figure 53 shows the situation. We assume that the ion is not appreciably deflected by

the OH molecule.   According to Jackson (1962), the nonzero components of $\vec{E}$ and $\vec{B}$ are
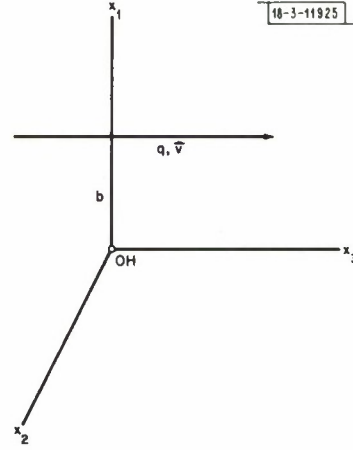
$$E_1 = \frac{\gamma q b}{(b^2 + \gamma^2 v^2 t^2)^{3/2}} \tag{46}$$

$$E_3 = -\frac{\gamma q v t}{(b^2 + \gamma^2 v^2 t^2)^{3/2}} \tag{47}$$

$$B_2 = \beta E_1 \tag{48}$$

where $\beta = v/c$ and $\gamma = (1 - \beta^2)^{-1/2}$.   Note that in the relativistic limit $(v \to c)$ these equations are the same as the equations describing a pulse of plane polarized electromagnetic radiation propagating in the x_3 direction.

Fig. 53.   Ion passing an OH molecule.

To use the approach suggested by Purcell (1952) we need the Fourier spectrum of the $\vec{E}$ field. If we define

$$\widetilde{F}(\omega) \equiv \int_{-\infty}^{\infty} F(t)\, e^{i\omega t}\, dt \tag{49}$$

then we get

$$\widetilde{E}_1(\omega) = \frac{2q\omega}{\gamma v^2}\, K_1(\frac{\omega b}{\gamma v}) \tag{50}$$

$$\widetilde{E}_3(\omega) = -\frac{2iq\omega}{\gamma^2 v^2}\, K_0(\frac{\omega b}{\gamma v}) \tag{51}$$

[see Jackson (1962)].   The K functions are the modified Bessel functions, the properties of which are summarized in Abramowitz and Stegun (1964).   Subsequent formulae involving these functions are either taken from Abramowitz and Stegun or are derivable from equations given by them.

The energy density and also the interaction energy with a harmonic oscillator are proportional to $|\vec{E}(\omega)|^2$ which is

$$|\vec{E}(\omega)|^2 = \frac{4q^2\omega^2}{\gamma^2 v^4} \left[K_1^2(\frac{\omega b}{\gamma v}) + \frac{1}{\gamma^2}\, K_0^2(\frac{\omega b}{\gamma v}) \right] \tag{52}$$

Several properties of this equation are worth noting:

(a) $|\vec{E}(\omega)|^2$ falls exponentially at large b [because $K_0(x) \to K_1(x) \to (\pi/2x)^{1/2}$ $\exp(-x)$ for $x \to \infty$].

(b) Although the E_3 spectrum has a peak at $\omega \simeq 1.35\,\gamma v/b$ [because $xK_0(x) =$ maximum at $x \simeq 1.35$] there is no peak for the total $|\vec{E}(\omega)|^2$ [because $xK_1(x) =$ maximum at $x = 0$].

(c) Although this equation has a singularity for $b \to 0$, it is well defined for $\omega \to 0$ and also for $\gamma \to \infty$.

Using Eq. (52) we may write the relativistically correct equivalent of Eq. (18) in Rogers and Barrett (1968) as

$$P_{j \to i}(b) = \frac{|\mu_{ij}|^2\, 4q^2\omega^2}{3\,\hbar^2\gamma^2 v^4}\left[K_1^2(\frac{\omega b}{\gamma v}) + \frac{1}{\gamma^2}\,K_0^2(\frac{\omega b}{\gamma v})\right] \tag{53}$$

where μ_{ij} is the electric dipole moment connecting the two states in question, and $P_{j \to i}$ is the probability of producing a transition.

In the low frequency or high energy limit $\omega \ll \gamma v/b$ we get the approximation

$$|\vec{E}(\omega)|^2 \simeq \frac{4q^2}{v^2 b^2}\left\{1 + \frac{1}{\gamma^2}\,[\frac{\omega b}{\gamma v}\,\ln(\frac{\omega b}{\gamma v})]^2\right\} \simeq \frac{4q^2}{v^2 b^2} \tag{54}$$

[because $xk_1(x) \to 1$, $xK_0(x) \to 0$ as $x \to 0$]. Note that:

(a) The spectrum becomes flat (the ω dependence cancels out) corresponding to the pulse character of $\vec{E}(t)$.

(b) $|\vec{E}(\omega)|^2$ falls as $1/b^2$ rather than exponentially as above.

In the high frequency or low speed limit $\omega \gg \gamma v/b$ we get the approximation

$$|\vec{E}(\omega)|^2 \simeq \frac{2\pi q^2\omega}{\gamma v^3 b}\left[1 + \frac{1}{\gamma^2}\right]\exp(-\frac{2\omega b}{\gamma v}) \quad . \tag{55}$$

This spectrum is illustrated schematically in Fig. 54.

For the conditions under which Eq. (54) holds ($\omega \ll \gamma v/b$) we have the approximation

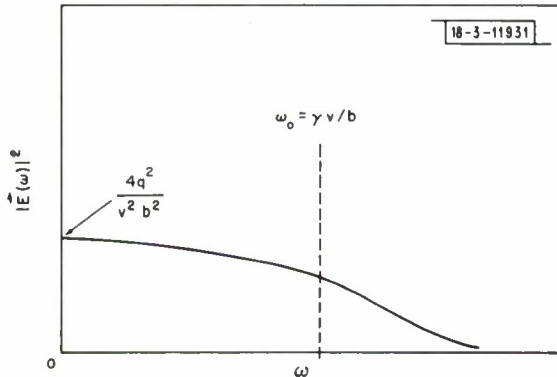$$P_{j \to i}(b) \simeq \frac{|\mu_{ij}|^2\, 4q^2}{3\,\hbar^2 v^2 b^2} \tag{56}$$

Fig. 54. Equivalent energy spectrum of a passing ion.

80

provided $P_{j \to i}(b) < \frac{1}{2}$ Following Rogers and Barrett (1968) we define r_1 by $P_{j \to i}(r_1) = \frac{1}{2}$ in Eq. (56) and calculate

$$r_1^2 = \frac{8q^2 |\mu_{ij}|^2}{3\hbar^2 v^2} \tag{57}$$

(The equivalent of Eq. (57) in Rogers and Barrett contains a misprint; it should have an exponent of $\frac{1}{2}$.) The use of Eq. (56) to calculate r_1 would be incorrect under circumstances in which $P_{j \to i} \sim \frac{1}{2}$ but $\omega \overset{\sim}{>} \gamma v/r_1$.   We shall see below that this is unlikely.

In summary, provided $\omega \ll \gamma v/r_1$, we use $P_{j \to i}(b) = \frac{1}{2}$ for $b < r_1$ and Eq. (56) for $b > r_1$ unless $\omega \overset{\sim}{>} \gamma v/b$ in which case we must use Eq. (53).   If $\omega \overset{\sim}{>} \gamma v/r_1$, we must use Eq. (53) both for calculating r_1 and for $P_{j \to i}(b)$ for $b > r_1$.

We now assume that the OH molecule is in a stream of mono-energetic ions characterized by N_1, their number density per unit volume.   Then the number of ions passing the OH molecule per unit time with impact parameters in the range b to b + db will be

$$dN_1 = N_1 v 2\pi b \, db \tag{58}$$

We wish to evaluate

$$R_1(v) = \int P_{j \to i}(b) \, N_1 v 2\pi b \, db = 2\pi N_1 v \left[\frac{r_1^2}{4} + \int_{r_1}^{\infty} P_{j \to i}(b) \, b \, db \right] \tag{59}$$

which is the rate of $j \to i$ transitions caused by the N_1 ions.   Using Eq. (53) [as we must because the approximation used to get Eq. (56) breaks down somewhere in the range of integration], the integral in Eq. (59) is

$$\int_{r_1}^{\infty} P_{j \to i}(b) \, db = \frac{|\mu_{ij}|^2 \, 4q^2 \omega^2}{3\hbar^2 \gamma^2 v^4} \int_{r_1}^{\infty} \left[K_1^2\left(\frac{\omega b}{\gamma v}\right) + \frac{1}{\gamma^2} K_0^2\left(\frac{\omega b}{\gamma v}\right) \right] b \, db$$

$$= \frac{|\mu_{ij}|^2 \, 4q^2}{3\hbar^2 v^2} \int_{x=\omega r_1/\gamma v}^{\infty} \left[K_1^2(x) + \frac{1}{\gamma^2} K_0^2(x) \right] x \, dx \tag{60}$$

These integrals can be done;

$$\int x K_0^2(x) \, dx = \frac{x^2}{2} \left[K_0^2(x) - K_1^2(x) \right] \tag{61}$$

$$\int x K_1^2(x) \, dx = \frac{x^2}{2} \left[K_1^2(x) - K_0^2(x) \right] - x K_0(x) K_1(x) \tag{62}$$

so Eq. (60) becomes, after some manipulation,

$$\int_{r_1}^{\infty} P_{ji}(b) \, b \, db = \frac{|\mu_{ij}|^2 \, 4q^2}{3\hbar^2 v^2} \left\{ \frac{\omega^2 r_1^2}{2\gamma^2 c^2} \left[K_0^2\left(\frac{\omega r_1}{\gamma v}\right) - K_1^2\left(\frac{\omega r_1}{\gamma v}\right) \right] \right.$$

$$\left. + \frac{\omega r_1}{\gamma v} K_0\left(\frac{\omega r_1}{\gamma v}\right) K_1\left(\frac{\omega r_1}{\gamma v}\right) \right\} \tag{63}$$

However, we have already assumed that $\omega \ll \gamma v/r_1$, so Eq. (63) reduces to

$$\int_{r_1}^{\infty} P_{j \to i}(b)\, b\, db \simeq \frac{|\mu_{ij}|^2\, 4q^2}{3\hbar^2 v^2} \left[-\frac{\beta^2}{2} - \ln\left(\frac{\omega r_1}{\gamma v}\right) \right] \tag{64}$$

[because $K_0(x) \to -\ln(x)$ for $x \to 0$]. Now we may write Eq. (59) as

$$R_1(v) \simeq \frac{|\mu_{ij}|^2\, 4\pi N_1 q^2}{3\hbar^2 v} \left\{ 1 - \beta^2 - \ln\left[\frac{|\mu_{ij}|^2\, 8q^2\omega^2}{3\hbar^2\gamma^2 v^2} \right] \right\} \tag{65}$$

This equation is comparable with Eq. (24) of Rogers and Barrett (1968) and Eq. (12) of Purcell (1952), but Eq. (65) is for mono-energetic ions and so differs in detail.

We now assume that the OH molecule is in a stream of ions characterized by an energy spectrum such as that shown in Fig. 55(a), i.e., a power law for energies above a limiting energy E_0 and a constant below E_0. We assume that $E_0 \ll m_0 C^2$, i.e., that the cutoff energy E_0 is well below the relativistic range, and we assume $1 < \alpha \simeq 1.5$ or 2.

The form of this energy spectrum and the assumption about E_0 perhaps deserve some comment. The power law energy spectrum, and values for α and K but not E_0, are determined for electrons in supernova remnants from radio observations of the synchrotron continuum radiation and some assumption about the magnetic field. The energy spectrum is therefore known only for electrons in a limited range of relativistic energies. It is also not clear just what part of a supernova remnant is being observed in the radio continuum. It is likely that conditions near an OH emission source on the edge of a supernova remnant are very different. We shall see below that ions with low energies are very important, and the energy spectrum in Fig. 55(a) should be considered only as plausible but certainly not uniquely specified by any observations.
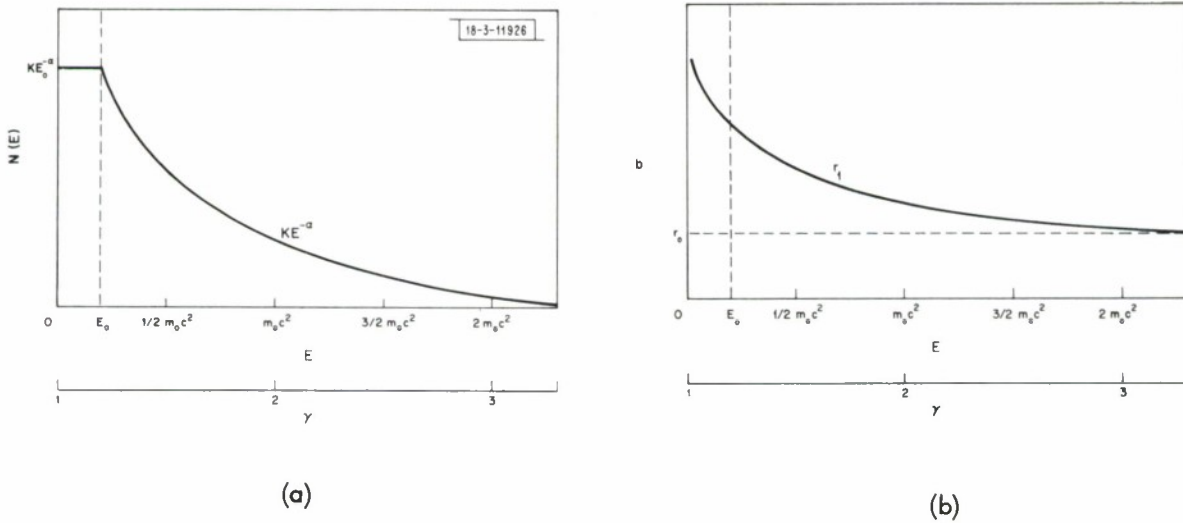

(a)   (b)

Fig. 55. Schematic illustration of the cross-section integral.

Furthermore, we need to determine the third parameter E_o. We do this by specifying that the total ion density — the integral under the curve in Fig. 55(a) — be some reasonable but assumed value.

The total ion density [from Fig. 55(a)] is

$$N = \int_0^\infty N(E)\, dE = KE_o^{1-\alpha}\, [\frac{\alpha}{\alpha - 1}] \tag{66}$$

We now wish to perform the total rate integral which is

$$\Omega = \int_{E=0}^\infty \frac{R_1[v(E)]}{N_1}\, N(E)\, dE \tag{67}$$

This will give us the number of transitions per OH molecule per second for an OH molecule in the ion field corresponding to $N(E)$. It will be necessary to break up the range of the integral in Eq. (67) into three pieces:

(1) $E < E_o$ for which $N(E) = KE_o^{-\alpha}$ = constant and for which $E = 1/2 m_o v^2$;

(2) $E_o < E < 1/2 m_o c^2$ for which $N(E) = KE^{-\alpha}$ and for which we assume
$E \simeq 1/2 m_o v^2$, and

(3) $E > 1/2 m_o c^2$ for which $N(E) = KE^{-\alpha}$ and for which we assume $v \simeq c$
(but use the correct value for γ, of course).

The results of these three integrals are

$$\Omega_1 = BE_o^{-\alpha} m_o \left(\frac{2E_o}{m}\right)^{1/2} \ln\left(\frac{a2E_o}{m_o e^2}\right) \tag{68}$$

$$\Omega_2 = \frac{B(m_o/2)^{-\alpha} m_o}{(1 - 2\alpha)} \left\{ c^{1-2\alpha} \ln\left(\frac{ac^2}{e^{2/(1-2\alpha)}}\right) - \left(\frac{2E_o}{m_o}\right)^{1/2-\alpha} \right.$$

$$\left. \times \ln \frac{a2E_o}{m_o e^{2/(1-2\alpha)}} \right\} \tag{69}$$

and

$$\Omega_3 = \frac{B}{C} \left(\frac{m_o c^2}{2}\right)^{1-\alpha} \frac{1}{\alpha - 1} \ln\left(\frac{ac^2}{4e^{2/(1-\alpha)}}\right) \tag{70}$$

where

$$a = \frac{3\hbar^2 e}{|\mu_{ij}|^2 8q^2\omega^2} \tag{71}$$

and

$$B = \frac{|\mu_{ij}|^2}{3\hbar^2} 4\pi q^2 K \tag{72}$$

83

For any reasonable value of N (several hundred/cm^3) and with values of K and α usually used, we get $E_o \ll m_o c^2$ and this immediately shows that Ω_3 and the first term of Ω_2 are negligible with respect to Ω_1 and the second term of Ω_2, which are comparable. This result means that the low energy electrons contribute almost all of the interaction. And the form for N(E) is probably not correct at low energies. The sought-for effect (coupling of the OH microwave transitions to passing high energy ions) exists but it is completely dominated by the interaction with low energy ions for the energy spectrum assumed. The interaction between OH molecules and passing ions can explain neither the 1720-MHz emission in type IIa sources nor the nonequilibrium excitation temperature in the OH clouds observed by Goss (1968).

In conclusion it seems likely that the apparent association between OH emission sources and SNRs is an association in the sense that certain regions of the galaxy, perhaps because of the chemical composition of the interstellar medium, the presence of large amounts of dust, or other causes, tend to form stars with the kind of circumstellar clouds that show OH emission and also tend to form the kind of stars that explode as supernovae. Thus the two kinds of objects are proximate in space but probably not interacting. Very likely the association between OH emission sources and H II regions is of the same character. The association between OH emission sources and IR stars will probably turn out to be a more direct causal relationship.

C. Physical Pictures of OH Emission Sources

It was pointed out above that most OH emission features that contain linear polarization and also some that contain only circular polarization show a variation of the polarization properties (the percent circular and the percent linear polarization and the linear polarization position angle) as a function of velocity across the feature. There are several possible causes for this behavior:

(1) The feature itself may have, intrinsically, polarization properties that vary as a function of frequency or velocity. Until the mechanism which produces the polarization is understood, this remains a possibility at least for some features in some sources.

(2) If we say, rather arbitrarily, that an individual feature is to be Gaussian or at least symmetrical in shape, then most spectra are made up of composite features and the variation of the polarization properties may be due to the incoherent overlap of separate features, each of which has its own polarization.

(3) Faraday rotation in the intervening medium rotates the plane of linear polarization as a function of frequency. However, this is unlikely to be the cause of the rotation of the linear polarization position angle across the spectrum if the Faraday rotation is to take place either in the interstellar medium or in the earth's ionosphere, because the rotation measures are far too small. For example, to Taurus A the total rotation from $\lambda = 0$ to $\lambda = 20$ cm is only about 60° [see Kraus (1966), p. 146]. It is conceivable that the OH emission originates inside a region of much higher rotation measure.

Regardless of which of these possibilities turns out to be correct, it is likely that some of the features in some of the sources (e.g., W49 and W51) will turn out to be more highly polarized when examined with higher frequency and spatial resolution.

Moran, et al. (1968) show a map of the 1665-MHz OH emission from the W3 region. They find that each feature comes from a spot or small region 0.02 arcsecond or less in size, but the separation among these spots is typically 0.2 to 2 arcseconds. At the distance of W3 (which we have taken to be 3 kpc) this corresponds to a projected linear size of 50 au or less for the size of the spots and a few hundred to several thousand au for their separations.

It is not known whether the length of the OH emitting region along the line of sight is about the same as the spot size or the separation, or has some other value. For some models of the OH emission it is a weak general rule to say that the time scale of any time variations is equal to the light travel time through the emitting region along the line of sight. This is true, for example, of a saturated maser that has its pump approximately at right angles to the line of sight. The output of such a maser is insensitive to changes in the microwave signal input, but a change in the pump power will change the output. The change in output of various regions along the line of sight will not reach the observer at the same time, however, and the result will be a rise or decay no faster than the time scale mentioned above.

Although the OH emission from the W3 region has been reported to be time varying [Coles, et al. (1968), Menon (1967b) and Sec. V-A of this report], this has been only partially confirmed. The OH emission from NGC 6334S, a source in the same class as W3, has varied dramatically in a time of 9 days or less (see Sec. V-E). Using the rule above, we get a length along the line of sight of about 1600 au. Other time varying OH emission sources seem to vary more slowly. There is no conflict with the assumption that the lengths of the OH emitting regions are much larger than their apparent projected diameters. In any case, some models for the OH emission sources have no restriction on the time scale of the observed time variations. For example, almost arbitrarily rapid variations may occur with a model that has the OH emission confined to a narrow angular beam which rotates onto and off of the line of sight to the observer.

This illustrates the value of searching for time variations on a time scale of hours. Such variations have been reported by Menon (1967); however, they have not been confirmed by other observers and in any case were attributed to interstellar scintillations rather than to changes in the sources. Robinson and Goss (1968) have reported variations with a time scale of milliseconds due to interplanetary scintillations.

It now seems likely that some or all of the OH emission sources are circumstellar clouds around a single star or at least objects whose characteristic scale size is appropriate for solar system dimensions rather than typical interstellar distances. Still open is the question of whether these are young objects in which the circumstellar cloud is in the process of contracting to form a star, or old objects in which the cloud has been ejected from the star. If it can be shown that the OH velocity field corresponds to contraction or rotation, we would conclude that the object is young; expansion would correspond to an old object. Furthermore, if the space velocities of the OH turn out to be larger than the escape velocity for some measured or assumed mass, then we would also conclude that the object is old. The mass of an object must be 28 solar masses for the escape velocity from a distance of 2000 au to be 5 km/sec. These numbers are appropriate for W3 [Moran, et al. (1968)]. Arguments presented below lead us to suspect that 5 km/sec is less than the true space velocity for the OH in objects such as W3 and so this mass is a lower limit if the OH is gravitationally bound corresponding to a young object. We have no way of knowing whether 28 solar masses is a reasonable number.

It is interesting in this connection to examine the spread in Doppler velocities among features from each source and compare the median or centroid of these velocities, which probably should be interpreted as the Doppler velocity of the cloud as a whole, with the Doppler velocities of the objects with which the OH emission is presumably associated (usually H II regions). In all cases the OH emission velocity spread includes the velocity of the associated object. Furthermore,

the offset of the velocity of the associated object from the median of OH emission velocities is often much less than the spread of the OH emission velocities. This suggests that the cloud of OH is moving rather rapidly (up to several tens of km/sec) with respect to the star it surrounds (expanding, contracting, or possibly rotating) but that the star and its envelope as a whole are moving rather slowly (typically less than 10 km/sec) with respect to nearby objects [see also Menon (1967a)]. These latter velocities are typically less than the random velocities of individual stars and this may be interpreted to mean that the OH emission sources are more massive than most stars and so their velocities on an equipartition basis are smaller. Menon (1967) has pointed out that the Doppler velocity of the OH emission from Orion is closer to the Doppler velocity of the cluster stars than to the Doppler velocity of the H II region, and he interprets this to mean that the OH emission source is a member of the same class of objects as the cluster stars.

With the discovery of more OH emission sources associated with visible objects such as VY Canis Majoris, it should be possible to explore these correlations in detail.

With the trepidation appropriate to a considerable extrapolation of our present knowledge, the physical picture in Fig. 56 is proposed to expl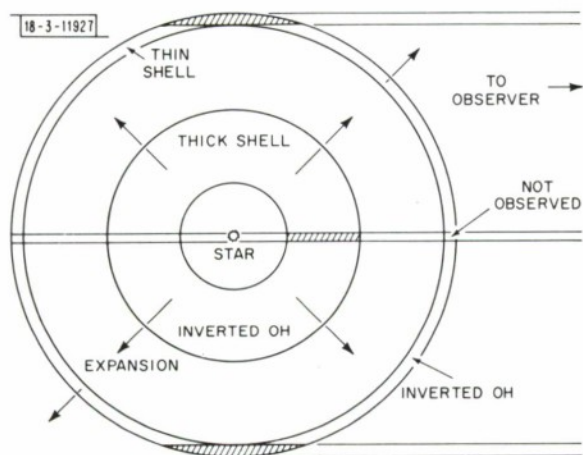ain some of the peculiarities of the OH emission sources. Figure 56 shows an expanding envelope of OH surrounding a star which provides the pump energy to invert the OH and also provides one source of microwave signal input to the resulting maser. The OH in the inner thick shell either is not saturated or is saturated by the microwave signal from the star. Thus only the cross-hatched region is visible to the observer. If the shell is expanding, the Doppler velocity of this visible OH will be negative with respect to the Doppler velocity of the star itself. This thick shell corresponds, for example, to the single feature at 1612 MHz seen in W28S.

Fig. 56. Schematic model of an OH emission source.

If it is more strongly inverted, the outer thin shell may be saturated by OH emission traveling approximately transverse to the direction to the star. This is because of the geometry which allows amplification of spontaneous emission along the longer transverse path until it dominates over microwave radiation from the star. Thus only the cross-hatched regions of the thin shell will be observed in OH emission and this emission is likely to be saturated and so polarized. The observed Doppler velocity spread will be small because the expansion (or contraction) velocity is largely transverse to the line of sight to the observer. Because of saturation and irregular motions, the appearance of the resulting OH emission will be patchy and irregular over the projected ring. The thin shell model corresponds to type I sources and in particular to the interferometer picture of the OH emission from W3 by Moran, et al. (1968).

Intermediate cases also occur, as, for example, a relatively thin shell which is not saturated and so can be seen both in amplified spontaneous emission and amplified stellar microwave continuum. The Doppler velocity spread in this case includes twice the expansion velocity (because even the far side of the shell can be seen) and this case corresponds, for example, to the very broad and relatively unpolarized emission from W28S at 1665 and 1667 MHz.

There are a number of obvious features of some of the OH emission sources which cannot be understood in terms of this simple picture. One of the more disturbing is the frequent occurrence of two groups of features at well separated Doppler velocities (for example, NML Cygnus and VY Canis Majoris at 1612 MHz) which may correspond to the front and rear of an expanding shell as suggested by Wilson and Barrett (1968b); what is not clear is why the rear of the shell should be prominent. It may be that the velocity field is such that the path length for amplification of a given frequency is longer in the radial direction either toward or away from the star, than in any transverse direction. This will be the case if there is little dispersion in velocity radial to the star, as might occur if the envelope were ejected gradually over an extended time rather than by a single explosion.

From this picture several predictions may be made to be tested by future observations. Among these predictions are: (1) The 1612 MHz feature in W28S should appear to come from the center of a larger region defined by the 1665 and 1667 MHz emission. (2) The features from type I sources (with narrow velocity spreads and highly polarized features) should define a rough ring when examined with high angular resolution. (3) For sources with a large Doppler velocity spread and relatively unpolarized features (for example, W28S at 1665 and 1667 MHz) the central features in velocity should define a region on the sky inside which should lie the higher velocity features (if the cloud is indeed expanding).

These predictions must be tested using the techniques of very long baseline interferometry.

VII. CONCLUSIONS AND SUGGESTIONS FOR FUTURE WORK

A. Conclusions

1. New Observational Constraints on OH Source Models

A considerable amount of specific new information about OH emission sources has been obtained in this study. Some of this information is probably related only to an individual source in the sense that each source is unique. However, a number of definite patterns are emerging and it is these patterns that must first be explained by OH source models. A completely satisfactory OH source model must now explain not only the high brightness temperature, the small angular sizes, and the strong linear and circular polarization of the OH emission sources, but also the variation of the percent circular and linear polarization and the linear polarization position angle with velocity across spectral features. In every feature that contains strong linear polarization, there is evidence for such a variation of the polarization position angle.

The dramatic and unambiguous time variations in the OH emission from NGC 6334S in a time of 9 days or less must also be explained by source models. Some source models (in general those with isotropic OH emission output) must be restricted in size by this time scale to 9 light days (1600 au) in thickness along the line of sight. Alternatively, the time variations might be explained by a model which emits OH photons only into a small solid angle which may then rotate on and off the line of sight to the observer. A lack of time variation in the polarization properties of the variable features seems to be indicated by the data and must be interpreted in terms of a lack of angular variation of the polarization properties of the OH emission for this model. This point, however, deserves further work.

By contrast, some of the features in some of the sources have remained remarkably constant in time. Most of the features in W3, for example, have not changed in any way after a time of more than three years.

Some source models imply the presence of detectable amounts of thermal microwave emission to be coincident with the OH emission position. This idea is supported by the continuum observations of W3 and some other sources. However, W75N and other sources have much less continuum emission or perhaps none at all. An OH source model which predicts a large amount of microwave continuum must be incorrect for these sources.

2. Associations Between OH Emission Sources and Nearby Objects

Observational selection effects may contribute to apparent associations between OH emission sources and nearby objects. Furthermore, phenomenological associations do not necessarily imply causal relationships. However, some associations seem to be well established and perhaps some causal relationships implied thereby.

Two OH emission sources (W28S and W49I) coincide with local maxima in the thermal continuum within the error limits of the positional measurements. These two OH sources may be inside dense H II regions. However, most Class I sources are displaced at least a few arcminutes from nearby strong thermal continuum maxima. There is probably some association between Class I OH emission sources and H II regions, but such an association cannot involve exact positional coincidence.

A similar statement may be made concerning OH emission sources and supernova remnants. In the Class II_a sources W28 and W44, the OH emission lies near the edge of an SNR. From the analysis of Sec. IV-B we conclude, however, that there is probably no causal association between SNR's and OH emission. Also many Class I OH emission sources have an SNR nearby but probably not close enough for any interaction.

We noted in several regions of the sky (W43, W44, and others) that we are probably observing two or more separate sources close together in angle but probably separated in distance. If this separation is correct, then interferometers or larger antennas should resolve these sources in angle as well. In some regions (W49, NGC 6334, and W75) we are clearly seeing two independent sources close together on the sky and also spatially proximate to each other.

These seemingly unrelated facts may be understood in terms of a breeding ground theory. Certain regions of the galaxy may contain the right combination of density, chemistry, and magnetic field to promote the formation of OH emission objects and also supernovae. Certain dusty H II regions are probably such breeding grounds.

In Sec. VI-C an OH source picture was presented which indicated that at least the Class II_b OH sources are probably old objects because the simplest explanation of their spectrum involves an expanding shell. An expanding circumstellar cloud probably corresponds to an old object although a young star just turned on might be seen in the process of blowing away its shell. It is interesting to note that the same class of OH sources (II_b) that seem most likely to be old are also not closely associated with H II regions or with the galactic plane. It is possible that these objects originally formed in the same breeding grounds as Class I sources, but have since escaped. There is little evidence that any of the OH sources trace spiral arms, but this needs more research.

This study has not solved the problem of the OH emission sources; this report can only describe the progress to date. The area of interest has widened to include some optically visible objects and the recently discovered water vapor emission. Rather than elucidating the situation, this study seems to have uncovered new anomalies and new complexities. Perhaps our present

situation with respect to the OH emission sources is similar to the early days in the study of stellar spectra. If so, we have a great deal of work yet to do. The following section describes some of the work which seems most likely to yield new insight into these problems.

B. Suggestions for Future Work

1. Extragalactic OH

Recently Roberts (1967) and Radhakrishnan (1967) reported negative results in their searches for OH emission from external galaxies. This section summarizes calculations on the detectability of extragalactic OH in emission and absorption.

Roberts (1967) based his calculations on so-called "normal" OH emission, that is, emission from extended regions of OH with excitation temperatures of the same order as the kinetic temperatures (Roberts actually calculates upper limits for the OH to H1 density ratios on the assumption of equal excitation temperatures). But such "normal" emission in our galaxy has only recently been detected (by Heiles, 1968) and is very weak. Let us assume that the external galaxy M31 is basically similar to our own galaxy, and calculate the detectability of OH absorption against the nucleus of M31 using the figures for the strong absorption in Sag A. We pick M31 because it is the nearest spiral galaxy.

We take the distance to M31 to be 6.3×10^5 pc and the distance to Sag A to be 10^4 pc. The OH absorption in Sag A is about 80°K in the Parkes 210-foot antenna [Bolton, et al. (1964a and b)], and is several hundred kHz wide. If we simply scale this to the distance of M31 and to the area of the NRAO 140-foot antenna we get

$$80° \times \left(\frac{10^4}{6.3 \times 10^5}\right)^2 \times (\frac{140}{210})^2 = 0.009°K$$

As an aside, note that we get the same number if we use the results of Goldstein, et al. (1964). They measured about 6.5°K of absorption with the Agassiz 60-foot telescope. We have avoided calculations based on the measured continuum temperature of M31 and assumed opacities, because it is difficult to estimate the fraction of the measured continuum temperature that arises in the nucleus.

To have a figure to compare with, we calculate the theoretical rms temperature fluctuation for a 200°K system temperature, a 100-kHz bandwidth, and an 8-hour integration time as

$$\Delta T = \frac{2 T_{sys}}{\sqrt{\beta t}} = \frac{2 \times 200}{\sqrt{10^5 \times 8 \times 3600}} = 0.008°K \quad .$$

The upper limit placed by Roberts (1967) on the emission (and presumably also the absorption) in the direction of the nucleus of M31 was 0.04°K, based on a 45 minute integration with approximately the above system parameters.

Several comments need to be made. It is clearly possible to increase the bandwidth, perhaps to 500 kHz, and also increase the integration time, so the signal is detectable if the above figures are accurate. Also both transitions can be measured simultaneously and this increases the detectability. However, the integration time requirements depend on the fourth power of the distance to M31 and this distance is not too accurately known. And finally, we are looking at M31 in a direction well out of the plane of that galaxy. If the absorbing OH is confined to the plane of the galaxy, as seems likely, then the absorption in our direction may be much less than

that between the sun and Sag A. It is possible to find other spiral galaxies that are seen edge-on, but they are considerably farther away and the distance dependence mentioned above puts them out of the question.

Now let us assume the existence of a W49-type object in M31. W49 produces about a 100°K peak in the NRAO 140-foot telescope [Palmer and Zuckerman (1967)]. If we take the distance to W49 to be 15 kpc and scale the temperature to the distance of M31 we get 0.057°K. However, this peak temperature will only be gotten if we use a 1- or 2-kHz resolution and this increases the rms temperature fluctuations by a factor of 7 to 10 for the same integration time. Furthermore, we know neither the position nor the velocity of this hypothetical W49-type object in M31, so a search is necessary. And finally we should note that W49 is very probably unique in our galaxy; its spectral luminosity is considerably higher than any other known OH emission source; there may be no comparable object in M31. It seems, then, that a search for W49-type OH emission objects in M31 is less likely to succeed than a search for OH absorption against the galactic nucleus of M31. Ball and Zuckerman have proposed to use the NRAO 140-foot telescope to look for extragalactic OH.

2. $O^{18}H$ in Emission

In the terrestrial environment the isotopes O^{16} and O^{18} are in the ratio of about 490 to 1. Barrett and Rogers (1964), Rogers (1967a), and Rogers and Barrett (1966) calculated the frequencies of the four 18-cm transitions in $O^{18}H$ and obtained the values shown in Table XVIII. They then observed the 1639-MHz absorption of $O^{18}H$ against the galactic center and confirmed the line rest frequency and the relative abundances. Similar results have been reported from Australia [Robinson (1967)], and by Wilson and Barrett (1968).

The strength of radio emission from $O^{18}H$ is more difficult to calculate because the $O^{16}H$ emission sources are very far from thermodynamic equilibrium. We obtain the 1/490 ratio for the $O^{18}H$ to $O^{16}H$ radio emission only if the OH radio emission comes from a maser for which (a) the terrestrial oxygen abundance ratio (1/490) holds for the observed OH, (b) the pumping mechanisms are independent of isotopic species, and (c) the maser at both the $O^{16}H$ and the

TABLE XVIII		
$O^{18}H$ AND $O^{16}H$ FREQUENCIES		
$F \to F$	$O^{16}H$ Frequency* (kHz)	$O^{18}H$ Frequency† (kHz)
$1 \to 2$	1612231	1584330
$1 \to 1$	1665401	1637460
$2 \to 2$	1667358	1639460
$2 \to 1$	1720533	1692630
* As measured by Radford (1964).		
† As calculated by Barrett and Rogers (1964) with expected errors of about 100 kHz.		

$O^{18}H$ transitions is fully saturated. Assumption (a) is likely to hold, at least approximately; however (b) and (c) are less likely. Some of the proposed maser pumping models are sensitive to the isotopic species or at least the isotopic density. For example, models involving selective absorption or resonance trapping of pump photons [Litvak, et al. (1966), Litvak, et al. (1969)] will be less efficient for the less abundant species unless the absorption lines at the pump frequencies overlap due to Doppler broadening. Pumping models which involve the formation of OH in excited states are probably independent of isotopic species. It is difficult to evaluate the likelihood of assumption (c); however the strong polarization of the 1665- and 1667-MHz emitters (e.g., W3 and W49) is probably related to a maser saturation effect. The 1612-MHz emission from NML Cygnus [Wilson and Barrett (1968b)] and VY Canis Majoris [Eliasson and Bartlett (1969)] is less strongly polarized.

Wilson and Barrett (1968a) reported negative results in their search for $O^{18}H$ emission at 1637 MHz from W3 and W49, and gave an upper limit significantly better than the 1/490 terrestrial oxygen abundance ratio times the 1665-MHz emission. Because the 1612-MHz emitters probably belong to a different class of objects, $O^{18}H$ emission at 1584 MHz from NML Cygnus and VY Canis Majoris at velocities corresponding to their 1612-MHz emission should be sought. Such a project is under way (Ball and Penfield, to be published).

3. High Resolution Stokes Parameters

Although most OH emission features seem to be resolved with 1-kHz instrumental resolution, it was pointed out in Sec. VI-C-1 that many features show a variation of polarization properties as a function of velocity across the feature. This suggests that some of the emission which appears to be only partially polarized may contain a higher degree of polarization and additional complexities when examined with higher spectral resolution. For example, it may be possible to understand the unpolarized features in W51 either in terms of overlapping polarized features, or as cases in which the variation of the linear polarization position angle is so rapid that it is smeared by the 1-kHz instrumental resolution.

4. Further Studies of Time Variations

It was pointed out in Sec. VI-C that studies of the time variations may help us understand both the kinematics and the physics of the OH emission sources. It is particularly important to determine whether the variable features change their flux without changing their degree and sense of polarization as suggested by Ball and Mecks (1968) and Zuckerman, et al. (1969) or whether the polarization percentages also change as suggested by Coles, et al. (1968) and Goss and Robinson (1969).

Another important area of study is now possible for those OH emission sources associated with visible objects. Any time variations in the OH emission should be compared with variations at optical and infrared wavelengths. Such a comparison along with long-baseline interferometer data may eventually allow us to specify more precisely the physical conditions near the OH emission source in a complex object such as VY Canis Majoris which apparently consists of several stars and extended nebulosity [Wallerstein (1958 and 1969)].

Ball and Zuckerman have proposed to use the NRAO 140-foot telescope and the 413-channel digital correlator to measure the Stokes parameters of well known sources with high resolution in order to look for the effects mentioned in Sec. VII-B-3 and to make comparisons with previous work as a check on the character of the time variations.

5.   Search for New OH Emission Sources

Evidence was presented in this report for the existence of some association between OH emission sources and (1) supernova remnants (or galactic nonthermal sources), (2) H II regions (or galactic thermal sources), (3) IR stars, and (4) the galactic plane. One should therefore look for new OH emission sources near objects of this kind which have not already been observed. Several such programs are already in progress or proposed: (1) near SNR's or galactic NTS's by Ball (to be published) and by Downes (private communication), (2) near H II regions or galactic thermal sources by Downes (private communication), (3) near IR stars by Eliasson and Groth (1968) and by Wilson and Barrett (private communication), and near selected optical stars by Ball (to be published), and (4) selected sections of the galactic plane by Elldér, et al. (1969).

It was pointed out in Sec. VI-A that some of the apparent phenomenological associations between OH emission sources and other objects may be the result of observational selection effects. To check this, a search for OH emission sources in randomly selected regions of the sky should be conducted. Only if such a search turns up enough OH emission sources to give statistically significant correlations with other objects can we be certain that such correlations are meaningful.

6.   Interferometry and Correlations with H_2O Emission

Very likely the next major step in understanding the OH emission sources will come from VLB interferometry (see Sec. VI-C) and from a study of the H_2O emission sources [Cheung, et al. (1969), Knowles, et al. (1969)] which are probably the same objects as those seen in OH emission. VLB interferometry on OH emission sources is being pursued by Moran (private communications), and Lilley, Penfield, and Ball have proposed to use the Haystack-Westford interferometer to study the spatial distribution of H_2O emission sources.

ACKNOWLEDGMENTS

REFERENCES

Abramowitz, M. and Stegun, I.A., Handbook of Mathematical Functions (Natl. Bur. Standards, 1964).

Aikman, G.C., M.Sc. thesis, Department of Astronomy, University of Toronto (1968).

Aizu, K., and Tabara, H., Progress in Theor. Phys. (Japan) 37, 296 (1967).

Akabane, K., Morimoto, M., Miyazawa, K., Suguri, Y., Ishizawa, Y., Nakajima, T. and Kawajiri, N., Pub. Astr. Soc. Japan 19, 88 (1967).

Allen, R.J., Ph.D. thesis, Department of Physics, M.I.T. (1967).

Allen, R.J. and Barrett, A.H., Astrophys. J. 149, 1 (1967).

Allen, R.J., Barrett, A.H. and Crowther, P.P., Astrophys. J. 151, 43 (1968).

Ball, J.A., Technical Note 1968-22, Lincoln Laboratory, M.I.T. (1968).

Ball, J.A. and Meeks, M.L., Astrophys. J. 153, 577 (1968).

Ball, J.A. and Staelin, D.H., Astrophys. J. 153, L41 (1968).

Barrett, A.H. and Lilley, A.E., Astronom. J. 62, 5 (1957).

Barrett, A.H. and Rogers, A.E.E., Quarterly Progress Report 74, 16 Research Laboratory of Electronics, M.I.T. (1964).

——————————————————, Nature 210, 188 (1966).

Barrett, A.H., Meeks, M.L. and Weinreb, S., Nature 202, 475 (1964).

Bolton, J.G., Gardner, F.F., McGee, R.X. and Robinson, B.J., Nature 204, 30 (1964).

Bolton, J.G., van Damme, K.J., Gardner, F.F. and Robinson, B.J., Nature 201, 279 (1964b).

Born, M., Wolf, E., Principles of Optics (Pergamon/Macmillan, New York, 1964).

Bracewell, R.N., Proc. IRE 46, 106 (1958).

——————————, The Fourier Transform and its Applications (McGraw-Hill, New York, 1965).

Bracewell, R.N. and Roberts, J.A., Aust. J. Phys. 7, 615 (1954).

Caswell, J.L., Royal Astronom. Soc. Monthly Notices 136, 11 (1967).

Cheung, A.C., Rank, D.M., Townes, C.H., Thornton, D.D. and Welch, W.J., Nature 221, 626 (1969).

Clark, B.G., Astrophys. J. 142, 1398 (1965).

Clark, B.G., Radhakrishnan and Wilson, R.W., Astrophys. J. 135, 151 (1962).

Coles, W.A., Rumsey, V.H. and Welch, W.J., Astrophys. J. (Letters) 154, L61 (1968).

Conant, G.H., Jr. and Meeks, M.L., Technical Note 1968-1, Lincoln Laboratory, M.I.T. (1968).

Courtes, G., Ann. d'Ap. 23, 115 (1960).

Cudaback, D.D., Read, R.B. and Rougoor, G.W., Phys. Rev. Letters 17, 452 (1966).

Cudaback, D.D. and Heiles, C., Astrophys. J. 155, L21 (1969).

Davies, R.D., Jager, G. de and Verschuur, G.L., Nature 209, 974 (1966).

Davies, R.D., Rowson, B., Booth, R.S., Cooper, A.J., Gent, H., Adgie, R.L. and Crowther, J.H., Nature 213, 1109 (1967).

Dieter, N.H., Astrophys. J. 150, 435 (1967).

Dieter, N.H. and Ewen, H.I., Nature 201, 279 (1964).

Dieter, N.H., Weaver, H. and Williams, D.R.W., Astronom. J. 71, 160 (1966a).

——————————————————————, Sky and Telescope 31, 132 (1966b).

Dousmanis, G.C., Sanders, T.M., Jr. and Townes, C.H., Phys. Rev. $\underline{100}$, 1735 (1955).

Downes, D. and Rinehart, R., Astrophys. J. $\underline{144}$, 937 (1966).

Ehrenstein, G., Townes, C.H. and Stevenson, M.J., Phys. Rev. Letters $\underline{3}$, 40 (1959).

Eliasson, B. and Bartlett, J.F., Astrophys. J. $\underline{155}$, L79 (1969).

Eliasson, B. and Groth, E.J., Astrophys. J. $\underline{154}$, L17 (1968).

Elldér, J., Rönnäng, B. and Winnberg, A., Nature $\underline{222}$, 67 (1969).

Gardner, F.F., McGee, R.X. and Robinson, B.J., Aust. J. Phys. $\underline{20}$, 309 (1967).

Gardner, F.F., Robinson, B.J., Bolton, J.G. and van Damme, K.J., Phys. Rev. Letters $\underline{13}$, 3 (1964).

Goldstein, S.J., Jr., Gundermann, E.J., Penzias, A.A. and Lilley, A.E., Nature $\underline{203}$, 65 (1964).

Goss, W.M., Astrophys. J. Supp. $\underline{15}$, 131-202 (1968).

Goss, W.M. and Field, G.B., Astrophys. J. $\underline{151}$, 177 (1968).

Goss, W.M. and Robinson, B.J., Astrophys. Letters $\underline{2}$, 81 (1968).

Goss, W.M., Robinson, B.J. and Manchester, R.N., Proc. Astron. Soc. of Australia $\underline{1}$, 214 (1969).

Goss, W.M. and Spinrad, H., Astrophys. J. $\underline{143}$, 989 (1966).

Gudnov, V.M. and Sorochenko, R.L., "Emission of Excited Hydrogen Line $n_{105} - n_{104}$ in Certain Nebulae in the Northern Sky," P.N. Lebedev Physical Institute, Academy of Sciences of the U.S.S.R., Radio Astronomy Laboratory, Moscow (1966).

Gundermann, E., Ph.D. thesis, Department of Astronomy, Harvard University (1965).

Haddock, F.T., Mayer, C.H. and Sloanaker, R.M., Nature $\underline{174}$, 176 (1954).

Heart, F.E., Mathiasen, A.A. and Smith, P.D., Technical Report 406, Lincoln Laboratory, M.I.T. (27 October 1965), DDC AD-631559.

Heiles, Carl E., Astrophys. J. $\underline{151}$, 919 (1968).

Herzberg, G., Spectra of Diatomic Molecules (D. van Nostrand, Princeton, 1950).

Hollinger, J.P. and Hobbs, R.W., Science $\underline{153}$, 1633 (1966).

Howard, W.E., III and Maran, S.P., Astrophys. J. Supp. $\underline{10}$, 1 (1965).

Ishida, K. and Akabane, K., Nature $\underline{217}$, 433 (1968).

Jackson, J.D., Classical Electrodynamics (John Wiley & Sons, Inc., New York, 1962).

Johnston, I.D., Astrophys. J. $\underline{150}$, 33 (1967).

Kesteven, M.J.L., Aust. J. Phys. $\underline{21}$, 369 (1968a).

——————————, Aust. J. Phys. $\underline{21}$, 739 (1968b).

Knowles, S.H., Mayer, C.H., Cheung, A.C., Rank, D.M. and Townes, C.H., Science $\underline{163}$, 1056 (1969).

Kraus, J.D., Radio Astronomy (McGraw-Hill, New York, 1966).

Kundu, M.R. and Velusamy, T., Ann. D'Astrophys. $\underline{30}$, 59 (1967).

Lilley, A.E., Menzel, D.H., Penfield, H., and Zuckerman, B., Nature $\underline{209}$, 468 (1966).

Litvak, M.M., Zuckerman, B. and Dickinson, D.F., Astrophys. J. $\underline{156}$, 875 (1969).

Litvak, M.M., McWhorter, A.L., Meeks, M.L. and Zeiger, H.J., Phys. Rev. Letters $\underline{17}$, 821 (1966).

MacLeod, J.M. and Doherty, L.H., Astrophys. J. $\underline{154}$, 833 (1968).

McGee, R.X. and Gardner, F.F., Proc. Astronom. Soc. of Australia $\underline{1}$, 19 (1967).

McGee, R.X. and Gardner, F.F., Aust. J. Phys. 21, 149 (1968).

McGee, R.X., Gardner, F.F. and Robinson, B.J., Aust. J. Phys. 20, 407 (1967).

McGee, R.X., Milton, J.A. and Wolfe, W., Aust. J. Phys., Astrophys. Supp. 1, (1966).

McGee, R.X., Robinson, B.J., Gardner, F.F. and Bolton, J.G., Nature 208, 1193 (1965).

Manchester, R.N., Goss, W.M. and Robinson, B.J., Astrophys. Letters 3, 11 (1969).

Meeks, M.L., Ball, J.A., Carter, J.C. and Ingalls, R.P., Science 153, 978 (1966).

Meeks, M.L., Ball, J.A. and Hull, A.B., Trans. IEEE Ant. Prop. AP-16, 746 (1968).

Menon, T.K., Astrophys. J. 150, L167 (1967a).

_____, Internatl. Astronom. Union Symposium 31, (1967b), p. 121.

Mezger, P.G., Altenhoff, W., Schraml, J., Burke, B.F., Reifenstein, E.C., III and Wilson, T.L., Astrophys. J. 150, L157 (1967).

Mezger, P.G. and Henderson, A.P., Astrophys. J. 147, 471 (1967).

Mezger, P.G. and Höglund, B., Astrophys. J. 147, 490 (1967).

Mezger, P.G., Schraml, J. and Terzian, Yervant, Astrophys. J. 150, 807 (1967).

Miller, J.S., Astrophys. J. 151, 473 (1968).

Minkowski, R., "Nonthermal Galactic Radio Sources" in Nebulae and Interstellar Matter, eds. B.M. Middlehurst and L.H. Aller (Univ. of Chicago Press, Chicago, 1968) p. 623.

Moran, J.M., Barrett, A.H., Rogers, A.E.E., Burke, B.F., Zuckerman, B., Penfield, H. and Meeks, M.L., Astrophys. J. 148, L69 (1967a).

Moran, J.M., Burke, B.F., Barrett, A.H., Rogers, A.E.E., Ball, J.A., Carter, J.C. and Cudaback, D.D., Astrophys. J. 152, L97 (1968).

Moran, J.M., Crowther, P.P., Burke, B.F., Barrett, A.H., Rogers, A.E.E., Ball, J.A., Carter, J.C. and Bare, C.C., Science 157, 676 (1967b).

Neugebauer, G., Hilgeman, T. and Becklin, E., 128th Amer. Astronom. Soc. Meeting, Austin, Texas (1968).

Oster, L., Rev. Mod. Phys. 33, 525 (1961).

Palmer, P. and Zuckerman, B., Astrophys. J. 148, 727 (1967).

Penzias, A.A., Astronom. J. 69, 46 (1964).

Pike, E.M. and Drake, F.D., Astrophys. J. 139, 545 (1964).

Poveda, A. and Woltjer, L., Astronom. J. 73, 65 (1968).

Purcell, E.M., Astrophys. J. 116, 457 (1952).

Radford, H.E., Phys. Rev. 122, 114 (1961).

_____, Phys. Rev. Letters 13, 534 (1964).

Radhakrishnan, V., Aust. J. Phys. 20, 203 (1967).

Radhakrishnan, V. and Whiteoak, J.B., Proc. Astronom. Soc. of Australia 1, 20 (1967).

Raimond, E. and Eliasson, B., Astrophys. J. 150, L171 (1967).

_____, Astrophys. J. 155, 817 (1969).

Reifenstein, E.C., III, Ph.D. thesis, Department of Physics, M.I.T. (1968).

Rieu, Nguyen Quang, Notes et Information de Observatoire de Paris, 11-2, 15 (1963).

Roberts, Morton S., Astrophys. J. 148, 931 (1967).

Robinson, B.J., Internatl. Astronom. Union Symposium 31, 49 (1967).

Robinson, B.J. and Goss, W.M., Astrophys. Letters 2, 5 (1968).

Robinson, B. J. and McGee, R. X., Ann. Rev. Astron. and Astrophys. 5, 183 (1967).

Robinson, B. J., Gardner, F. F., van Damme, K. J. and Bolton, J. G., Nature 202, 989 (1964).

Rogers, A. E. E., Masters thesis, Department of Electrical Engineering, M. I. T. (1964).

_____, Ph. D. thesis, Department of Electrical Engineering, M. l. T. (1967a).

_____, Technical Report 457, Research Laboratory of Electronics, M. I. T. (15 March 1967b).

_____, Technical Report 441, Lincoln Laboratory, M. l. T. (1968), DDC AD-666038.

Rogers, A. E. E. and Barrett, A. H., Astronom. J. 71, 868 (1966).

_____, Internatl. Astronom. Union Symposium 31, 77 (1967).

_____, Astrophys. J. 151, 163 (1968).

Rogers, A. E. E., Moran, J. M., Crowther, P. P., Burke, B. F., Meeks, M. L., Ball, J. A. and Hyde, G. M., Phys. Rev. Letters 17, 450 (1966).

Rogers, A. E. E., Moran, J. M., Crowther, P. P., Burke, B. F., Meeks, M. L., Ball, J. A. and Hyde, G. M., Astrophys. J. 147, 369 (1967).

Ryle, M. and Downes, D., Astrophys. J. 148, L17 (1967).

Ryle, M., Elsmore, B. and Neville, A. C., Nature 205, 1259 (1965).

Scheuer, P. A. G., Observatory 83, 56 (1963).

Shaver, P. A., Royal Astronom. Soc. Monthly Notices 142, 273 (1969).

Shklovsky, I. S., Dok. Akad. Nauk. USSR 92, 25 (1953).

Stuart, D. G., Technical Note 1968-7, Lincoln Laboratory, M. I. T. (1968), DDC AD-667518.

Stylos, P., Technical Note 1965-14, Lincoln Laboratory, M. I. T. (1965), DDC AD-620872.

Townes, C. H., lnternatl. Astronom. Union Symposium 4, 92 (1957).

Townes, C. H. and Schawlow, A. L., Microwave Spectroscopy (McGraw-Hill, New York, 1955).

Turner, B. E., Ph. D. thesis, Department of Astronomy, University of California (1967).

_____, Astrophys. J. 57, 103 (1969).

Wallerstein, G., Pub. Astronom. Soc. of the Pacific 70, 479 (1958).

_____, 129th Amer. Astronom. Soc. Meeting, Honolulu (1969).

Weaver, H. F., Dieter, N. H. and Williams, D. R. W., Astrophys. J. Supp. 16, 219 (1968).

Weaver, H. F. and Williams, D. R. W., Nature 201, 380 (1964).

Weaver, H. F., Williams, D. R. W., Dieter, N. H. and Lum, W. T., Nature 208, 29 (1965).

Weaver, H. F., Williams, D. R. W. and Dieter, N. H., Astronom. J. 71, 184 (1966).

Weinreb, S., Technical Report 412, Research Laboratory of Electronics, M. l. T. (1963).

Weinreb, S., Barrett, A. H., Meeks, M. L. and Henry, J. C., Nature 200, 820 (1963).

Weinreb, S., Meeks, M. L., Carter, J. C., Barrett, A. H. and Rogers, A. E. E., Nature 208, 440 (1965).

Weiss, H. G., lEEE Spectrum 14, 51 (1965).

Williams, D. R. W., Dieter, N. H. and Weaver, H. F., Astronom. J. 71, 186 (1966).

Wilson, R. E., Catalogue of Radial Velocities, Carnegie Inst. of Washington Pub. 601 (1953).

Wilson, R. W., "Observations of Owens Valley Radio Observatory" Cal. Inst. Tech. Pub. No. 2 (1963).

Wilson, R. W. and Bolton, J. G., Pub. Astronom. Soc. of the Pacific 72, 331 (1960).

Wilson, W. J. and Barrett, A. H., Quarterly Progress Report 90, Research Laboratory of Electronics, M. I. T. (1968a), p. 9.

—————————————————, Science 161, 778 (1968b).

—————————————————, to be published (1969).

Yen, J. L., Zuckerman, B., Palmer, P. and Penfield, H., Astrophys. J. 156, L27 (1969).

Zuckerman, B., Ball, J. A., Dickinson, D. F. and Penfield, H., Astrophys. Letters (1969).

Zuckerman, B., Lilley, A. E. and Penfield, H., Nature 208, 441 (1965).

Zuckerman, B., Palmer, P., Penfield, H. and Lilley, A. E., Astrophys. J. 153, L69 (1968).

DOCUMENT CONTROL DATA – R&D

(Security classification of title, body of abstract and indexing annotation must be entered when the overall report is classified)

1. ORIGINATING ACTIVITY *(Corporate author)*	2a. REPORT SECURITY CLASSIFICATION
Lincoln Laboratory, M.1.T.	Unclassified
	2b. GROUP None

3. REPORT TITLE

Observations of OH Radio Emission Sources

4. DESCRIPTIVE NOTES *(Type of report and inclusive dates)*

Technical Report

5. AUTHOR(S) *(Last name, first name, initial)*

Ball, John A.

6. REPORT DATE	7a. TOTAL NO. OF PAGES	7b. NO. OF REFS
23 May 1969	104	150

6a. CONTRACT OR GRANT NO. AF 19(628)-5167	9a. ORIGINATOR'S REPORT NUMBER(S)
b. PROJECT NO. 649L	Technical Report 458
c.	9b. OTHER REPORT NO(S) *(Any other numbers that may be assigned this report)*
d.	ESD-TR-69-138

10. AVAILABILITY/LIMITATION NOTICES

This document has been approved for public release and sale; its distribution is unlimited.

11. SUPPLEMENTARY NOTES	12. SPONSORING MILITARY ACTIVITY
None	Air Force Systems Command, USAF

13. ABSTRACT

The 18-cm OH radio emission sources were studied to determine their character and their relation to other objects in our galaxy. The Haystack and Millstone antennas were used with a 100-channel digital autocorrelator to obtain Stokes parameter spectra of many of the brighter sources. Time variations in the OH emission from some of these sources were detected and studied and maps of the regions around OH emission sources were obtained in the continuum near 2 and 4 cm. The Haystack-Millstone spectral-line interferometer was used to check the positions of a pair of OH emission sources and to search for angular variation in the OH absorption across Cas A. Evidence for phenomenological associations between OH emission and H ll regions, supernovae remnants, and infrared objects is discussed in the report and a kinematic model of the OH emission sources presented.

14. KEY WORDS

OH radio emission sources	radio astronomy	radio continuum sources
Haystack antenna	interferometry	microwave spectral lines
Millstone antenna		